GENERATING AUTOMATED FORESTRY GEOINFORMATION PRODUCTS FROM REMOTELY SENSED IMAGERY

by WOLFGANG LÜCK

Thesis presented in partial fulfilment of the requirements for the degree of Master of Science in the Faculty of Science at Stellenbosch University, South Africa

UNIVERSITEIT
iYUNIVESITHI
STELLENBOSCH
UNIVERSITY

Supervisor: Prof A van Niekerk

December 2018

DECLARATION

By submitting this report electronically, I declare that the entirety of the work contained therein is my own, original work, that I am the sole author thereof (save to the extent explicitly otherwise stated) that reproduction and publication thereof by Stellenbosch University will not infringe any third-party rights and that I have not previously, in its entirety or in part, submitted it for obtaining any qualification.

Date: December 2018

Whatever you do or dream you can, begin it:
Boldness has genius, power and magic in it.
Begin it now.

Johann Wolfgang von Goethe

SUMMARY

Private industry, national government departments, and the international community rely on geoinformation to optimise activities, enforce legislation, and assess global markets concerned with the use of natural resources. One of the main challenges faced by the remote sensing community is to derive thematic information from available imagery at the required speed, consistency, quality, and cost. The international space science community has organised itself within the Committee on Earth Observation Satellites to combine information systems for providing global information services as part of the resulting Global Earth Observation System of Systems (GEOSS). The European Union also initiated a programme called Copernicus, formally known as Global Monitoring for Environment and Security (GMES), which aims to provide information services as a contribution to GEOSS. Copernicus/GMES provides three core services consisting of land, marine, and emergency response, and two pilot services relating to the atmosphere and security aspects; each core service consists of several service elements. The forest monitoring programme is part of the land core services.

At present only Landsat archives provide a consistent and affordable data source to serve the land core services on local and regional levels. This is particularly true for all services addressing the thematic field of forestry, as the relatively low vegetation dynamics of forestry (compared to other cultivated crops) can be served by Landsat data as it optimally provides one cloud-free (cloudless) observation (not necessarily cloud-free scene) per season. Landsat data is also freely available from the United States Geological Survey (USGS) and several other ground receiving stations around the world. This makes it financially viable to use Landsat data for providing operational services that would otherwise be too expensive to deliver using commercially purchased satellite imagery. Another advantage of Landsat data is that it is well calibrated, and includes multispectral bands covering the full passive remote sensing spectrum from blue light to thermal radiation. While the blue band is useful for the characterisation of atmospheric effects, the red, near-infrared, and shortwave infrared bands are suitable for the characterisation of different vegetation types, in particular forests. The spatial resolution of Landsat imagery (15–30 m) is also suitable for forestry applications, in particular when the monitoring of tree clusters instead of individual trees is required. Given these unique attributes of Landsat imagery, this study focused on the development of a processing chain for the automatic extraction of forestry geoinformation products from Landsat thematic mapper (TM)/enhanced thematic mapper (ETM)+ imagery. The products generated consist of a plantation and indigenous forest mask, and a broad genus classification for plantation forests. The products were generated and validated in

three regions in South Africa, namely Cape Town (Western Cape Province); the Natal Midlands (KwaZulu-Natal Province); and the eastern escarpment and Lowveld region (Limpopo and Mpumalanga provinces). The results show that the products have an overall accuracy exceeding 93% for all areas, which will make them useful for forestry operations and planning. Although the resulting forestry products are evaluated in a South African context, the methodology can also be applied in other regions. The methods can also be adapted for application on other data sources such as those offered by the recently-launched Copernicus Sentinel 2 satellite and other commercially-operated satellites such as RapidEye, Resourcesat, and Spot.

KEY WORDS

remote sensing, Landsat TM ETM+, automated satellite image processing, radiometric normalisation, image compositing, automated spectral classification, machine learning, plantation forest genus classification

OPSOMMING

Die privaatsektor, nasionale regeringsdepartemente en die internasionale gemeenskap maak staat op geoinligting om aktiwiteite te optimaliseer, die nakoming van wetgewing af te dwing, en toegang te verkry tot globale markte wat verband hou met die gebruik van natuurlike hulpbronne. Een van die grootste uitdagings van die afstandwaarnemings-gemeenskap is om tematiese inligting van beskikbare beelde teen die vereiste spoed, konsekwentheid, kwaliteit en koste te bekom. Die internasionale ruimtewetenskapgemeenskap het hulself binne die Komitee vir Aardobservasie-satteliete (KAOS) georganiseer ten einde inligtingstelsels te kombineer om globale inligtingsdienste as deel van die gevolglike Globale Aardobservasiestelsel van Stelsels (GAOSS) te verskaf. Die Europese Unie het ook met ’n program, Copernicus (voorheen bekend as Globale Monitering vir Omgewing en Sekuriteit (GMOS)), begin wat daarop gemik is om inligting as ’n bydrae tot GEOSS te verskaf. Copernicus/GMOS bied drie kerndienste, naamlik land-, mariene- en noodreaksies, asook twee loodsdienste wat betrekking het op atmosferiese- en sekuriteitsaspekte. Elke kerndiens bestaan uit verskeie dienselemente en die bosbou-moniteringsprogram is ’n deel van die landkerndienste.

Tans voorsien slegs Landsat-argiewe ’n konsekwente en bekostigbare databron om die landkerndienste op plaaslike- en streeksvlakke te dien. Dit is veral waar vir alle dienste wat die tematiese gebied van bosbou aanspreek omdat die relatief lae plantegroei-dinamika van bosbou (in vergelyking met ander verboude gewasse) goed deur Landsat-data beskryf word. Onder optimale omstandighede word meer as een wolkvrye (wolklose) waarneming (nie noodwendig ’n wolkvrye beeld nie) per seisoen oor bosbougebiede gemaak. Landsat-data is ook vrylik beskikbaar van die Verenigde State se Geologiese Opname (VSGO) en van verskeie ander grond-ontvangstasies regoor die wêreld. Dit maak dit finansieel lewensvatbaar om Landsat-data te gebruik vir die verskaffing van operasionele dienste wat te duur sou wees om te voorsien indien satellietdata kommersieël aangekoop is. Nog ’n voordeel van Landsat-data is dat dit goed gekalibreer is en multispektrale bande insluit wat die volle passiewe afstandswaarnemingspektrum, van blou lig tot termiese straling, dek. Die blou band is nuttig vir die karakterisering van atmosferiese effekte, terwyl die rooi, nabye-infrarooi en kortgolf-infrarooi bande geskik vir die karakterisering van verskillende tipes plantegroei, veral woude. Die ruimtelike resolusie van Landsat-beelde (15–30 m) is ook geskik vir bosboutoepassings, veral waar die monitering van groeperinge in bome in plaas van individuele bome vereis word. Gegewe hierdie unieke eienskappe van Landsat-beelde het hierdie studie op die ontwikkeling van ’n verwerkingsketting vir die outomatiese onttrekking van bosbou-geoinligtingsprodukte

van Landsat TM/ETM+ beelde gefokus. Die geskepte produkte bestaan uit ’n plantasie en inheemse woudmasker en 'n breë genusklassifikasie vir bosbouplantasies. Die produkte is gegenereer en geëvalueer in drie streke in Suid-Afrika, naamlik Kaapstad (Wes-Kaap Provinsie); die Natal Midland (KwaZulu-Natal Provinsie); en die Oos-platorand en Laeveld streek (Limpopo en Mpumalanga provinsies). Die resultate toon dat die produkte hoogs akkuraat is met algemene akkuraatheid van oor die 93% vir al die areas, wat hulle baie nuttig sal maak vir bosboubedrywighede en -beplanning. Alhoewel die gevolglike bosbouprodukte in ’n Suid-Afrikaanse konteks geëvalueer word, kan hulle ook in ander wêreldstreke toegepas word. Die metodes kan ook aangepas word vir toepassing op ander databronne soos die onlangs-gelanseerde Copernicus Sentinel-2-satelliet, asook ander kommersieel-bedrewe satelliete soos RapidEye, Resourcesat en Spot.

SLEUTELWOORDE

afstandswaarneming, Landsat TM ETM+, automatiese satellietbeeldverwerking, radiometriese normalisasie, beeldkombinering, outomatiese spektrale klassifikasie, masjienleer, genus-klassifikasie in woudplantasies

ACKNOWLEDGEMENTS

The author is greatly indebted to a wide range of individuals and institutions. The following is a short recognition of the many contributions that made this work possible:

- SARVANNA project coordinated by Prof. Christiane Schmullius from the University of Jena and Prof. Harold Annegarn from the University of Johannesburg for making the airborne field survey in the Lowveld study area possible.
- The Chief Directorate of National Geospatial Information for funding the field work for all areas under the Land Cover Field Guide project.
- Komatiland Forests, in particular Benita Smith, for the provision of stand level reference data for plantations in the Lowveld and Escarpment.
- The United States Geological Survey (USGS) for the provision of all the relevant satellite imagery used in this study.
- Kevin Melhuish, the local agent for PCI Geomatica software, for the provision of many extensions of temporary licences which allowed the processing of data.
- David Roy and Andrea Baraldi for lively discussions and the exchange of ideas.
- The University of Stellenbosch and in particular Prof. Adriaan van Niekerk for his support and trust in me; granting numerous extensions to complete the thesis and acknowledging my busy commercial activities to sustain my family.
- Brian van Wilgen for providing me with a hideout to concentrate on the compilation of this document.
- My dearest wife Stephanie Lück for proofreading and editing graphics as well as the continual moral support. Your love has carried me through this ordeal.
- My parents for the many years of support, both morally and financially. I would also like to thank my father for accompanying and supporting me with fieldwork in the Natal Midlands. Special thanks to my mother who supported me throughout and provided me with accommodation and great meals, as well as making many other sacrifices.
- Finally, I would like to thank many fellow remote sensing specialists at research institutions and students for the exchange of ideas and stimulating discussions.

DEDICATION

This thesis is dedicated to the sustainable use of natural resources, in particular forests, and in this context to the “Arbeitsgemeinschaft für Naturgemäße Waldwirtschaft” (Working Group for Naturalistic Forestry).

I would also like to dedicate this thesis to two special persons:

My beloved aunt, the late Dr Irmgard von Teichman und Logischen, who was very anxious that I complete this work, but unfortunately did not live to witness its completion. You will always be in my memories.

Leo, my son, you are the joy of our lives, and will hopefully be less side-tracked in your life, completing whatever you undertake in the planned timeframe

CONTENTS

TABLES

FIGURES

ABBREVIATIONS

ACS	Advanced computing system
AFRI	aerosol free vegetation index
AOI	area of interest
ARC	Agricultural Research Council
ARD	analysis ready data
AS	at surface (reflectance)
AVHRR	advanced very high resolution radiometer
BRDF	bidirectional reflectance distribution function
CART	classification and regression tree
CC	cubic convolution
CCD	charged coupled device
CD NGI	Chief Directorate National Geospatial Information
CGA	Centre for Geographical Analysis
Comp	composite
COP	conference of the parties
CSIR	Council for Scientific and Industrial Research
DD	decimal degrees
DEM	digital elevation model
DN	digital number
DSM	digital surface model
DTM	digital terrain model
EOC	Earth Observation Centre

EROS	Earth resource observation system
ESA	European Space Agency
ETM+	enhanced thematic mapper plus
EVI	enhanced vegetation index
GCP	ground control point
GLOVIS	USGS global visualisation viewer
GOFC-GOLD	global observation of forest change - global observation of land cover dynamics
GPS	global positioning system
HDF	hierarchical data format
HOT	haze optimised transformation
HRG	high resolution geometry
IAS	image assessment system
IPCC	intergovernmental panel on climate change
IRMI	image resource management information system
ISCW	Institute for Soil Climate and Water
JRC	Joint Research Council
K	Kelvin
LIDAR	light detection and ranging
LPS	Landsat-7 processing system
LPGS	level-1 product generation system
MaxNDVI	maximum NDVI value compositing technique
MaxRatio	maximum ratio compositing technique
MCD	MODIS combined product

MERIS	medium resolution imaging spectrometer
MinRed	minimum red value compositing technique
MIR	middle-wavelength infrared
MISR	multi-angle imaging spectroradiometer
MODIS	moderate resolution imaging spectroradiometer
ms	multispectral
MSG	Meteosat Second Generation
MTF	modulated transfer function
MTMRMS	multi-temporal, multi-resolution and multi-source
MVC	maximum value compositing
NDVI	normalised difference vegetation index
NIR	near-infrared
NLAPS	national Landsat archive production system
NLC 2000	national land cover 2000
NN	nearest neighbour
NNC	neural network classifications
OA	object analyst
OBIA	object-based image analysis
OSRBC	optimised spectral rule-based classification
pan	panchromatic
RADAR	radio detection and ranging
RBC	rule-based compositing
RBE	rule-based engine

REDD+	reduction of emissions from deforestation and degradation
RCC	raw computer compatible
RF	random forest
RGB	red green blue
RTM	radiative transfer model
SAC	Satellite Application Centre
SANSA	South African National Space Agency
SAR	synthetic aperture radar
SfM	structure for motion
SRC	spectral rule-based classification
SRTM	Shuttle Radar Topography Mission
SVM	support vector machines
SWIR	short wave infrared
TC1	tasselled cap component 1, brightness
TC2	tasselled cap component 2, greenness
TC3	tasselled cap component 3, wetness
TIR	thermal infrared
TM	thematic mapper
TOA	top of atmosphere
TOC	top of canopy
UAV	unmanned aerial vehicle
UN	United Nations
UNFCCC	United Nations framework convention on climate change

USGS	United States Geological Survey
UTM	universal transverse Mercator
WELD	web-enabled Landsat data
WRS	worldwide reference system

GLOSSARY

Advanced computing system (ACS): Used by SANSA EOC (previously referred to as the CSIR Satellite Application Centre) to process raw Landsat imagery. Images are converted into a standardised raw product (0Rp) from which further systematically corrected products, such as radiometrically corrected (1R) and radio and geometrically corrected (1G) images, are derived with the same software. In 2008 SANSA EOC replaced the ACS with the LPGS developed by the USGS.

Colour composite: A colour image produced by the combination of three individual monochrome images (each image is assigned a given colour). For ETM+ data, if blue is assigned to band 1, green assigned to band 2, and red assigned to band 3, a true colour image will result.

Cubic convolution (CC): A high-order resampling technique in which the brightness value of a pixel in a corrected image is interpolated with an exponential inverse distance function best characterising the point spread function of a sensor. The brightness values of the 16 pixels closest to the location of the corrected pixel on the raw image is used. If the MTF or point spread function of a sensor is not known, then this technique is the best compromise between the preservation of spatial and spectral properties of an image.

Digital elevation model (DEM): A digital data model representing elevation in raster format. A DEM can accommodate both DSM and DTM information, but is often used interchangeably with the term DTM.

Digital surface model (DSM): A digital data model, either in vector or raster format, that represents the elevation of terrain, man-made (e.g. buildings), and natural (e.g. vegetation) surface features.

Digital terrain model (DTM): A digital data model, either in vector or raster format that represents the elevation of terrain surface features.

Dynamic range: The ratio of the maximum signal to the smallest measurable signal.

Electromagnetic radiation: Energy emitted as a result of changes in atomic and molecular energy states and propagated through space at the speed of light.

Electromagnetic spectrum: A system that classifies, according to wavelength, all energy (from short cosmic to long radio) that moves harmonically at the constant speed of light.

Enhanced thematic mapper plus (ETM+): The ETM+ is a fixed-position nadir viewing whiskbroom instrument. The viewing swath is produced by means of an oscillating mirror system that sweeps across track as the sensor field of view moves forward along track due to satellite motion. It is the main payload of Landsat-7.

ETM+ scene: A set of ETM+ observations that covers 185 km in width and length and is centred on a WRS vertex.

FAST-L7A: A common data format used for the distribution of systematically corrected 1G processed ETM+ imagery.

Geometric correction: The transformation of image data, such as Landsat data, to match spatial relationships as they are on the earth. This includes correcting for band-to-band offsets, line length, earth rotation, and detector-to-detector sampling delay. For ETM+ data, a distinction is made between data that has been geometrically corrected using systematic or predicted values, and data that have been geometrically corrected using precise ground control point data and elevations models.

Global position system (GPS): A constellation of satellites in medium earth orbit that can be used to accurately determine the orbit of other satellites. These satellites transmit their ephemeris information and an accurate time measurement. With the reception of more than four satellites, any position on earth and in low earth orbit can be accurately determined by measuring the distance to these satellites via the measured time delay.

Ground control point (GCP): A geographic feature of known location, recognisable on images, that can be used to determine geometric correction functions for those images.

Image: The recorded representation of an object produced by optical, electro-optical, optical-mechanical, or electronic means. It is the term generally used when the electromagnetic radiation emitted or reflected from a scene is not directly recorded on photographic film. In digital remote sensing terms it represents a two- or three-dimensional array of measurement records, also referred to as picture elements or pixels.

Image enhancement: Any one of a group of operations that improves the interpretability of an image or the detectability of targets or categories in the image. These operations include contrast enhancement, edge enhancement, spatial filtering, image smoothing, and image sharpening.

Image transformation: A function or operation that takes an image as input, and outputs a different image. Depending on the transformation chosen, the input and output images may appear entirely different and have different interpretations. Fourier, Hadamard and Karhunen-Love, tasselled cap, principal component analysis, as well as various spatial filters, are examples of frequently-used image transformation procedures.

Infrared: Pertaining to energy in the 0.7–100 µm wavelength region of the electromagnetic spectrum. For remote sensing purposes, the infrared wavelengths are often subdivided into near-infrared (0.7–1.3 µm), middle/shortwave infrared (1.3–3.0 µm), and far/thermal infrared (3.0–15 µm). Far infrared is sometimes referred to as thermal or emissive infrared.

Irradiance: The measure, in units of power, of radiant flux incident on a surface.

Jitter: Small rapid variations in a variable (such as a waveform), due to deliberate or accidental electrical or mechanical disturbances, or to changes in the supply of voltages, in the characteristics of electrical components. Jitter effects arising from the oscillating mirrors and other movable parts aboard a spacecraft are often the cause of certain anomalies in the image data received, and must be compensated for by the ground processing software.

L0R: A raw image product with neither systematic geometric nor radiometric distortions removed.

L1G: An image processing level for which systematic radiometric (CCD calibration offsets) and geometric distortions (jitter, yaw, pitch, roll, and earth rotation and curvature) are removed.

L1R: An image processing level for which systematic radiometric distortions (CCD calibration offsets) are removed, and which is calibrated to relative radiance values.

L1T: An image processing level for which systematic radiometric (such as CCD calibration offsets with values converted to relative radiance) and site-specific geometric corrections are applied with the use of a DEM and accurate GCPs, thereby removing parallax.

Landsat-7: Consists of the spacecraft and the ETM+ payload.

Level 1 product generation system (LPGS): Software system generating level 1 products for Landsat, normally running at satellite ground receiving stations and generating products of relevance to remote sensing practitioners. The system applies systematic radiometric and geometric corrections to the Landsat data, which may entail the conversion to relative radiance or top of atmosphere (TOA) reflectance values, and the orthorectification of imagery.

Map orientated: An image processed at level L1G where the image orientation matches that of the Cartesian map coordinate system. It is also referred to as NUP (North UP). This orientation entails more resampling during L1G/L1T product generation than its counterpart, "Path orientated".

Map projection: Any systematic arrangement of meridians and parallels portraying the curved surface of a sphere or spheroid upon a plane.

Metadata: An archived set of descriptive information about a scene and the parent sub-interval that provides a user with geographic coverage, date of acquisition, sun angles, cloud cover, gain states, and other quality measurements.

Mid-wave infrared (MIR): The preferred term in the sensor response division scheme for the wavelengths in the infrared region extending from about 3 µm (visible red) to about 5 µm. The longer wavelength end of this spectrum grades into the thermal infrared. Radiation measured in this region is a combination of solar irradiance reflectance and the irradiance of the earth.

Mosaic: An image made by piecing together individual images covering adjacent areas.

Multispectral (ms): Generally denotes remote sensing in two or more spectral bands, such as visible and infrared.

Nadir: That point on the celestial sphere vertically below the observer, or 180° from the zenith.

National land cover 2000 (NLC2000): A national land cover classification of South Africa based on Landsat-7 ETM+ imagery from 2000–2002. Forty-nine classes were captured at a 1:50 000 scale by various parties.

Near-infrared (NIR): The preferred term in the sensor response division scheme for the shorter wavelengths in the infrared region, extending from about 0.7 µm (visible red) to about 1.0 µm. The longer wavelength end of this spectrum grades into the middle infrared, sometimes called solar infrared, as it is only available for use during daylight hours. Also known as the shortwave infrared (SWIR).

Nearest neighbour (NN): A low-order resampling technique in which the brightness value of a pixel in a geometrically resampled image (output image) is copied from the brightness value of the nearest pixel around the location of the resampled pixel from the input image.

Orthorectified: Describing an image property in which terrain-relief distortions induced by parallax have been removed.

Panchromatic (pan): A single band covering a broad range of wavelengths; usually used in context of collecting information from the whole visible spectrum.

Parallax: The apparent change in the position of one object, or point, with respect to another, when viewed from different angles.

Path: The longitudinal centre line of a satellite image scene, corresponding to the centre of an orbital track. Sequential numbers from east to west are assigned to 233 nominal satellite tracks for Landsat-7. Path numbers are used with row numbers to designate nominal scene centre points.

Path orientated: An image processed at level 1G where the image orientation matches that of the satellite path and not the Cartesian map coordinate system. It is also referred to as NOM (not orientated to map). This orientation entails less resampling than its counterpart "map orientated" during 1G product generation.

Phenology: A term used to describe the spectral response fluctuations of vegetation over a certain period of time, normally a season or year. This fluctuation pattern is characteristic of the specific surface type and often used for its identification using a time series of image acquisitions. Phenology is particularly important for the identification of different vegetation types.

Pitch: The rotation of a spacecraft about the horizontal axis normal to its longitudinal axis (in the along-track direction) so as to cause a nose-up or nose-down attitude. This is also referred to as the X-axis.

Pixel: Picture element provided by a single detector scene sample output.

Pre-processing: All the processing undertaken on raw satellite imagery to bring it to a state where quantitative image analysis can be directly performed on the imagery.

Radian: The angle subtended by an arc of a circle equal in length to the radius of the circle. One radian equals 57.3°.

Radiance: A measurement of energy radiated by an object. In general, radiance is a function of the viewing angle and spectral wavelength, and is expressed as energy per solid angle.

Radiative transfer model (RTM): A physical atmospheric correction whereby the transfer of electromagnetic radiation through the atmosphere is modelled under known atmospheric conditions.

Rayleigh scattering: Selective scattering of light in the atmosphere by particles that are smaller than the light wavelength.

Reflectance: The ratio of the radiant energy reflected by a body to the energy incident upon it. In general, reflectance is a function of the incident angle of the energy, viewing angle of the sensor, spectral wavelength and bandwidth, and the nature of the object.

Registration: The process of geometrically aligning two or more sets of image data, such that pixels for a common ground area can be digitally or visually superimposed.

Roll: The rotation of a spacecraft about its longitudinal axis (in the along-track direction) so as to cause a side-up or side-down attitude. The roll axis is referred to as the Y-axis.

Row: The latitudinal (nominal) centre line of a Landsat scene. Row 1 is at latitude 80° 47'N, row 60 is at the equator, and row 122 is at latitude 81° 51'S. In total there are 248 rows.

Saturation: The condition where energy flux exceeds the sensitivity range of a detector.

Shortwave infrared (SWIR): The preferred term in the sensor response division scheme for the shorter wavelengths in the infrared region extending from about 1.0 µm (visible red) to about 3.0 µm. This spectrum grades into the middle infrared, sometimes called solar infrared, as it is only available for use during daylight hours.

Shuttle Radar Topography Mission (SRTM): A NASA space shuttle mission in 2000 carrying C and X band SAR instruments with two antennas, acquiring inferometric imagery for the major landmasses of the world to derive digital elevation models at different resolutions (90 m C-SAR public domain, 30 m C-SAR non-disclosed product and incomplete 12.5 m X-SAR).

Spectral band: An interval in the electromagnetic spectrum defined by two wavelengths, frequencies, or wave numbers.

Spot: A French satellite constellation consisting of Spot 1–3 (HRV), 4 (HRV-IR & VEGETATION), 5 (HRG, HRS & VEGETATION), and 6–7 (NAOMI) with the respective instruments on board.

Sun elevation angle: The angle of the sun above the horizon.

Solar zenith angle: Reciprocal of the sun elevation angle.

Sun synchronous: An earth satellite orbit in which the orbital plane remains at a fixed angle with respect to the sun, progressively wandering 360° during the period of a year to maintain this relative position.

Swath: Refers to the 185 kilometre wide ETM+ imaging ground track.

Temporal resolution: The expected repeat time between measurements over the same location.

Thermal band: A general term for intermediate and long wavelength infrared-emitted radiation, as contrasted to short wavelength reflected infrared radiation. In practice, it generally refers to infrared radiation emitted in the 3–5 µm and 9– 4 µm atmospheric windows.

Thermal infrared: The preferred term for the long wavelength ranges of the infrared region extending roughly from 8 µm at the end of the mid-wavelength infrared, to about 15 µm where the far infrared commences. In practice, the limits represent the envelope of energy emitted by the earth behaving as a grey body with a surface temperature around 290 K.

Universal Transverse Mercator (UTM): A widely used map projection employing a series of identical projections around the world in the intermediate latitudes, each covering six degrees of longitude, and orientated to a meridian. The UTM projection is characterised by its property of conformity, meaning that it preserves scale and angular relationships well, and easily allows a useful rectangular grid to be superimposed on it. For Landsat data, UTM is the most commonly used projection.

Visible radiation: Electromagnetic radiation of the wavelength interval to which the human eye is sensitive; the spectral interval from approximately 0.4 to 0.7 µm.

Wavelength: Wavelength = 1/frequency. In general, the mean distance between maximums (or minimums) of a roughly periodic pattern. Specifically, the shortest distance between particles moving in the same phase of oscillation in a wave disturbance.

World geodetic system: The reference earth model used by the Landsat-7 system.

Worldwide reference system (WRS): The indexing system used for Landsat scenes defined by path and row.

Yaw: The rotation of a spacecraft about its vertical axis, so as to cause the spacecraft's longitudinal axis to deviate left or right from the direction of flight. The yaw axis is referred to as the Z-axis.

Zenith: The point in the celestial sphere that is exactly overhead.

CHAPTER 1: SETTING THE SCENE

1.1 FORESTS: AN ESSENTIAL NATURAL RESOURCE

Humans are different from other species in that they are able to modify their physical environment for protection against the elements of nature. The ability to adapt our local conditions to provide a better habitat has led to a population explosion, and has modified the environment of all other species, often to their detriment. To maintain humans' artificial habitats and infrastructure, and to prevent it from reverting to its natural state, energy is needed – derived from renewable and non-renewable resources. The use of non-renewable resources is inherently not sustainable and, in the case of fossil fuels, produce waste products that negatively affect the global environment. Renewable resources, on the other hand, all derive their energy ultimately from the electromagnetic radiation of the sun (Hinckley 1980).

Carbon, oxygen, and hydrogen are the most important elements that absorb and release energy at different molecular combinations. Here, the carbon cycle is of foremost importance. Carbon in its pure form can react with oxygen at different ignition temperatures, forming mainly carbon dioxide (CO_2) to release energy. Carbon dioxide, in turn, together with water, can store energy from the sun during photosynthesis in plants, and produce hydrocarbon compounds with oxygen (O_2) as a by-product. A fine balance of oxygen and carbon dioxide concentrations regulates the amount of thermal radiation that is captured in the earth's atmosphere, which in turn controls its surface temperature. This temperature is optimally between 10–30°C. An increase of carbon dioxide, together with other hydrocarbons such as methane (referred to as greenhouse gases), increases the amount of thermal radiation trapped in the atmosphere and further heats up the earth's surface. This process is called global warming, and it rapidly changes the natural environment, making it difficult for man to maintain his own adapted habitat (Houghton 1997).

Forests consist of plants that are able to effectively convert carbon dioxide into hydrocarbons and oxygen, binding these hydrocarbons for an extended period of time into large volumes of woody biomass. They are, therefore, referred to as carbon sinks, and are vitally important to maintaining a favourable balance between oxygen and carbon dioxide in the atmosphere. The stored carbon can also be seen as a renewable resource, as it is constantly replenished as long as the forests remain functional (Valentini 2003).

Forests can be classified into five broad climatic groups (Figure 1-1) with different levels of resilience to human utilisation. These groups, according to the World Commission on Forests and Sustainable Development (Salim & Ullsten 1999), are:

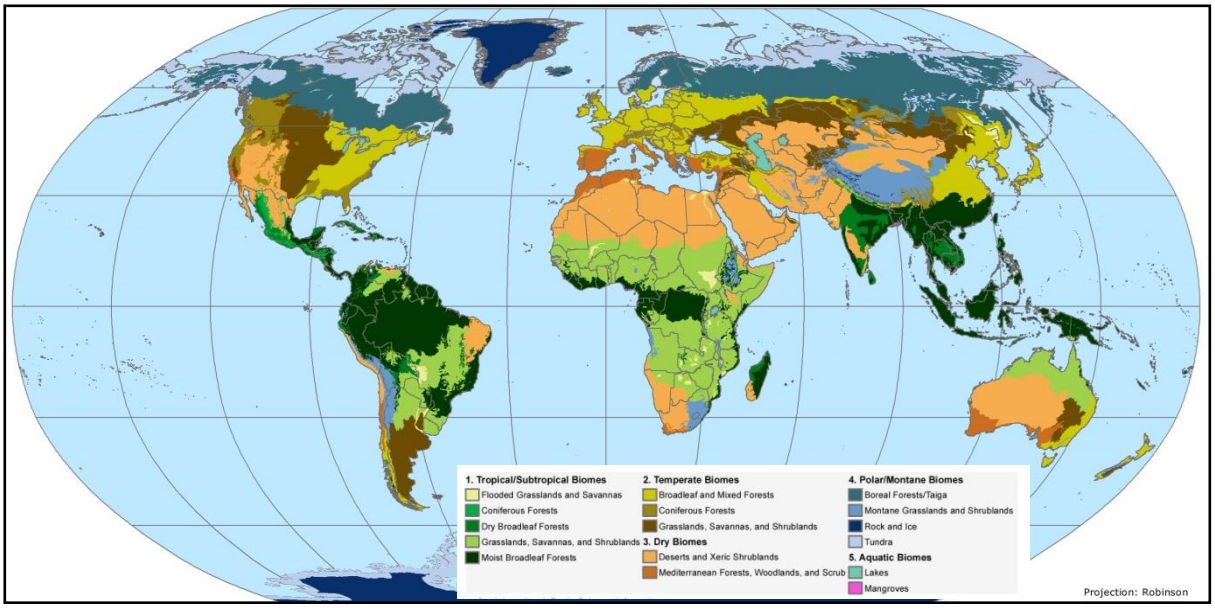

Source: Adapted from Anonymous (2013)

Figure 1-1 Global biomes with special reference to forest types

Boreal forests occur in climatic zones between 50°N and 70°N with mean annual temperatures ranging from -5° to 5°C, and low rainfalls. These forests are slow-growing, with a low above ground carbon stock and a relatively large below ground carbon stock. They are composed of species that are relatively resilient to human utilisation, as timber harvesting can have a similar impact on forests as that of natural disturbances such as fire and insect infestations (the natural drivers of the ecosystem). Sustainable utilisation, however, has to take into account the long successional cycles, which can be several hundred years, as this limits the amount of timber that can be harvested.

Temperate forests occur in climatic zones between 30°N/S and 50°N/S with a mean annual temperature ranging from 5 to 15°C. These are generally the most productive natural forests in terms of utilisable timber, but they occur in regions with dense population where there is great pressure to see land converted to other uses, particularly agriculture and urban settlements.

Mediterranean forests are restricted in growth due to a dry summer, and are susceptible to fire. They are of minor importance to forestry due to their small geographic extent.

Subtropical forests occur in climatic zones between 10°N/S and 30°N/S, and may experience one or two rainy seasons, with one being distinctively more pronounced in summer. The dry season(s) usually spans several months. Rainforests in these areas receive an even distribution of rain, in excess of 800 mm, and are largely evergreen. They cover a small area, and are often relicts of a wetter climatic period. They are of low productivity and therefore not resilient to human utilisation, and once destroyed, they seldom recover. Dry subtropical forests have a low

biomass and a dominant herbaceous component. They have a tree cover of as low as 10% according to the definition of the Food and Agricultural Organisation (FAO 2015). Savannahs are included in this class, and cover a large landmass. They are extensively utilised by humans in often poor and industrially underdeveloped regions of the world, and are frequently associated with rapidly expanding rural populations. Due to the large area they cover, they are important carbon pools and sinks that are, however, rapidly being degraded. In subtropical areas with a rainfall exceeding 800 mm, plantation forests are profitable and provide the highest productivity of utilisable timber – between ten to 100 times that of natural forests – as well as being important carbon sinks. Plantation forests, although often represented by exotic species, have the lowest environmental impact of all intensive human land uses. They produce renewable resources that would otherwise have been harvested from a much larger area of natural forest, often in an unsustainable manner (Bredenkamp & Upfold 2012). They further counteract the effects of global warming by reducing the ambient temperature at a microclimatic scale of up to 30°C, as measured in irrigated popular plantations in the Columbia River basin in Oregon, USA (Przyborski 20013).

Tropical rain forests are found along the equatorial belt and receive rainfall throughout the year, with moderate variations in seasonal intensity. They often grow on nutrient poor soils, recycling essential nutritional elements such as nitrogen, phosphorous, and potassium effectively. The abundant supply of water, sunlight, and temperature, in addition to a nutrient deficiency, have provided many niches and lead to the evolutionary development of tremendous diversity in species. Tropical forests provide by far the highest carbon sinks of all forest types and host the highest timber volumes, although they do not have the highest timber productivity. They are moderately resilient to timber utilisation and tend to recover quickly from harvesting activities, provided that these activities are limited to small patches. Large clear-cuts lead to heavy erosion and a rapid nutrient depletion of the soil. Large areas of tropical forests have been over-utilised and lost through deforestation over the past three decades. Although a decline in deforestation rates have been recently observed in the Amazon (Fearnside 2003), tropical forest cover in Indonesia, Malaysia, and Central Africa is still rapidly declining, leading to a loss of species and additional release of carbon dioxide to the atmosphere, thereby enhancing global warming (Freer-Smith, Broadmeadow & Lynch 2007).

The conservation of forests, or sustainable use thereof, can thus be supported with arguments from the instrumental and intrinsic value theories of environmental ethics (Hargrove 1989). Instrumental values include the arguments of the cathedral (forests are used for recreation of the soul), gymnasium (forests are used to practice sports), silo (forests are a renewable natural resource), and laboratory (forests and their species diversity provide many uses and benefits to man that have not yet been researched or discovered).

From the arguments presented above, the motivation to conserve and sustainably use forests is well founded and should be the priority of the international community, national governments, industries, and local communities. Several international initiatives have been launched in this regard, especially focussing on the principles of carbon trading. These initiatives accommodate industrialised nations emitting large volumes of carbon dioxide, while paying underdeveloped or emerging countries with sufficient afforested areas for not overexploiting these resources (Kollmuss 2010). Projects to facilitate carbon trading have been defined at several conventions starting with the Kyoto protocol and Rio convention (1992), and leading to the Rio +10 summit (2002), and several Conference of the Parties (COP) meetings. The most recent conferences included the United Nations (UN) series of climate change conferences, in particular of the United Nations framework convention on climate change (UNFCCC), of which a significant meeting was held in Durban, South Africa in 2011. During the UNFCC meetings held between 2005 and 2007, a project called *Reduction of emissions from deforestation and degradation plus* (REDD+), supported by the World Bank, was initiated. This project provides a mechanism for developing countries with substantial forest resources and proven decelerated, halted or reversed deforestation processes to trade the amount of carbon not lost or that is gained with industrialised nations. It is a good example of the positive sides to environmental economics as described by Anderson (2010). The group for global observation of forest change and global observation of land cover dynamics (GOFC-GOLD) published a book that guides countries participating in REDD+ in the use of remote sensing for their relevant reporting while adhering to the Intergovernmental panel for climate change (IPCC) guidelines by Achard (2012). Considering the value of forests as a natural resource, information on this natural resource is needed, which can be submitted to governments, NGOs, and the forestry industry. The next section will discuss the requirements of spatial information for this purpose in greater detail.

1.2 GEOINFORMATION PRODUCTS FOR SUSTAINABLE FOREST MANAGEMENT

The sustainable management and use of forests can be achieved when the value of use exceeds the value of the input/contributions required to achieve this use (Gadow, Pukkala & Tomé 2000). Utilisation is sustainable when forest resources fluctuate with natural cycles and do not exceed that of a natural fluctuation. The cost of using forestry resources and the cost of ensuring sustainability in the use thereof can be dramatically reduced with the acquisition of geoinformation products that describe the environment, forest resources, and surrounding infrastructure. These geoinformation products can be used for strategic (long-term), tactical (mid-term), and operational (short-term) planning (Sample 1994).

Information products for strategic use describe the physical environment in which forests grow, which in turn determines their natural composition or allows for finding optimal site-species matches. Spatial information for long-term infrastructure planning is also included in information products. Strategic planning is undertaken for a timeframe of approximately 20 years and beyond, depending on the climatic conditions. Information products typically consist of the following spatial datasets, usually in geographical information system (GIS) format (Thwaites 2002):

- Climatic conditions, providing information on annual rainfall and rainfall distribution, as well as the occurrence of other forms of precipitation (such as snowfall and hail), temperature means and extremes, summary of extreme wind conditions, fire events, and sunlight duration and intensities;
- Underlying geology and derivative soils, including descriptions of soil horizons in terms of clay concentration and types, fragment structure, and ion and nutrient concentrations, together with the effective rooting depth;
- Digital elevation models (DEMs) for the description of microclimatic variables, access costs, sun exposure, and soil stability;
- Flora/vegetation maps describing the natural composition of plant species in an environment with and without anthropogenic presence;
- Natural distribution of fauna/animal species maps;
- Long-term conservation plans based on specie distribution, vulnerability, indemnity, and the requirement of corridors for facilitating natural migration patterns and genetic exchange for both fauna and flora; and

- Optimal road network and other related infrastructure.

Products of tactical value describe medium-term trends (5–20 years) in forest and infrastructure development required for the exploitation and use of forests (Köhl, Magnussen & Marchetti 2006). They include:

- Land cover/use datasets and modelled data on future land cover/use changes based on past change events – these datasets aid in the formulation of legislation and laws for the protection of forest resources;
- Age distribution and geographic location of plant/tree communities at different successional stages as demonstrated by Dye, Mutanga & Ismail (2012) and Dye, Mutanga & Ismail (2011);
- Distribution of current growth, yield, and carbon/timber growing stock as demonstrated by Dube, Mutanga, Elhadi & Ismail (2014) using RapidEye imagery for the estimation of intra- and inter-species biomass prediction in a plantation forest;
- Timber quality and properties such as the amount of knot-free timber, the presence of reaction wood, other growth defects, and the content of lignin (important for the pulp and paper industry);
- Distribution of product ranges to be harvested from the forests, and associated medium-term harvesting and utilisation plans;
- Plans for the conservation of species and the recreational use of forests;
- Current ranges of fauna species and population densities;
- Maintenance and construction plans of infrastructure (such as roads and processing plants) for the extraction and processing of timber and non-timber forest products; and
- Planning of fire, wind, and pest infestation breaks for the protection of forests as illustrated by Poona & Ismail (2013) for pitch canker in *Pinus radiata* and Ismail et al. (2008).

Spatial information is required for operational day-to-day management and short-term adjustment of utilisation plans for a time span of up to five years. This is linked, somewhat, to aspects of tactical planning described previously (Beaudoin, Frayret & LeBel 2008), and may include:

- Monitoring and recording of the spatial distribution of weather events such as droughts, floods, snowfall, frost, hail, and wind damage that affect forest health and impact harvesting activities;
- Spatial location of active fires in conjunction with fire-spread models, and the mapping of fire scars and severity of a fire event;
- Detection of forest pests, and the area and severity of the infestation, as well as the rate of spread;
- Adaptation of forest utilisation plans based on unforeseen biotic and abiotic drivers as listed above;
- Detection of unforeseen land cover/use change or illegal/unplanned forest utilisation for the enforcement of legislation to protect forest resources; and
- Detection and mapping of growth anomalies and stress due to the wide range of factors mentioned above.

Now that the spatial information required for the sustainable management of forests has been clarified, methods of obtaining this information will be briefly discussed in the next section. Emphasis is placed on remotely sensed data as it is a relatively inexpensive and consistent data source (Franklin 2001).

1.3 REMOTE SENSING TECHNOLOGIES AND METHODS

A wide range of methods exist for generating geoinformation products for the sustainable management of forest resources. These methods can be broadly categorised as 1) manual in-field (in situ) measurements; and 2) automated or semi-automated remote sensing methods (Franklin 2001). In-field measurements entail the use of traditional surveying methods such as soil sampling and laboratory analyses, stand mensuration and species classification, and enumeration techniques, as well as location-based measurements such as those recorded by weather stations, manned observation towers, and autonomous flux towers (Von Gadow & Bredenkamp 1992). Automated or semi-automated remote sensing methods are more autonomous, but may require some in situ measurements for interpretation, calibration, and accuracy assessment (Ozdogan & Schumann 2014).

This study is focused on the use of fully-automated remote sensing techniques for the generation of forestry-related geoinformation products. Ground-based remote sensing techniques, such as oblique photography from elevated vantage points, panoramic and hemispheric photography in

sample plots, and ground-based light detection and ranging (LIDAR), will not be considered. The focus will instead be on sensors mounted on airborne and spaceborne platforms, as they provide overhead perspectives that can be easily related to other spatially referenced information.

Imaging sensors can be grouped into active and passive systems. The following subsections provide an overview of each of these sensor types.

1.3.1 Active sensors

Active sensors illuminate the target with electromagnetic radiation and record the radiation properties and intensities scattered back from the illuminated objects (Campbell 1996). Examples of active remote sensing systems useful for forestry are LIDAR and synthetic aperture radar (SAR). Each of these technologies is discussed in the following subsections.

1.3.1.1 LIDAR

LIDAR consists of a sensor that transmits a light pulse in-between the visible and near-infrared range, interacts with the vegetation, and is partially scattered from the vegetation canopy or from within the crown or the underlying ground before returning back to the sensor. The time delay between transmission and reception is used to determine the distance between the sensor and surface responsible for the scattering (Vierling et al. 2011). Low-end LIDAR systems only transmit radiation in one wavelength, and measure first, limited intermediate and last returns of a pulse, while more sophisticated systems transmit in multiple frequencies and/or measure the full return wave from many scattering events of a pulse. The latter is referred to as wave form LIDAR, and is favoured by Asner, Levick & Cleland (2012). LIDAR is used to derive accurate digital surface models (DSMs) and digital terrain models (DTMs) (Mongus & Zalik 2012). The difference between a DSM and DTM can be used for the estimations of tree height and crown diameter (Vaughn, Asner & Giardina 2013). Wave form LIDAR can additionally be used for the assessment of structural crown profiles, which provides good correlations with overall biomass and stem volume (Vierling et al. 2011).

1.3.1.2 SAR

SAR is a side-looking radio detection and ranging (Radar) instrument that uses the movement of the platform and the resulting Doppler shift of the returning signal to resolve a two-dimensional image, thus synthetically simulating a long antenna described by Elachi & Van Zyl (2006). SAR systems transmit radiation at frequency bands Ka, K, Ku, X, C, S, L, and P (Table 1-1). Shorter frequencies enable higher spatial resolutions, but reduce the ability of the signal to penetrate

vegetation and soil. SAR signals can be sent and received at various combinations of polarisation (Van Zyl & Kim 2011).

Table 1-1 Radar wavebands and nomenclature

Band designation	Frequency (MHz)	Wavelength (cm)
P	300–1000	30–100
L	1000–2000	15–30
S	2000–4000	7.5–15
C	4000–8000	3.75–7.5
X	8000–1200	2.5–3.75
Ku	12000–18000	1.667–2.5
K	1800–27000	1.111–1.667
Ka	27000–40000	0.75–1.111

Source: Mather (2004)

To generate an image, two components of a SAR signal are measured. The first is the intensity of the signal and the second is the phase (Oliver & Quegan 2004). A change in polarisation and the distribution of changed to unchanged polarisations provide an indication of the surface structure (Van Zyl & Kim 2011). An unchanged polarisation indicates a flat surface with the signal interacting with the surface only once. A polarisation change indicates interaction of the signal with a horizontal and vertical surface, causing a double bounce return. An even distribution of polarisation (when both vertically- and horizontally-sent signals change) for signals transmitted in the C, S, and L bands indicates a volumetric scattering of the surface (e.g. dense tree crowns). The technique of separating the scattering mechanisms is called polarimetric decomposition and can be used to derive biomass with moderate success (Dickinson et al. 2013). The strength of a return signal is an indication of the moisture content, surface roughness, and the slope of the surface. Attempts to derive woody biomass from the intensity of a signal under uniform moisture and slope conditions have proven successful only at low biomass levels and long frequencies (Mathieu et al. 2013). For most forest types (excluding sparse savannahs), intensity readings from the P band alone do not saturate and are therefore useful for biomass estimations (Guyon 1992). The phase of the returned signal can be used for interferometric analysis provided that two measurements at almost the same angle, but with different baselines, have been made. This is possible either with two receiving antennas spaced a certain distance (baseline) apart, or two consecutive acquisitions with the sensor path parallel but slightly displaced to the previous acquisition (Hanssen 2001). The first measurement scenario is referred to as single pass interferometry, while the second is called repeat pass interferometry. Single pass interferometry has the advantage of having no temporal decorrelation between the phases, whereas this is the case with repeat pass interferometry (Duque, Lopez-Dekker & Mallorqui 2010). With two phases, a phase shift can be calculated with an interferogram, which, when flattened and

unwrapped, can be converted to a surface model (Hanssen 2001). The shuttle radar topography mission (SRTM) (as investigated by Van Zyl (2001)) and TanDEM-X (by Krieger (2007)) are SAR examples of single pass interferometric missions with the aim of generating a global DEM. The TanDEM-X satellite mission is generating an almost true DSM, as little of the signal is able to penetrate vegetation canopy.

Decorrelation between two complex interferometric SAR datasets, also referred to as coherence, can be attributed to different penetration levels of the two signals (Tansey et al. 2004). Coherence of both repeat pass and single pass interferometry can consequently be correlated to biomass and, in particular, woody biomass (Sinha et al. 2015). Santoro et al. (2007) demonstrated a repeat pass interferometric approach at a high spatial resolution (30 m) for a large area (more than 8 million km^2) in Siberia and China. The German Space Agency (DLR) and other scientists are currently developing a similar approach using TanDEM-X data (Garestier, Dubois-Fernandez & Papathanassiou 2008). Combinations of interferometry and polarimetry, referred to as PolInSAR, exist and are promising for the derivation of geoinformation products for forestry (Li et al. 2014).

1.3.2 Passive sensors

Passive remote sensing sensors measure electromagnetic radiation reflected or emitted by an object or the earth's surface (Campbell 1996).

1.3.2.1 Measuring emitted energy

The distribution of radiation frequencies from either the sun or other bodies is determined by the temperature, commonly measured in Kelvin (K), and the emissive properties of the body. Emissive properties are described in terms of conformity to the emissive radiation distribution curve of a black body, which transforms heat energy into radiant energy, at the maximum rate conforming to the laws of thermodynamics described by Honig (1999). A black body and grey body produce a smooth skewed curve when plotting radiance, measured in $Wm^{-2}\mu m^{-1}$, with the grey body differentiating itself from the black body by lower emissive properties. The ratio between black body radiation and grey body radiation is called emissivity. Selective radiators have emissivity properties that are wavelength dependent. The distribution curve of temperature dependent black body radiation across wavelength can be described by Planck's Law formulated in Equation 1-1.

$$M_\lambda = \frac{c_1}{\lambda^5 (exp[c_2/\lambda T] - 1)}$$

Equation 1-1

where c_1 is the constant 3.742×10^{-16}Wm^{-2};

c_2 is the constant 1.4388×10^{-2}mK;

λ represents the wavelength in m;

T represents the temperature of the object in K; and

$M\lambda$ is the spectral exitance per unit wavelength.

The electromagnetic radiation emitted by the sun has a mean estimated temperature of 5777 Kelvin (K) and is therefore of relevance to passive remote sensing, as it is the origin of emitted radiation that, in turn, is reflected from the earth's surface. The radiation incident to and reflected from the earth's surface is partially absorbed by the atmosphere (illustrated by Figure 1-2). Radiation, therefore, ranges from 0.3µm (ultra-violet) and 0.4–0.76µm (visible), peaking at 0.47µm (visible green), to then decrease over 0.76–1.3 µm (near-infrared or NIR), 1.3–3.0 µm (shortwave infrared or SWIR), and 3.0–5 µm (middle/thermal infrared).

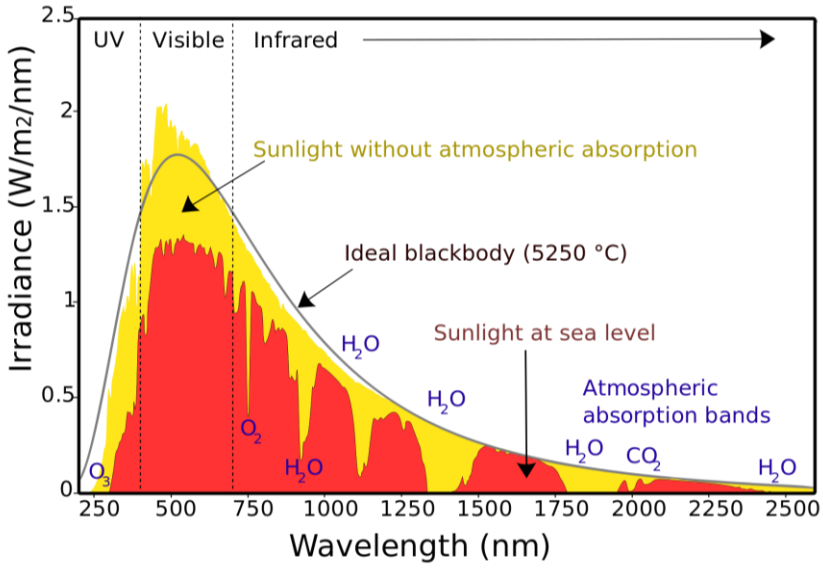

Source: Adapted from Josh (2017)

Figure 1-2 Irradiance from the sun compared to radiation penetrating the atmosphere from the ultra-violet to the shortwave infrared range of the electromagnetic spectrum (absorption bands illustrated with the atmospheric gases that are responsible).

It becomes evident, therefore, that even small amounts of middle infrared radiation emitted by the sun will contaminate thermal measurements during the day, which is why we refer to thermal day measurements as acquired by Landsat as brightness temperature. Thermal infrared is sometimes referred to as emissive infrared when emitted by the earth at temperatures around 290K (Mather 2004). The thermal bands of remote sensing sensors are useful for forestry applications to not only detect fires, but can also be used to model evapotranspiration rates. Fires

pose a major threat to forests, and the early detection of active fires using imagery from MODIS sensors (aboard Aqua and Terra satellites) and the MSG satellite aid in their management (Moodley, Simonis & Tapamo 2012). The modelling of evapotranspiration rates provides insight into water use efficiency, productivity, and health of forests (Wu et al. 2006). Emitted radiation which strikes a surface interacts with that surface by either being absorbed (adding energy to the surface) or reflected back into space. The next section will deal with the reflected radiation.

1.3.2.2 Measuring radiance and reflectance

Since measuring the reflective property of a surface is the goal of shortwave passive remote sensing, a normalisation of measured radiance is required for quantitative analysis. Radiation emitted by or reflected from a surface is measured as radiance by a sensor. Radiance represents the energy per area of the surface and solid angle of the sensor in relationship to the surface geometry. Radiance is measured in Watts per square meter (surface area) per sterradian (solid angle) per micrometre (wavelength), which is abbreviated as W $m^{-2}sr^{-1}\mu m^{-1}$ (Liang 2004). The units for the different components of radiance vary in the literature (Liang 2004). The amount of radiation reflected from a surface relates to the radiation intensity the surface is subjected to, and the reflection properties of the surface. This normalised variable is called reflectance, which is the ratio of measured radiance to potential radiance at full reflection. Potential radiance at full reflectance is dependent on the average radiation intensity of the source (sun) for a certain wavelength, the distance between the source (sun) and target (earth), the general shape of the target (i.e. spherical in the case of the earth), and the illumination angle (solar elevation angle). Reflectance can thus be described by Equation 1-2 (Mather 2004).

$$\rho = \frac{\pi L d^2}{E_s \cos \theta_s}$$ Equation 1-2

where
- ρ is reflectance;
- π is scattering from a spherical surface;
- L is measured radiance by the sensor;
- d is the distance between the earth and the sun measured in astronomical units;
- Es is exoatmospheric solar irradiance at a distance of one astronomical unit between the earth and the sun for a given wavelengths; and
- θs represents the solar zenith angle.

The distance between the earth and the sun can be measured roughly in astronomical units using Equation 1-3 (Mather 2004).

$$d = 1 - 0.01674\cos\left(0.9856(JD - 4)\right)$$ Equation 1-3

where d is the distance between the earth and the sun measured in astronomical units; and

JD defines the Julian day interpreted as day of the year starting with 1 January and ending with 31 December.

With the normalisation of measured radiance values to reflectance values, reflective properties of surfaces can be described quantitatively. Changes in these reflective properties due to changes in chemical processes, such as photosynthesis in plants over time, can be accessed quantitatively by comparing two radiance observations normalised to reflectance, which corrects the varying radiation intensities the surface has been exposed to during consecutive observations. Any automated classification approaches relying on quantitative spectral observations, as is the case in this study, rely on radiation values normalised to reflectance. Reflectance measurements are therefore the foundation of passive quantitative remote sensing (Baraldi 2009), with the exception of thermography and aeromagnetic imaging (Muundjua et al. 2007). The accuracy of reflectance measurements can be affected by the atmosphere between the source (sun), object reflected from (forest), and sensor measuring the reflected radiation. The next section explains atmospheric effects on radiance measurements.

1.3.2.3 Atmospheric effects

The earth's atmosphere interacts with incoming and outgoing radiation before it is recorded by sensors, mainly in the form of absorption (outside atmospheric windows) and scattering (Friedlander 2000). Absorption of short wavelengths is attributed to ozone (O_3) concentrations and affects ultra-violet and blue radiation, while water vapour absorbs radiation in the SWIR and thermal infrared regions of the electromagnetic spectrum described by Ho, Smith & Huang (2002). This type of scattering is dependent on the size of the molecule interacting with the radiation and the wavelength of the radiation (Hanafy, Roggemann & Guney 2014). Very small particles with sizes much smaller than the wavelength cause Rayleigh scattering. The effect of this type of scattering is inversely proportional to the fourth power of the wavelength, which implies that only short wavelengths are affected, and scattering takes place forward, away from the source. Mie scattering is caused by particles of more or less the same size as the wavelength concerned. Its scattering effect is also inversely proportional to the wavelength, but to a much lesser degree than Rayleigh scattering. Mie scattering takes place forward and backward and occurs only in the lower parts of the atmosphere where larger suspended particles are normally present. A third type of scattering, namely non-selective scattering, is wavelength independent

and is caused by very large molecules and suspended particles (e.g. soot), that are much larger than the affected radiation's wavelength. Non-selective scattering takes place in all directions in equal proportions, and is described by Mather (2004), Nair et al. (2009), and Chuvieco & Huete (2010).

Atmospheric effects such as absorption and scattering should ideally be taken into account when calculating the reflectance properties of objects on the earth's surface. When these effects are taken into account, the measurements are referred to as top of canopy (TOC) or at surface reflectance. However, many remote sensing applications disregard atmospheric effects. Such measurements are referred to as top of atmosphere (TOA) or at-sensor reflectance (Baraldi 2009).

The accuracy of a measurement is related to the factors that distort it, such as atmospheric effects in the case of the measurement of radiation intensities as radiation passes through the atmosphere as discussed above. Accuracy is also dependent on the resolution or sampling interval at which the measurement takes place. Resolution is, therefore, discussed in greater detail in the following section.

1.3.2.4 Resolution

Passive remote sensing sensors have been designed to take measurements of electromagnetic radiation at different resolutions, and can be categorised into the following observation types (Liew 2013):

- *Panchromatic sensors* that measure radiation in one wide spectral band at high spatial resolution. The extraction of textural and contextual information is the main application of such observations. This was the main driving force for the mission definition of the American Corona surveillance satellites, producing imagery at resolutions of 2–3 feet in the 1960's (Fowler 2011).
- *Multi-angular sensors* that take measurements of the same surface at different angles almost simultaneously. This angular resolution allows for the characterisation of the bidirectional reflectance distribution function (BRDF), whereby different surfaces reflect light into different directions at different intensities and wavelengths. A classic example of such a system is MISR on board the Terra satellite. It acquires imagery at nine different angles, with which structural parameters of vegetation can be assessed (Gobron et al. 2002).

- *Multispectral sensors* measure radiation in different bands of the electromagnetic spectrum. This type of sensor addresses the fact that surfaces of interest are characterised by their band-specific characteristics to absorb, reflect, and transmit fluorescent radiation. Generally, sensors with two to ten spectral bands are referred to as multispectral, 11–100 spectral bands as super-spectral, and more than 100 spectral bands as hyperspectral. An example of a hyperspectral sensor in space is Hyperion. Spaceborne hyperspectral sensors for vegetation studies have not been used for operational applications, but rather for research as they produce large volumes of data over small areas at coarse spatial resolutions (Govender, Chetty & Bulcock 2007). An example of a super-spectral sensor is ESA's Sentinel-2 satellite, which delivers operational data useful for vegetation studies (Frampton et al. 2013).

Sensors dedicated to the acquisition of systematic multi- and hyper-temporal acquisitions are often carried in a constellation of satellites with relatively wide swath widths, often to the detriment of either spatial or spectral resolution. These sensors are used to measure and characterise the radiation and reflectance fluctuations in different spectral bands of diverse surface types. These characteristics, also referred to as phenology, are of particular relevance to the characterisation of vegetation, where growth, photosynthesis, and evapotranspiration processes are closely linked to seasonal environmental variables, such as temperature, water, light, and nutrient availability. An example of such a system is MODIS, deployed on the two satellites Aqua and Terra, which cover the globe up to twice daily. MODIS data is used extensively for the characterisation of vegetation phenology as described by Tang (2013).

From the range of resolutions described above, a multitude of techniques can be developed, and several techniques have partially been developed to extract thematic information from remotely sensed imagery. The next section will touch on some of these techniques.

1.4 REMOTE SENSING PRODUCT GENERATION

Three approaches to the analysis and extraction of geospatial information from remotely sensed imagery exist. These approaches are outlined in the subsections to follow, and have developed in an evolutionary process from manual qualitative image interpretation to fully automatic quantitative analyses.

1.4.1 Manual image interpretation

The first approach entails manual image interpretation combined with either on-screen or tablet-based digitisation. This method is very labour intensive as it relies entirely on the cognitive skills

of the image interpreter, who would normally visualise the data in one (panchromatic) to three (true colour or false colour composites) spectral bands. Imagery used for this technique does not have to be radiometrically normalised (and can in fact be of poor radiometric quality), but it is generally of higher spatial resolution, providing information (such as texture) to enhance cognitive interpretation. Several large land cover products, such as CORINE and SIOSE, were generated with manual photo interpretation (Perez-Hoyos, Garcia-Haro & Valcarcel 2014). This approach is often applied to rare or expensive data, or when the availability of computing power or software is limited. South Africa's first national land cover product was generated in 1996 using this approach, mainly due to the availability of only single date images acquired over different seasons and the lack of computers powerful enough to process the large volumes of data (Thompson et al. 2001). Manual image interpretation is often applied to forestry applications when global products must be derived from high resolution imagery (e.g. the global land cover survey based on Landsat data) or where slight disturbances in forests have to be identified with sparse or inconsistent multi-temporal datasets (Pflugmacher, Cohen & Kennedy 2012).

1.4.2 Supervised statistical image classification

Statistical classifiers can be used to mathematically discriminate between classes of interest with sufficient statistical significance under the following conditions:

- Remote sensing imagery is of high quality;
- Radiometric normalisation within a scene is sufficient; and
- Spectral and radiometric resolution is sufficient.

This classification type is moderately to highly computation and labour intensive and requires operators who understand some basic concepts of statistics and spectral properties of the classes of interest. Statistical classifiers are normally applied to remote sensing imagery on a scene-by-scene basis, using either unsupervised classification and clustering techniques (which require thematic recoding at a second stage), or supervised classification techniques (which require the collection of training samples to statistically characterise the spectral properties of classes of interest). Statistical classifiers are currently being used as the norm by most remote sensing practitioners as they can provide the highest level of detail and accuracy as long as the imagery is of good quality, samples are selected diligently, and classes of interest can be described statistically by the imagery. The South African National Land Cover (NLC) 2000 project was based on this technique using high quality, bi-seasonal Landsat-7 ETM+ imagery, which enabled

it to achieve a much higher level of detail than the NLC 1996 product, as described by Lück (2004). Wulder (2008) applied such a technique for land cover mapping of Canada, whereby imagery was first normalised to TOA reflectance and an NDVI was calculated to stratify imagery into four broad classes including water, non-vegetated, low-reflectance vegetation, and high reflectance vegetation. These strata were then subjected to a K means unsupervised classification and recoded manually into final classes.

1.4.3 Automated rule-based image classification

Fully-automated rule-based image classification techniques are the "holy grail" of the remote sensing community as they allow the extraction of thematic information from imagery automatically, at almost no cost. This approach becomes particularly relevant with the availability of huge amounts of high quality, systematically acquired, multi-temporal remote sensing data, including NOAA, Spot Vegetation, MODIS data, and the freely available Landsat 5,7, and 8 imagery from the USGS and Sentinel-2 satellite from ESA.

The necessity of developing automated image classification techniques is further supported by Cihlar et al. (2003) and Sester (2000) who emphasise the importance of knowledge base systems for automatic classifications, while Schiewe, Tufte & Ehlers (2001) emphasise that the automatic classification of remotely sensed data is an essential action within the process of generating or updating GIS databases. Cihlar et al. (2000) realise that a fine-scaled global mapping programme is unfeasible until all the major processes can be automated. The development of a research environment for advanced Landsat monitoring (REALM) at the University of Maryland on a cluster of Linux-based PC's demonstrates that hardware and software have finally become affordable enough to implement automatic processing (Masek, Shock & Goward 2001).

Many of the previous precincts such as spectral limitations (due to a lack of bands), inaccurate readings (due to low signal to noise ratio), data delivery delays, and policy problems have been overcome. It is consequently now the time to investigate the feasibility of automatic pre-processing and classification workflows, predicted years ago by Landgrebe (1997).

Automation can only be facilitated or made viable if a range of prerequisites are met. These entail that models used for each processing step in the production chain are rigid, with known error tolerances, and that no manual image interpretation is required at any step of the processing chain.

Processes need to be identified and investigated for their possible implementation in an automated processing chain. Cihlar et al. (2003) mention that the following processing actions need to be considered:

1. Sensor calibration;
2. Atmospheric correction;
3. Haze, clouds, and shadow identification;
4. Haze and shadow effects removal;
5. Regional radiometric mosaicking;
6. Pre-classification;
7. Labelling;
8. Confidence and accuracy assessment; and
9. Metadata.

Masek, Shock & Goward (2001):204 state that "new approaches for converting Landsat digital numbers into a standard radiometric reference frame (e.g. surface reflectance) need to be developed. Specific steps, including calibration, atmospheric correction, and terrain correction need to be improved to ensure that analysis across multiple scenes give constant results. Second, automated systems need to incorporate ancillary data (particularly field data) for validation and to improve classification accuracy."

1.4.4 Machine learning classifiers

One of the core technologies affecting the fourth industrial revolution is the advancement in artificial intelligence and machine learning techniques (Schwab 2016). Figure 1-3 illustrates the various types of algorithms available.

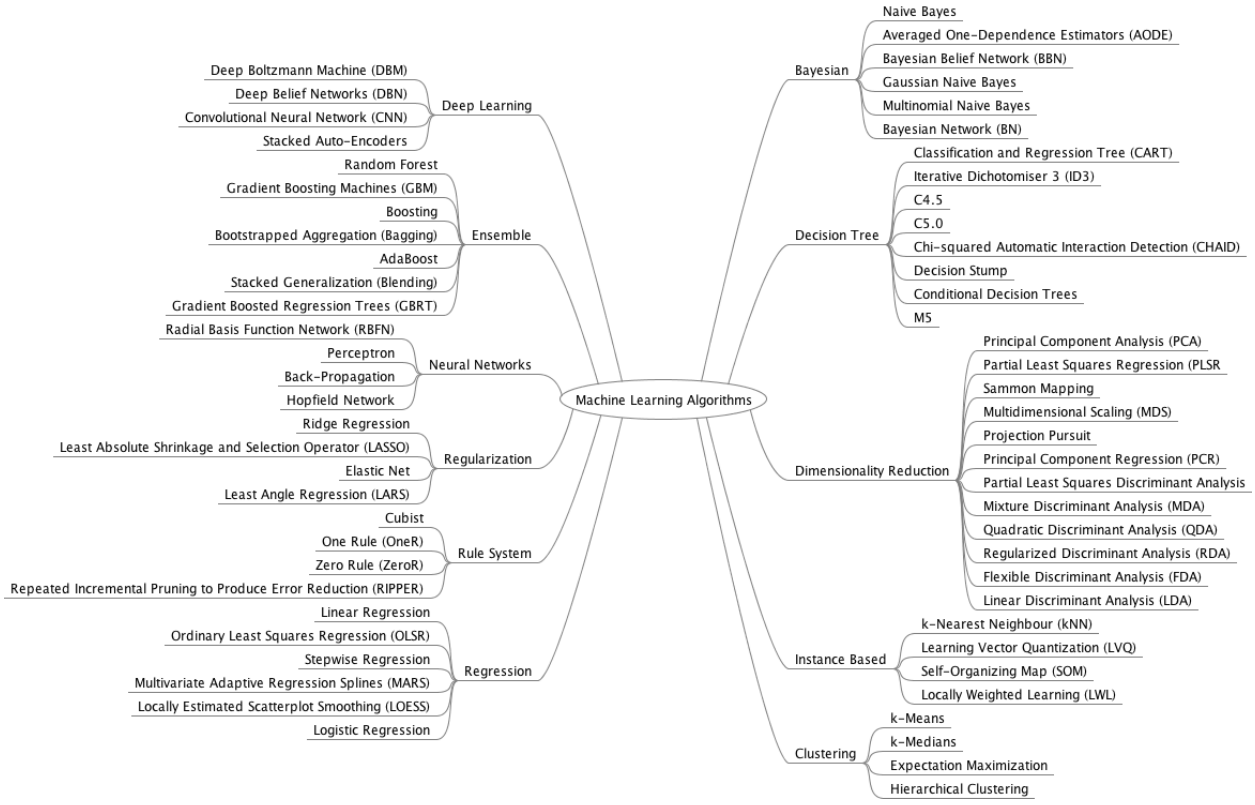

Brownlee (2017)

Figure 1-3 Types of machine learning algorithms

Machine learning can be formulated as Equation 1-4, whereby an output variable (y) is predicted by a function (f) in conjunction with an input variable (x).

$$y = fx \qquad \text{Equation 1-4}$$

where y is the output variable;

f is the function that best describes input variables; and

x is the input variable.

One can discriminate between parametric versus non-parametric machine learning algorithms. In a parametric model, the form for a function is selected beforehand, and the coefficients for the function are subsequently calculated from the data. Examples of parametric models are linear regression and logistic regression. In non-parametric machine learning, the function is learned. They are normally more computation intensive and require more data. Support vector machines (SVM) and neural network classifications (NNC), as well as decision tree classifiers such as random forests (RF) are good examples of non-parametric machine learning algorithms. Machine learning classification techniques generally have a trade-off between the reduction of bias, introduced by using simplified assumptions, and the reduction of variance, both of which

should be as small as possible for a good classification. Decision tree classifiers normally produce low bias values, whereas linear regression leads to high values. The following is a description of the most important machine learning algorithms, taken from Brownlee (2017):

Linear regression

Linear regression is expressed by correlating one set of variables with another set of variables, and is expressed by Equation 1-5. A coefficient of determination (R^2) is calculated together with a linear regression, and expresses how well the two variables can be described with a linear function.

$$y = gx + b \qquad \text{Equation 1-5}$$

Where y is the dependant variable;
x is the explanatory variable;
g is the gain or fractional relationship between the two variables; and
b is the bias between the two variables.

Logistic regression

Logistic regression uses a non-linear function to provide binary classifications of values 0 or 1, and can also provide the probability of a data instance belonging to either class. This method requires feature properties that are not highly correlated with one another and unrelated to the class.

Linear discriminant analysis

Linear discriminant analysis is a technique preferred to logistic regression, especially when dealing with more than two classes. For each input variable, the mean value per class and the variance calculated across all classes are required. This technique assumes that the data have a normal distribution and provides a probability for each class, ultimately allocating it to the class with the highest prediction value.

Classification and regression trees

Classification and regression trees (CART) are binary classifications splitting a group of classes into the most dissimilar sub-groups until ending at the individual class/leaf level. Each node/split uses a single input variable. Decision trees have a high variance and perform best in an ensemble.

Naïve Bayes algorithm

The Naïve Bayes algorithm calculates two types of probabilities from training data assumed to be normally distributed, namely the probability of each class and the conditional probability of each class given each *x* value.

K-nearest neighbour

In k-nearest neighbour, the entire training dataset is considered and the algorithm attempts to find the training sample with properties closest to that of the object being classified, where proximity is measured in Euclidean distance. This method utilises more computer memory and is computationally intensive as it needs to compare an observation with each individual training sample.

Learning vector quantisation

This algorithm uses neural networks to reduce the training sample and to include only the most relevant ones defining the classes before applying a k-nearest neighbour classification. This algorithm thus produces similar results to the previous, but is computationally more efficient.

Support vector machine (SVM)

SVM find boundaries between classes in feature space that are equal distances away in terms of class standard deviation. These boundaries are termed “hyperplanes” and can have non-linear multidimensional shapes to describe the boundaries between classes. Hyperplanes are mathematically described with support vectors that rely on clean samples, but are able to deal with a limited number of samples that do not need to be distributed equally among all classes.

Random forest (RF)

RF uses ensembles of decision tree classifiers, run across subsets of samples and variables. By applying bootstrap aggregation, or bagging, this classifier improves model performance because it reduces the variance without increasing the bias. Classifications from multiple trees are averaged, and a class is assigned to a sample with which it is associated most frequently. RFs require a larger amount of samples, distributed evenly across all classes.

AdaBoost

This is an ensemble technique that creates a strong classifier from several weak decision tree classifiers by creating several layers of models on top of each other, where each model attempts to describe the error of its parent. Models are added until the prediction is correct or a maximum number of layers have been produced. Very clean training data is needed for this approach.

Artificial and deep learning neural networks

Neural networks are computational models based on mathematics and threshold logic algorithms. They consist of several layers, iteratively analysing and defining relationships between variables of input data and output classes, using mathematical functions such as addition and subtraction. Neural networks have been rebranded over the decades as they became more complex and approximated the function of a human brain, with descriptors ranging from “neural networks” and “artificial neural networks” to “deep learning”. The classification process entails the definition and training of a neural network, after which it can be applied to data to classify it.

This section provided an overview of the remote sensing technologies applicable to forestry and summarised several product generation techniques. The next section formulates the research problem.

1.5 PROBLEM FORMULATION

The different geoinformation products required for the sustainable management of forests were discussed in Section 1.2. Currently, these satellite geoinformation products cannot always be generated at the speed, accuracy, and cost required from the forestry industry and government departments. With one cloud-free coverage per season, however, satellite observations from Landsat are often sufficient to serve a variety of geoinformation requirements for the forestry sector. These observations may consist of several partly cloudy scenes, and in the case of Landsat-7 imagery acquired after 31 May 2003, there may also be gaps in the imagery caused by the malfunction of the Scan Line Correction Mirror. In order to utilise this data, satellite images need to be radiometrically and geometrically normalised, and image composites without any cloud, shadow or missing data have to be created. The compositing of Landsat data is a relatively new application, and researchers concur that the techniques in this field should be refined (Roy, Ju & Kommadreddy 2011).

For continental, national or even regional operational applications, the extraction of geoinformation products using the methods described in Sections 1.4.1 and 1.4.2 is too labour intensive, and automated techniques such as those described in Section 1.4.3 are urgently needed. To date no operational forest monitoring service that addresses both the geoinformation requirements of governmental agencies and private industry exists for Southern Africa. The research question posed in this work is therefore:

How can existing, freely available remote sensing data be used to automatically generate geoinformation products required for forestry applications?

1.6 AIM AND OBJECTIVES

The aim of this research is to investigate the use of freely available remote sensing data to automatically generate geoinformation products that can be used by the forestry industry for planning and management. The objectives are to:

1. Develop and evaluate an image compositing technique that is completely automated, and that produces a product that is suitable for the extraction of geoinformation;
2. Develop automatic image classification techniques for providing thematic geoinformation required for forestry applications;
3. Compare the resulting classification techniques to existing rule-based and statistical classifiers; and
4. Identify remaining research gaps and make recommendations for future research.

The first hypothesis of this research is that the automation of radiometric and geometric corrections, with special reference to image compositing, is possible and leads to products that are superior to those generated by existing operational systems (such as WELD introduced in Chapter 2). Such composited data can then serve as an input for image classification, which relates to the second hypothesis, namely that the classification of imagery and the extraction of information relevant to forestry are not only possible, but economically viable and fast and can produce results of sufficient accuracy.

1.7 RESEARCH METHODOLOGY

This research is experimental in nature in that it compares the newly developed techniques with existing techniques, while also validating the resulting products with field (in situ) observations. The data used is quantitative in nature, consisting of physical radiation measurements at different wavelengths and temporal intervals. This primary data consists of direct measurements from the satellite optical sensors. The validation data was either collected during field visits or provided by forestry companies. The validation data and target classes are ordinal in nature.

Methods used in this research were based on physical and empirical models that could either be defended by the laws of physics or statistical patterns in the data. Statistical patterns or relationships could, in turn, be explained by various fields in the natural sciences. This work therefore relied entirely on the hard (physical) versus the soft (social) sciences.

The rest of the thesis is presented as two scientific articles. Manuscripts relating to these two articles were submitted to the *International Journal of Applied Earth Observation and Geoinformation*. The first manuscript (Chapter 2) was published in January 2016[1] and focusses on optimal pre-processing approaches and, in particular, image compositing methods for Landsat TM/ETM+ imagery. The article addresses the first research objective (see previous section). The second manuscript, unpublished, deals with the evaluation of machine learning classifiers trained by samples acquired within the study area compared to samples acquired outside the study area (applying signature extension). Furthermore, an optimised spectral rule-based classification (OSRBC) was developed and compared to existing rule-based classifications for the automatic classification of the preprocessed imagery and generation of forestry-related products.

While detailed descriptions of the experimental design were included in each manuscript, an overall experimental design and research agenda is provided in Figure 1-4. The research agenda outlines the research activities on the left and research outputs on the right. A study of the research requirements and the associated literature comprised the first step of the research, as was summarised in Section 1. Section 1.1 emphasised the global importance of forests and the sustainable use thereof, whereas Section 1.2 elaborated on the different geoinformation products required for sustainable management of forests. Section 1.3 focused on different remote sensing methods for deriving some of these geoinformation products. Following this preparatory work, the problem was formulated in Section 1.5, followed by the declaration of the aims and objectives in Section 1.6. The research methodology is provided in this section, while an overview of the experimental design is discussed in Section 1.8.

---

[1] http://dx.doi.org/10.1016/j.jag.2015.11.019

As this thesis consists of two articles, of which one (Chapter 2) has been published in a scientific journal. The conducted literature review is not a formal chapter on its own, as is normally the case with a thesis, but rather forms part of Chapters 1, 2, and 3.

Field work and data collection were carried out as part of the *Land Cover Field Guide* project allocated to the CSIR/Satellite Applications Centre (SAC), which was the responsibility of the author. Details of this common dataset are provided in Chapters 2 and 3, and will not be elaborated on here. The scene IDs of the 171 Landsat TM and ETM+ images used in this study are listed in Appendix I.

Research activities providing output for the compilation of the two articles consisted of the coding of image processing chains in the EASI scripting language of PCI Geomatica, registered by PCI Geomatics (2012), with which the data is subsequently processed, analysed, and evaluated. The work is ordered chronologically so that the paper on image classification follows the paper on image pre-processing and compositing.

The concluding research activities consist of a synthesis of research results in both of the articles. The findings from the two articles (Chapters 2 and 3) are also summarised, while a short synopsis of suggestions for future research and concluding remarks are provided in Chapter 4.

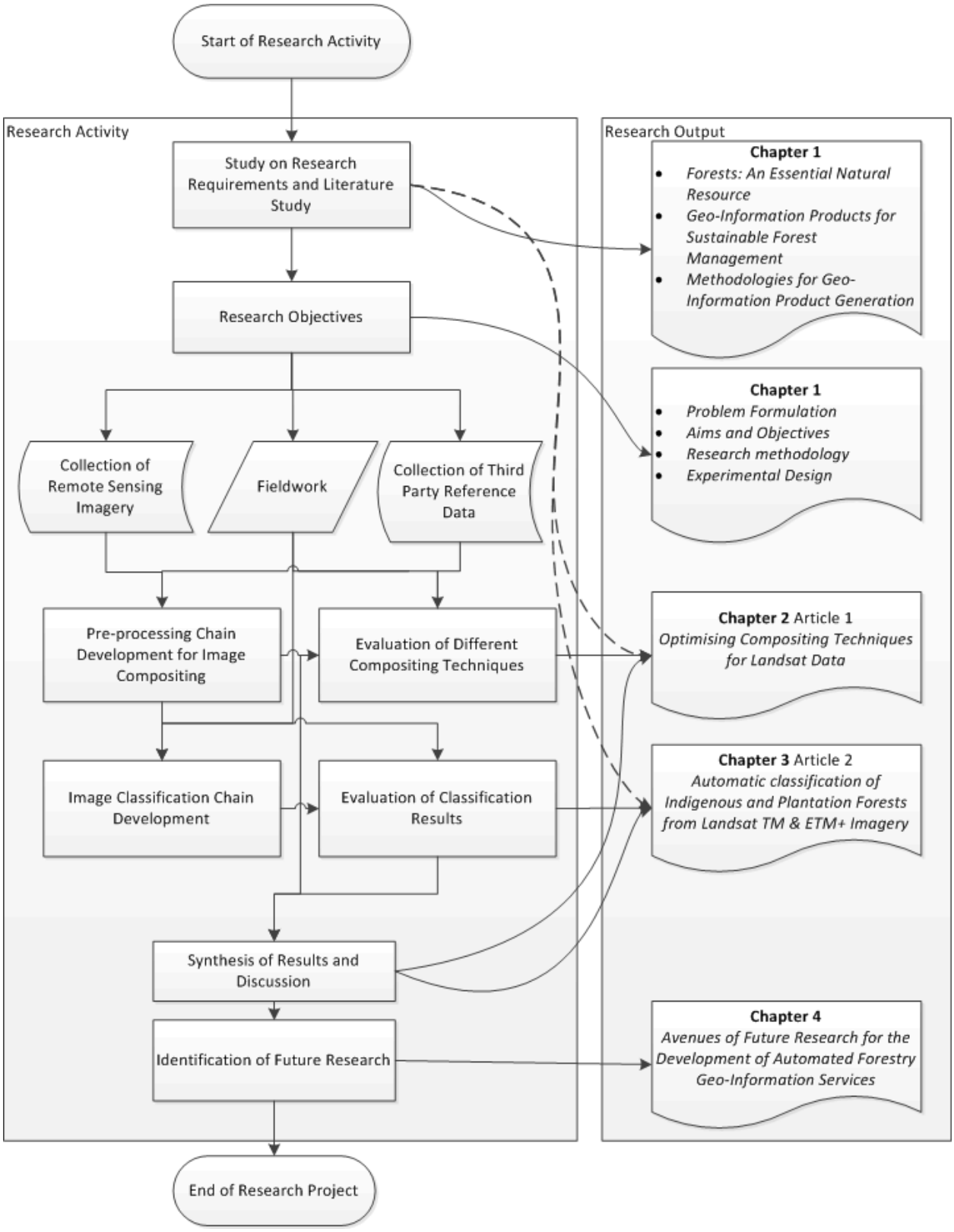

Figure 1-4 Research design and thesis structure

1.8 EXPERIMENTAL DESIGN

The overarching research aim of this thesis is to automatically generate basic geoinformation products for forestry applications from Landsat imagery. The reason for selecting Landsat imagery for this operational service can be motivated as follows:

- The information requirements can be met via (optimally) one cloud-free observation per season (not necessarily a single cloud-free scene) due to the relatively low vegetation dynamics of forests (compared to other agricultural thematic fields).
- The data is freely available from the USGS and several other ground receiving stations around the world. This means that it can provide a commercially viable operational service; a service that would have been too expensive if satellite imagery was commercially purchased.
- The data is well calibrated and include multispectral bands covering the full passive remote sensing spectrum – from blue to the thermal wavelengths. While the blue band is useful for the characterisation of atmospheric effects, the red, near-infrared, and shortwave infrared bands are suitable for the characterisation of different vegetation types, in particular forests.
- The imagery has a spatial resolution of 15–30 m, which is suitable for forestry applications where the monitoring of tree clusters is required.

For these reasons, this thesis focusses on the development of methods for the automatic information extraction of forestry geoinformation products from Landsat imagery in a South African context. Such methods could also be applicable to data from missions such as ESA's Copernicus Sentinel-2, and to a lesser extent RapidEye, Planet Scope, Resourcesat, and Spot, should the need arise for large-scale forestry products. Neither Sentinel-2 nor Landsat 8 imagery was considered for this study as the field work was conducted prior to the launch of either the above mentioned missions.

The next chapter describes the first set of methods developed within the context of this undertaking.

CHAPTER 2: EVALUATION OF A RULE-BASED COMPOSITING TECHNIQUE FOR LANDSAT-5 TM AND LANDSAT-7 ETM+ IMAGES[2]

2.1 ABSTRACT

Image compositing is a multi-objective optimisation process. Its goal is to produce a seamless cloud- and artefact-free artificial image. This is achieved by aggregating image observations, and by replacing poor and cloudy data with good observations from imagery acquired within the timeframe of interest. This compositing process aims to minimise the visual artefacts, which could result from different radiometric properties, or be caused by atmospheric conditions, phenologic patterns, and land cover changes. It has the following requirements: (1) Image compositing must be cloud-free, which requires the detection of clouds and shadows; and (2) the image composite must be seamless, minimising artefacts and visible across inter-image seams. This study proposes a new rule-based compositing technique (RBC) that combines the strengths of several existing methods. A quantitative and qualitative evaluation is made of the RBC technique by comparing it to the maximum NDVI (MaxNDVI), minimum red (MinRed), and maximum ratio (MaxRatio) compositing techniques. A total of 174 Landsat TM and ETM+ images, covering three study sites and three different timeframes for each site, are used in the evaluation. A new set of quantitative/ qualitative evaluation techniques for compositing quality measurement was developed, and showed that the RBC technique outperformed all other techniques, with MaxRatio performing the best and MinRed performing the worst.

Keywords:

image compositing, spectral rule-cased Classification, Landsat

[2] This chapter was originally published in the *International Journal of Applied Earth Observation and Geoinformation*, January 2016 (Volume 47, pages 1-14) [http://dx.doi.org/10.1016/j.jag.2015.11.019], but has been reformatted to conform to the guidelines of Department of Geography & Environmental Studies, Stellenbosch University.

2.2 INTRODUCTION

Image compositing is a popular technique used to reduce large datasets of satellite imagery, with often redundant or contaminated observations, into a single dataset of uncontaminated and "valid" data (Gutman, Ignatov & Olson 1994). The techniques are traditionally applied to low earth orbiting meteorological satellite imagery such as Advanced Very High Radiometer (AVHRR) and Moderate Resolution Imaging Spectroradiometer (MODIS) (Chuvieco et al. 2005), and have recently gained popularity in compositing higher resolution Landsat imagery, as the rich archive of historical imagery is of particular value for longitudinal studies and time series analyses (Roy et al. 2010). The compositing of Landsat Thematic Mapper (TM) and Enhanced Thematic Mapper Plus (ETM+) imagery in forest monitoring has recently gained popularity due to a good balance between image acquisition frequency and forest dynamics (Potapov, Turubanova & Hansen 2011). The use of Landsat ETM+ imagery with the scan line correction failure artefact (Roy et al. 2011) makes compositing highly desirable. Although there are a number of existing compositing techniques, there is no consensus on what the best techniques are for Landsat TM and ETM+ imagery (Dennison, Roberts & Peterson 2007). Many of the existing techniques were developed for other sensors or have specific limitations that reduce the quality of the resulting products.

A common technique for image compositing is to use observations from an image which has the highest normalised difference vegetation index (NDVI) value of all the images in the stack (Gutman, Ignatov & Olson 1994). The assumption is that observations with a higher component of haze or cloud will have a higher response in the red band and thus a lower NDVI value. This compositing method, commonly referred to as maximum value compositing (MVC), is widely used and was initially developed for AVHRR and MODIS data (Van Leeuwen, Huete & Laing 1999). MVC is applied (Roy 2011; Roy et al. 2011) to web-enabled Landsat data (WELD), while Roy et al. (2010) used a combination of MVC, based on NDVI and brightness temperature, to generate Landsat composites after preliminary cloud and cloud shadow masking. This technique is, henceforth, referred to as the maximum NDVI compositing or MaxNDVI.

Although MaxNDVI is known to be ineffective at excluding haze, shadow, and bidirectional reflectance distribution function (BRDF) artefacts, it is very useful for the generation of a single band NDVI product as implemented by Maxwell & Sylvester (2012) and Kross et al. (2011) who used it to monitor the greening phenology in the boreal forests of Canada (using AVHRR data). To overcome some of the shortcomings of using MaxNDVI to create multiband composites, Brems, Lissens & Veroustraete (2000) and Maxwell & Sylvester (2012) used a median value of

several spectral observations on imagery corrected to at surface (AS) reflectance with the MC-FUME method. The main drawback of this method is that it relies on AS reflectance imagery.

Hüttich et al. (2011) used a combination of maximum NDVI and the mean value of several cloud-free observations in their compositing for MODIS time-series data, producing monthly composites for a land cover classification in Namibia. Pouliot et al. (2011) found that a 6–8 day MaxNDVI for AVHRR or medium resolution imaging spectrometer (MERIS) data is optimal, while 10–14 day averaged composites are suitable for the detection of green-up periods in Canada. Breaker, Armstrong & Endris (2010) established an objective basis for finding the correct compositing timeframe, characterised by the phonological response, without losing too much temporal information. They concluded that, when images were taken daily along the coast of California, the best compositing window was 3.2 days. A blending approach that weighs acquisitions according to their quality was used to produce composites.

Luo, Trishchenko & Khlopenkov (2008) developed a technique for generating 250 m resolution, seven band, clear-sky composites of MODIS imagery of Canada using sun-satellite relative azimuth angles. This was conducted after a good pre-classification. Unfortunately, hemispheric directional specific compositing techniques are not suitable for lower latitudes or for use with the nadir-acquired narrow swath width data produced by Landsat. Hemispheric directional compositing relies on considerable image overlaps and various acquisition angles. The comparison of different compositing techniques, however, showed that the maximum ratio compositing technique (MaxRatio) [max(B4,B5)/B1] is a promising alternative to MaxNDVI, mainly because the latter performs poorly over water bodies as it gives preference to cloudy observations in such areas. The MaxRatio class-based compositing has inspired this work.

A computationally-intensive compositing technique developed by Dennison, Roberts & Peterson (2007) uses the shape of the signature across the full spectral range of the input imagery to guide decision making about whether to include or reject an observation in a composite. This approach is promising, but its computational requirements limit its application to operational solutions.

All of the methods described above substitute missing values in a composite and do not adjust the spectral values of valid picture elements, with the exception of the work done by Hüttich et al. (2011) which entailed a hybrid approach of averaging and substitution. Adjustments can produce a result that is visually more appealing, as demonstrated by the GLS 2005 gap-filled ETM+ imagery (Gutman et al. 2008). This approach uses a simple histogram matching of the master image (composite) needing substitution and the slave image to identify apparently invariant features. However, it has been shown that invariant features cannot be identified accurately enough by this technique. An alternative method is to match Landsat imagery to spot

vegetation data (Olthof et al. 2005), but the added complexity and instability of such approaches suggest that cosmetic adjustments of spectral values should be avoided, especially when using Landsat-7 ETM+ scan line correction off (SLC OFF) data.

Chuvieco et al. (2005) used the maximum values in the thermal band to optimise compositing of MODIS imagery for burnt area mapping. Earlier work on burnt area mapping by Barbosa, Pereira & Grégoire (1998) used MaxNDVI techniques on AVHRR albedo corrected data. This approach is expected to provide unreliable results for Landsat composites and forestry applications as forests are normally cooler than their surroundings and because the resolution of the thermal bands for both ETM+ (60 m) and TM (120 m) is significantly coarser than that of the multispectral bands (30 m). In addition, the poor relative calibration of the thermal detectors in the TM sensor is expected to introduce noise.

Image compositing techniques generated from wide swath data have to take into account large spectral distortions introduced by BRDF (Hu et al. 2000). Up to ten cloud-free observations, acquired for MODIS and Spot VEGETATION at different angles, are needed to accurately fit a BRDF function to each pixel. These functions are then applied to the observations candidates in the compositing window, and often averaged for the composite (Cihlar et al. 2004; Hagolle, et al. 2005). These compositing methods cannot be applied to Landsat data due to insufficient angular observations, and a relatively low angular variability.

Maximum surface temperature compositing, as described by Liang, Li & Wang (2012), is known to produce good results by favouring the warmest observations for a composite. It was not considered in this study for the same reasons mentioned above for not using the method proposed by Chuvieco et al. (2005). With the overall objective of excluding haze, cloud, and cloud shadow pixels, the haze optimised transformation (HOT) developed by Zhang, Guindon & Cihlar (2002) can provide a valuable contribution to the exclusion of such observations from composites. HOT is discussed in more detail in Section 2.3.3.2.

This paper proposes a new RBC technique that combines several existing pre-processing, pre-classification, and compositing methods. The RBC technique is evaluated by a quantitative and qualitative comparison thereof to three existing compositing techniques, namely the maximum NDVI (MaxNDVI), minimum red (MinRed), and maximum ratio (MaxRatio) methods using 174 Landsat TM and ETM+ images. To assess the transferability and robustness of the techniques for forestry applications, images from three sites and three different timeframes were chosen. The results of the evaluations are discussed in the context of finding an operational solution and recommendations are made for future research opportunities.

2.3 MATERIALS

2.3.1 Study areas

To demonstrate the transferability of the developed techniques, three study sites in different regions in South Africa were selected. The selection of test sites was based on the heterogeneity of the landscape and land cover classes and included bright bare areas, strong topographic relief areas, highly vegetated areas (e.g. forestry, sugarcane, dry-land, and irrigated cultivation) as well as large urban areas. All three study sites are characterised by seasonal cloud cover and dry periods with smoke contamination from burning biomass, which poses major challenges for compositing (Dennison, Roberts & Peterson 2007). Each site covers a one degree square area and represents a different climatic zone (Figure 2-1). Variations of elevation above sea level within each area were recorded from the Shuttle Radar Topography Mission (SRTM) digital elevation model (DEM). The three sites are defined as:

Site A (2430 Lowveld) extends from 30.5–31.5° E and 24.5–25.5°S, and covers a large block of commercial forestry in South Africa. The area has a very distinct subtropical climate and summer rainy season, although rainfall is heavily influenced by the orographic effect of the escarpment (elevation ranges from 283 m to 2255 m above mean sea level), which runs from north to south. The north-western parts of the study area falls in the rain shadow of the escarpment, resulting in semi-arid conditions. The eastern section of the study area is dominated by human land use activities which are spectrally characterised by high albedo. Veld and forest fires frequently occur in winter which, added to the natural vegetation's strong spectral response to phenologic changes over time, makes image compositing difficult.

Site B (3318 Western Cape) extends from 18.25–19.25° E and 33.25–34.25° S and includes parts of the Cape Town metropolitan area, as well as the towns of Stellenbosch, Paarl, and Grabouw. The area has a Mediterranean climate with most rainfall occurring during the winter months (May to August). Elevation ranges from 0 m to 1959 m above mean sea level, with cloud cover being a regular feature in the mountainous areas. A wide range of land cover classes are present in the area and includes heathland (fynbos), forestry plantations, small patches of indigenous forests in steep valley gorges, vineyards, large agricultural fields (mainly for wheat production), fruit orchards, large sealed surfaces, and water.

Site C (2930 Natal Midlands) is situated in the Natal Midlands in the Kwa-Zulu Natal province and extends from 30–31° E and 28.75–29.75° S. The south and south-east fringes of the study area intersect the cities of Pietermaritzburg and Durban respectively. The landscape is dominated by steep escarpment slopes and rolling hills, with elevation ranging from 44 m to 1761 m above

mean sea level. The overall rainfall is high (600–1000 mm/a), with the exception of the dryer north-eastern corner of the site (500 mm/a). Most precipitation occurs in spring, summer, and autumn months. Smoke from fires perturbs the atmosphere during dry winter months, while fog is often present during springtime. Fog also occurs frequently in the mornings throughout the year, which poses a unique challenge as this is the time when Landsat images are acquired. Forestry, sugarcane, and dry-land cultivation are the major commercial land uses in the area, although subsistence agriculture and traditional dwelling structures are also present.

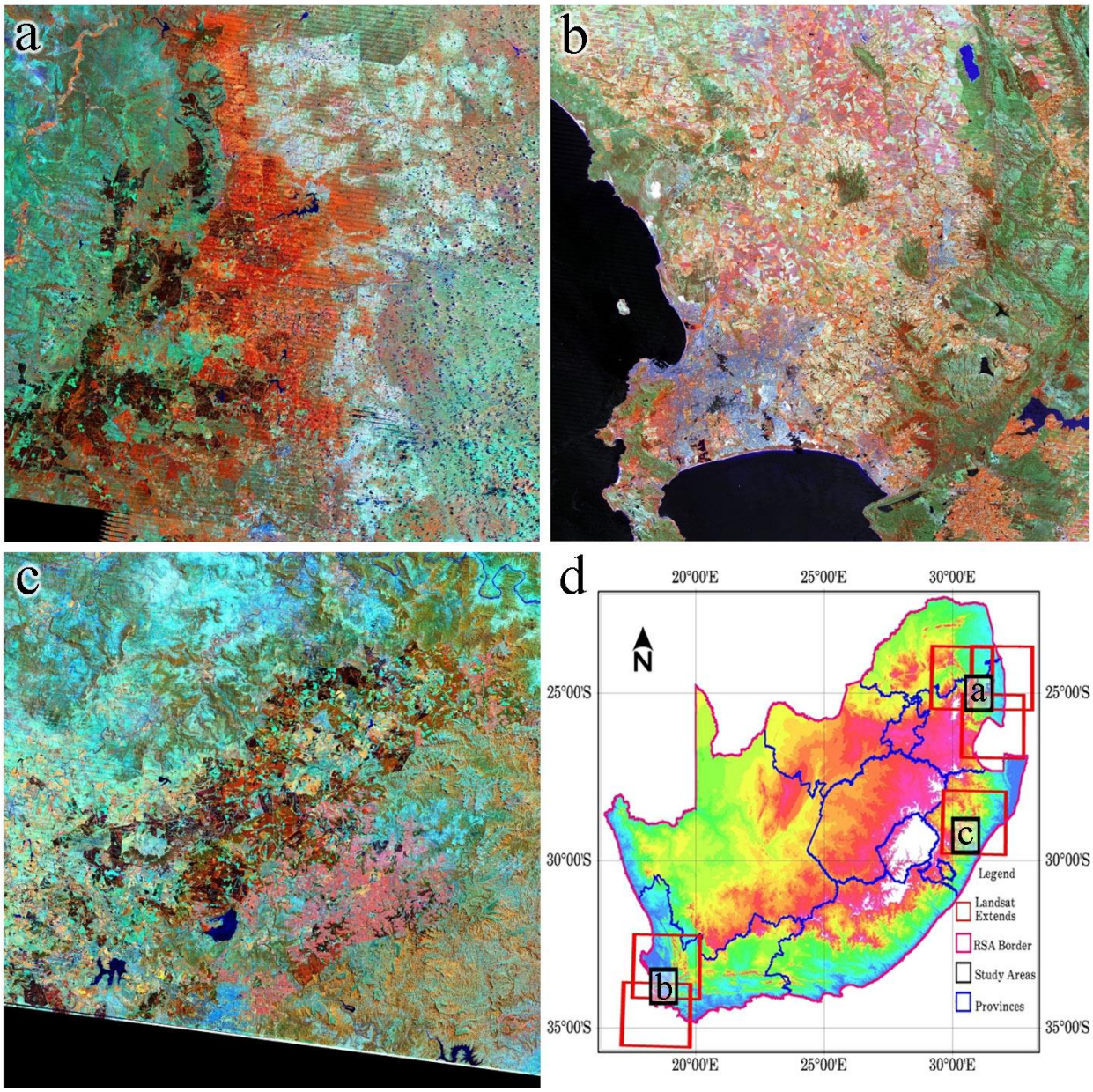

Figure 2-1 Location of study sites used to evaluate image compositing techniques: (a) Site A: 2430 Lowveld, (b) Site B: 3318 Western Cape, (c) Site C: 2930 Natal Midlands, and (d) location of study sites in South Africa with reference to Landsat scene extents and underlying topographic variability (image composites are calibrated Landsat ETM+ false colour images displayed in an adaptively stretched RGB band combination of 453).

2.3.2 Imagery

A total of 174 Landsat scenes were selected, ordered and downloaded through the United States Geological Survey (USGS) Global Visualization Viewer (GLOVIS) catalogue. These scenes were from the period between 2008 and 2010, covered the study sites, and had cloud cover of below 50%. The imagery was processed to Level 1T by the USGS using the Landsat Product Generation System (LPGS) processing software. The 5 m resolution Stellenbosch University DEM (SUDEM), which was generated by the Centre for Geographical Analysis (CGA) at Stellenbosch University from 5 m contours and SRTM data, was used for the topographic normalisation of the imagery.

2.3.3 Rule-based compositing (RBC)

The introduction provided an overview of existing compositing techniques. The following subsections discuss the theoretical and technical aspects considered for developing the RBC method.

2.3.3.1 Radiation measurements and L1T product generation

The charged coupled devices (CCDs) on both Landsat 5 TM and Landsat-7 ETM+ are sensitive to electromagnetic radiation, recorded as voltage over a certain integration time (Irish 2012). During image acquisition, these detector readings are digitised to relative voltage in an 8-bit data stream and transmitted to ground receiving stations. Using calibration parameters for each CCD element, measurements are converted from relative voltage to relative radiance during Level 1R processing. During Level 1T processing, the internal and external orientation parameters of the sensor are calculated and refined with ground control points (GCPs) from a chip database using the LPGS software that runs at a satellite ground receiving station. Parameters such as scanning speed, sensor orientation, angular velocity, and the optical path model, together with a DEM, are applied to the imagery to account for geometric distortions (such as topography-induced parallax), which results in an orthorectified Level 1T product. The importance of using orthorectified products versus Level 1G products for compositing has been demonstrated on AVHRR data. Fontana et al. (2009) showed that, irrespective of the coarse resolution of AVHRR, parallax is noticeable in the non-rectified product, leading to significant artefacts during compositing.

All imagery used in this study was resampled to a standard grid using a cubic convolution resampling algorithm approximating the sensor-specific modulated transfer function (MTF) resampling kernel during Level 1T production. The importance of this standard grid for compositing was highlighted by Tan et al. (2006). The same grid positions were used during

image tiling and prior to compositing to avoid a second resampling process. The Landsat TM and ETM+ imagery used in this study has seven spectral bands that represent specific parts of the electromagnetic spectrum. Their common names are denoted in Table 2.1 and will henceforth be used.

Table 2-1 Landsat TM and ETM+ spectral bands, common names and wavelength ranges

Band	Common Name	Wavelength
1	Blue	0.45 µm–0.52 µm
2	Green	0.52 µm–0.60 µm
3	Red	0.63 µm–0.69 µm
4	NIR	0.76 µm–0.90 µm
5	SWIR 1.6	1.55 µm–1.75 µm
6	Thermal	10.40 µm–12.50 µm
7	SWIR 2.1	2.08 µm–2.35 µm

Adjusted from Irish (2012)

Radiometric normalisation is required for many quantitative image analysis techniques, and for extracting indices and features suitable for seamless image compositing. This is done by converting the digital numbers (DN) values of the Level 1T product (which represent relative radiance) to at-sensor radiance (L_λ) values using gain and bias coefficients provided in the header files of the imagery, as set out in Equation 2-1:

$$L_\lambda = DN * gain + bias$$ Equation 2-1

where L_λ is the radiance in W m-2sr-1µm-1;

DN is the digital number;

gain is the gradient of the slope in W m-2sr-1µm-1; and

bias is the corresponding radiance at a DN value of 0 in W m-2sr-1µm-1.

At-sensor radiance values reflected from surfaces vary according to the degree of intensity of solar irradiance the surfaces were subjected to; therefore, a further normalisation is required. During this normalisation, the solar elevation angle, spherical reflectance, earth-sun distance, and expected solar irradiance at an average earth-sun distance are taken into account. This normalised value is called top of atmosphere (TOA) reflectance, which is the ratio between the expected full reflection of radiation from Lambertian surfaces, to the measured radiation. The formula for converting at-sensor radiance to reflectance is:

$$\rho = \frac{\pi L d^2}{E_s \cos \theta_s}$$ Equation 2-2

Where ρ is the reflectance;

π is the scattering from a spherical surface;

L is the measured radiance by the sensor in W $m^{-2}sr^{-1}\mu m^{-1}$;

d	is the distance between the earth and the sun measured in astronomical units;
Es	is the exoatmospheric solar irradiance at a distance of one astronomical unit between the earth and the sun for a given wavelengths; and
θs	is the solar zenith angle.

The distance between the earth and the sun (*d*) can be approximated by (Mather 2004):

$$d = 1 - 0.01674\cos\left(0.9856(JD - 4)\right)$$ Equation 2-3

where

d	is the distance between the earth and the sun measured in astronomical units; and
JD	is the Julian day interpreted as day of the year starting with the 1 January and ending with 31 December.

A distinction between TOA reflectance and AS reflectance is made because the latter further compensates for the atmospheric effect (scattering and absorption) on reflected radiation (Richter 2011b). For the purpose of this study, only TOA reflectance is used, because operational atmospheric correction is poorly understood and its automated application to South African atmospheric conditions predating the acquisition of MODIS imagery is unreliable (Ju et al. 2012).

Due to the relative data scarcity of TM and ETM+ imagery of Southern Africa (Roy et al. 2010) and comparable radiometric properties between these datasets, imagery from both sensors were used interchangeably for compositing purposes. This is a common practice in the MODIS community as attested by the MODIS Combined Product (MCD) range and has also been applied to Spot VEGETATION data (Hagolle et al. 2005).

2.3.3.2 Spectral characterisation of surfaces

Each surface type is characterised by distinct spectral characteristics and spectral band reflectance measurements. Clouds have a high reflectance in all spectral bands which often leads to a saturated signal, with the exception of the thermal band which generally provides lower values over clouds compared to the surrounding land masses (Chuvieco et al. 2005). Due to selective scattering of water vapour, shorter wavelengths show stronger scattering of radiation over cloudy and hazy areas (Richter 2011b). The high correlation between the blue and red band over most land cover types (with the exception of water and certain urban structures with a proportionally higher reflectance in the blue band) means that a clear-sky vector can be calculated by using these bands. Any deviation from this clear-sky vector can be attributed to

haze and cloud and is characterised by a haze vector perpendicular to the clear-sky vector (Zhang, Guindon & Cihlar 2002). This so-called HOT can be calculated by:

$$HOT = \rho_{BLUE} \sin\theta - \rho_{RED} \cos\theta \qquad \text{Equation 2-4}$$

Where HOT is the haze optimised transformation;

ρ_{BLUE} is the reflectance of the blue band;

θ is the angle of the clear-sky vector; and

ρ_{RED} is the reflectance of the red band.

By favouring low values over higher values, HOT can be used for compositing. The HOT variable is, however, very noisy at lower values and should therefore only be used at higher intensities (Richter 2011b). As all imagery is in TOA reflectance, a value of 1.3 derived experimentally for θ could be used throughout the dataset, thereby avoiding a manual calculation thereof.

The effectiveness of this technique is illustrated in Figure 2-2, which depicts the result of HOT on a Landsat 5 TM image acquired on 28 May 2009. The smoke plumes from an active fire to Figure 2-2a the west of the big dam and the thin fog patches in the eastern centre are clearly visible in a. From Figure 2-2b it is clear that this transformation is not only very useful for masking clouds, but also very effective in enhancing and delineating haze, smoke plumes, and fog.

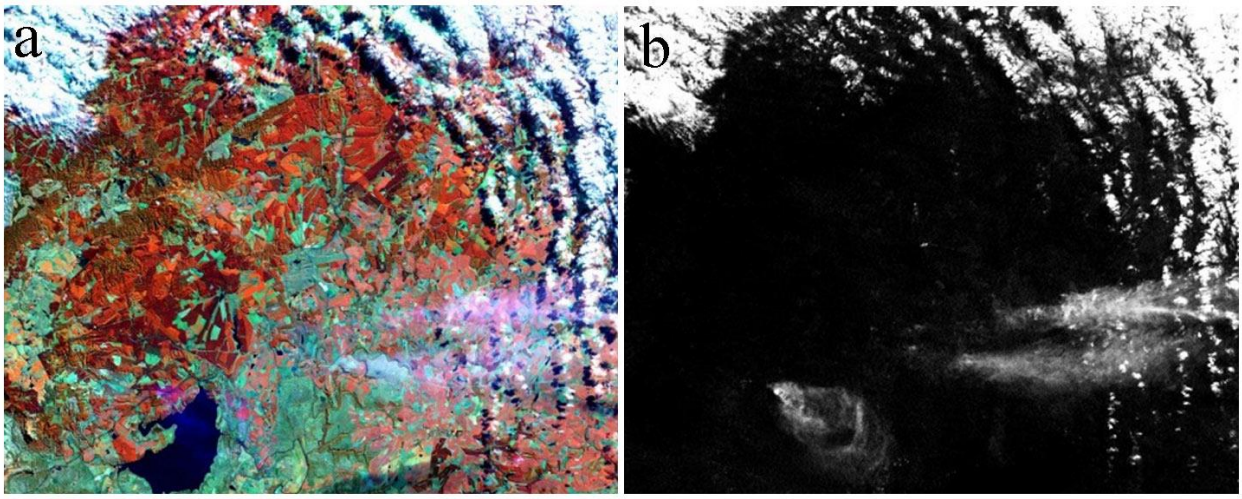

Figure 2-2 (a) 453 false colour composite, and (b) HOT for a Landsat 5 TM image acquired on 28 May 2009 over the Natal Midlands

A tasselled cap transformation (Kauth & Thomas 1976) was used to transform the spectral information into thematic principal components with predefined eigen vectors. The tasselled cap

parameters used for Landsat-7 reflectance data (Huang et al. 2002) are listed in Table 2-2. This technique uses a linear transformation to condense information captured in the spectral bands, so that the first three components represent brightness as tasselled cap component 1 (TC1), greenness (TC2), and wetness (TC3) features. Combined, these features account for over 97% of the image variability (Huang et al. 2002). Shadow has a proportionally higher value in the wetness component, while the inverse is true in the greenness and brightness features. TC1 was consequently used to identify and discriminate between shadow pixels during the compositing process and both TC1 and TC3 were used in the compositing performance tests.

Table 2-2 Tasselled cap parameters for Landsat TM and ETM+ reflectance values

Index	Blue	Green	Red	NIR	SWIR 1.6	SWIR 2.1
TC1	0.3561	0.3972	0.3904	0.6966	0.2286	0.1596
TC2	-0.3344	-0.3544	-0.4556	0.6966	-0.0242	-0.263
TC3	0.2626	0.2141	0.0926	0.0656	-0.7629	-0.5388

Two additional indices, namely NDVI and the aerosol free vegetation index (AFRI), were used to classify thematic content from the Landsat imagery. NDVI is the most widely used vegetation index used for discriminating between actively growing vegetation and areas with no vegetation.

AFRI, as described by Karnieli et al. (2001: 10), is based on the high correlation between ρ_{RED} and $\rho_{SWIR2.1}$, and the observation that the latter is much less affected by Mie or Rayleigh scattering. The AFRI is consequently more suitable where these conditions are prominent. AFRI is defined as:

$$AFRI_{2.1} = \frac{(\rho_{NIR} - 0.5\rho_{SWIR2.1})}{(\rho_{NIR} + 0.5\rho_{SWIR2.1})}$$ Equation 2-5

Where $AFRI_{2.1}$ is the aerosol free vegetation index using SWIR 2.1;

ρ_{NIR} is the reflectance of the blue band; and

$\rho_{SWIR2.1}$ is the reflectance of the SWIR 2.1 band.

2.3.3.3 BRDF effects and topography-induced radiometric distortions

Some surfaces have anisotropic reflectance properties (i.e. light is reflected at different intensities and into different directions, depending on the illumination angle). This phenomenon is characterised by the BRDF, and is particularly pronounced over forests where values are lower for pixels acquired east and higher for pixels acquired west of the satellite ground track respectively for a Landsat image acquired in the morning. Image composites derived from images acquired along adjoining satellite tracks will consequently be most affected by this phenomenon. Correction techniques for Landsat imagery have been suggested by Shuai et al. (2011), but they require multi-angular observations from imagery such as MODIS or the multi-

angle imaging spectroradiometer (MISR), acquired at coarser resolutions. As more work is required on the operational fusion of MODIS and Landsat data before these techniques can be incorporated into operational workflows for Landsat imagery, they were consequently not considered in this study. Another approach proposed by Potapov et al. (2012) is to simply adjust each pixel value according to its column number obtained from its relative position to the central column. This technique is applied irrespective of surface cover type and as such only addresses variation in forest cover types, to the detriment of all other classes. The technique particularly distorts spectral responses from water, because water has an inverse BRDF compared to vegetation (Danaher, Xiaoliang & Campbell 2001). This approach is not desirable for objective compositing and was consequently not considered for this study. The method suggested by Xiaoliang et al. (2001) was also not considered because it entails the use of the same BRDF coefficients for all land cover types and does not take into account variable atmospheric conditions across the mosaic. The solar elevation and azimuth of images of an area acquired at different times in a year varies considerably, particularly in areas with strong topographic relief. It is therefore advisable to perform a radiometric topographic normalisation (also referred to as an illumination correction) before image compositing as this compensates for reflectance values of the same spectral land cover types on shady and sunny slopes. Numerous topographic correction techniques have been proposed. These can be grouped into two approaches: 1) those assuming a Lambertian reflectance from surfaces, of which the Cosine or Lambertian correction is the most popular (Richter, Kellenberger & Kaufmann 2009); and 2) those assuming anisotropic reflection and depend on different surface cover types. The second group provides the best results (McDonald et al. 2001), but requires an accurate pre-classification and calculation of anisotropic parameters for each spectral band and class (Baraldi, Gironda & Simonetti 2010). The most common anisotropic corrections are the C and Minnaert correction methods. McDonald et al. (2001) compared various techniques and found that the Minnaert and C corrections performed the best. Although they did not account for different land cover classes, they noted that it is important to account for these classes in order to achieve accurate results. For the purpose of this study, the Minnaert correction was used, formulated as:

$$L_H = L_T \left[\frac{\cos(sz)}{\cos(i)}\right]^k$$ Equation 2-6

Where L_H is the radiance normalised to the horizontal;

L_T is the radiance measured by the sensor;

sz is the solar zenith angle;

i is the local incidence angle; and

k is the Minnaert constant.

The Minnaert constant can be regressed with:

$$\log(L_T \cos(sz)) = \log(L_H) + k \log(\cos(i) \cos(e)) \quad \text{Equation 2-7}$$

Where L_H is the radiance normalised to the horizontal;

L_T is the radiance measured by the sensor;

sz is the solar zenith angle;

i is the local incidence angle;

k is the Minnaert constant; and

e is the existence angle equal to the surface slope angle when sensor at nadir.

The C correction is described by:

$$L_H = L_T \left[\frac{\cos(sz) + c}{\cos(i) + c}\right] \quad \text{Equation 2-8}$$

Where L_H is the radiance normalised to the horizontal;

L_T is the radiance measured by the sensor;

sz is the solar zenith angle;

i is the local incidence angle; and

c is the c correction factor.

where c is expressed as

$$c = \frac{b}{m} \quad \text{Equation 2-9}$$

Where c is the C correction factor;

b is the intercept regressing radiance against incidence angle; and

m is the gradient regressing radiance against incidence angle.

The incidence angle *i* can be calculated by (Liang 2004 and Mather 2004):

$$\cos(i) = \cos(\theta_s)\cos(\beta_t) + \sin(\theta_s)\sin(\beta_t)\cos(\varphi_s - \varphi_t) \quad \text{Equation 2-10}$$

where i is the local incidence angle;

θ_s is the solar zenith angle;

β_t is the slope angle;

φ_s is the solar azimuth angle;

φ_t is the slope azimuth angle.

2.3.3.4 Image pre-classification

Image pre-classification is required for various pre-processing steps (e.g. topographic normalisation) before compositing can take place. A spectral pre-classification (as proposed by Baraldi et al. (2006) for Landsat and Baraldi et al. (2010a, 2010b, 2010c) for multiple sensors), makes use of unique spectral responses of various land cover types, separating these in a rule-based classification. This pre-classification allows for a class-based compositing favouring vegetation classes, which is the main focus of many studies. These spectral pre-classifications can also be used to guide the compositing approaches. Luo, Trishchenko & Khlopenkov (2008) used a simple rule base (as illustrated in Figure 2-3) to discriminate between non-vegetated lands, snow/ice, water bodies, clouds, cloud shadows, and vegetated lands. Only observations in relevant classes for the compositing process were used. This approach was also used in this study.

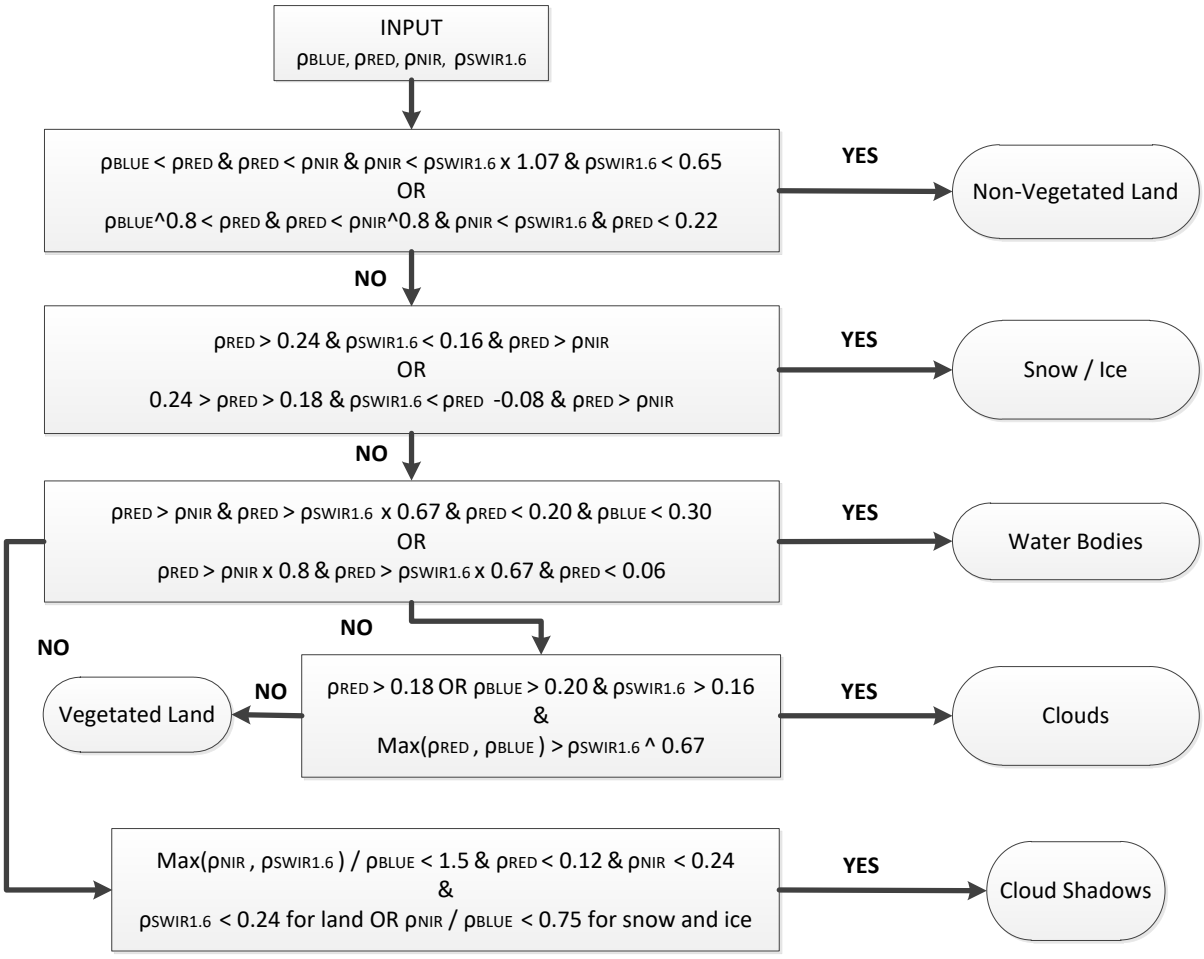

Adapted from Luo, Trishchenko & Khlopenkov (2008)

Figure 2-3 Classification rule base

2.3.3.5 Image compositing

RBC is essentially a fusion of existing compositing techniques, with the addition of an automated pre-classification of spectral classes. The RBC compositing rules are shown in Figure 2-4. In essence the compositing processor starts with a single scene in close temporal proximity to the reference data and places it, along with its pre-classification and calculated features (such as the HOT and NDVI and TC1), into the composite file. It then takes the next image closest in time and considers it's pixels as candidates for substitution of the existing pixels in the composite. A substitution takes place if the candidate pixel has valid data (i.e. it has a value which is not saturated or cloudy) and the existing composite pixel is cloudy or has no data. When the existing composite pixel represents a burnt area, and the candidate pixel is valid or cloudy, MaxRatio compositing is applied.

When both composite and candidate pixels are cloudy, or both are not cloudy, then the following decisions (based on features calculated from TOA reflectance values scaled by 10000) are made:

1. If the HOT value of either composite or candidate is above 1000, MIN HOT compositing is applied;
2. Else, if the tasselled cap TC1 is less than 1500, then MaxRatio compositing is applied; or
3. Else, MaxNDVI compositing is applied.

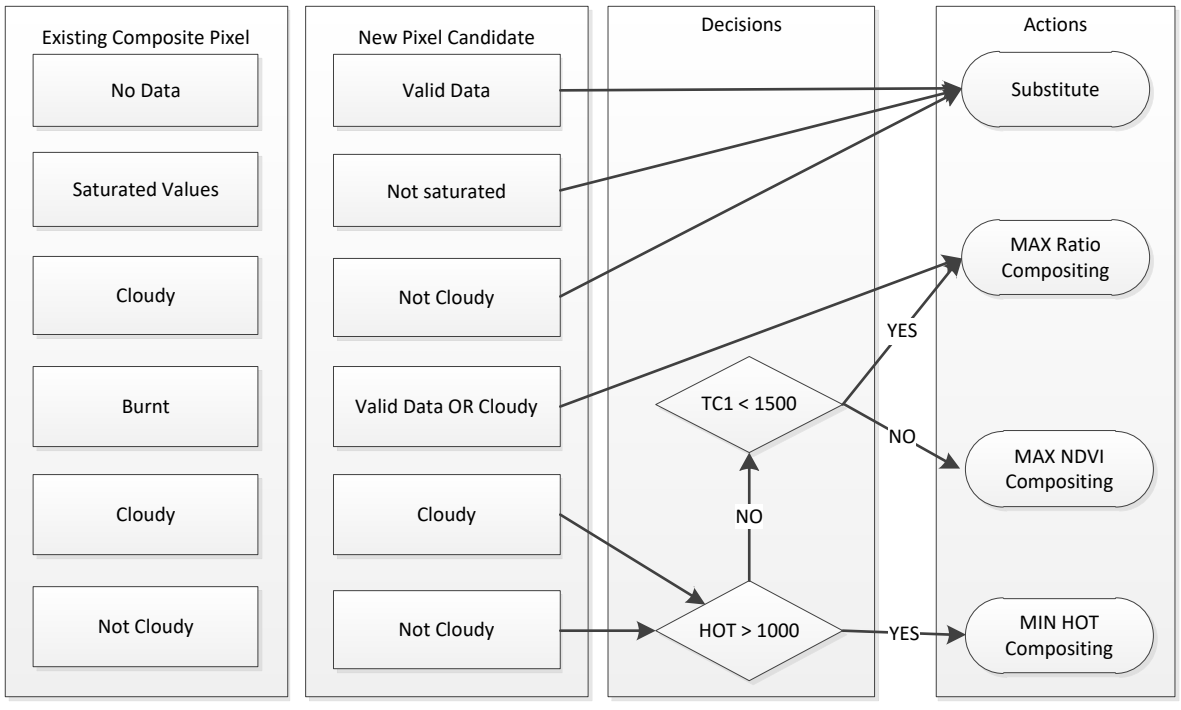

Figure 2-4 RBC flowchart showing composite and input image conditions, decisions and actions for value substitution

2.3.4 Experimental design

The experimental design is shown in Figure 2-5. The Level 1T Landsat imagery was ingested into a workflow management framework, called Image Resource Management Information System (IRMI), which is designed around libraries and functions provided by PCI Geomatica 2012 software. During this ingestion, all metadata required for further radiometric and geometric image processing was harvested from accompanying header files of the respective imagery. All image manipulation and processing were handled by automated processing chains as part of the IRMI system and was scripted in the EASI modelling language of PCI Geomatica 2012. The images were subsequently clipped to the extents of the study areas, converted to TOA reflectance, multiplied by 10000, and stored as scaled, signed 16bit files. A spectral rule-based classification (SRC) (Baraldi et al. 2006) was used to classify the image into classes with different BRDF properties (which excluded clouds and water), which were then used to calculate the Minnaert coefficient for topographic normalisation as proposed by Baraldi, Gironda & Simonetti (2010).

Coefficients published by Huang et al. (2002), NDVI values, and an HOT (Zhang, Guindon & Cihlar 2002) were used to calculate a tasselled cap transformation for the imagery. Sample vector polygons were used to extract pixel values from all spectral bands and derived indices. These values were further analysed in the R statistical package to evaluate the suitability of feature layers for image compositing. Focus was placed on the ability to discriminate between clouds, haze, smoke, shadow, vegetation, and other spectral land cover classes – the aim being the elimination of clouds, haze, smoke, and shadow in the final composite and the favouring of vegetated observations.

Four image composites with different timeframes were generated per study site and for each composite technique. These techniques were:

- MaxNDVI, as used in WELD (Roy 2011);
- MinRed (Liang, Li & Wang 2012);
- MaxRatio, or [max(B4,B5)/B1] (Luo, Trishchenko & Khlopenkov 2008); and
- RBC, a new parametric model incorporating NDVI, HOT, the first tasselled cap parameter (brightness), and a spectral rule-based pre-classification.

For all four compositing techniques, a cloud mask, generated from the SRC, was used to eliminate clouds from the composite products.

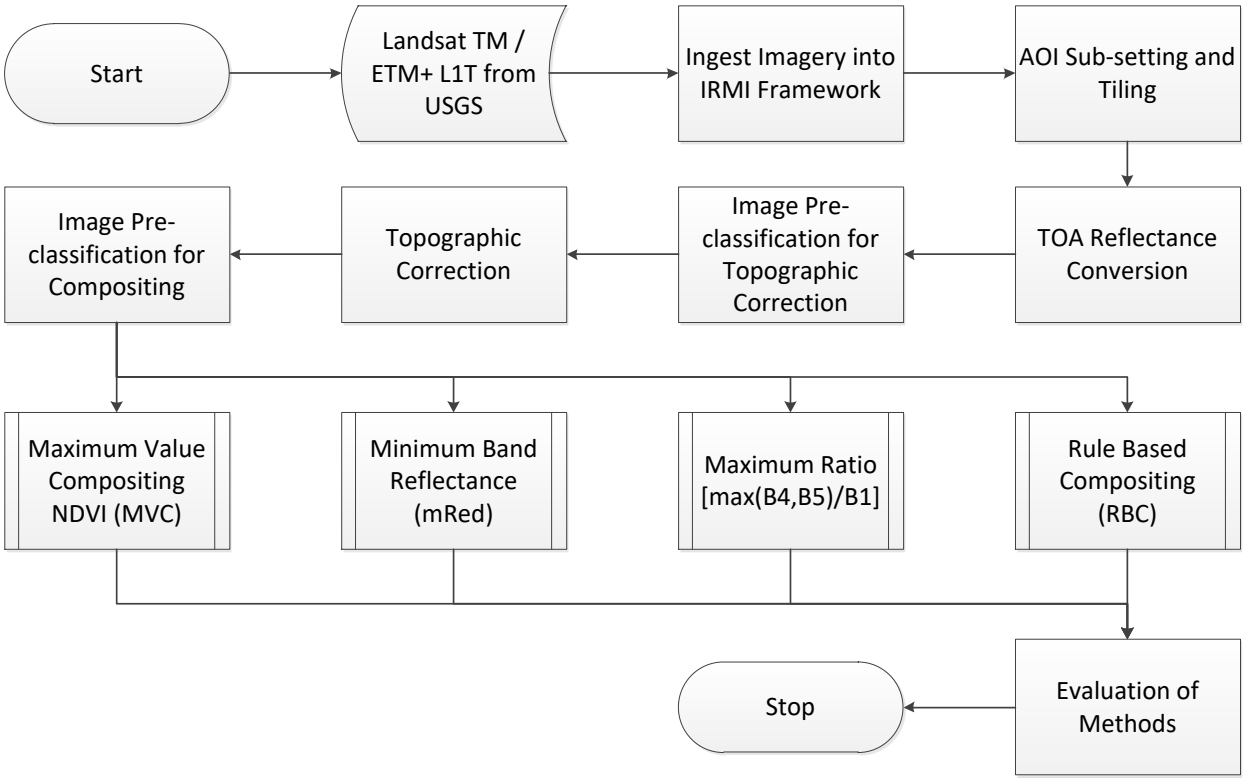

Figure 2-5 Experimental design for evaluating the MaxNDVI, MinRed, MaxRatio, and SBC image compositing techniques

2.3.5 Accuracy assessments

Quantitative accuracy assessment techniques evaluating the quality of an image composite are not well established and are poorly described in literature. Hagolle et al. (2005) suggested the use of regional variability as a compositing quality measure. This measure works well for composites generated from medium to low resolution sensors (e.g. AVHRR and MODIS), as BRDF effects between input scenes with large viewing angles are prominent, especially along scene edges. Small clouds also tend to be a problem for compositing at medium to low resolutions, but could be evaluated effectively by this technique. For higher resolution composites, such as those generated in this study, however, man-made features such as roads and field boundaries are more recognisable, and the high spectral variability of such features masks any variability introduced by compositing artefacts. Conversely, large areas of cloud shadow reduce variability, which, in turn, introduces a bias towards favouring cloudy composites. In spite of these deficiencies, the quality measure was included in this study for the sake of completeness. A 3x3 mean standard deviation filter was passed over the red band of each set of composites.

Mean standard deviation is defined as:

$$\bar{\Delta} = \sum_{i=0}^{n} \left| \frac{x - \bar{x}}{n} \right|$$ Equation 2-11

Where $\bar{\Delta}$ is the regional average;

n is the number of observations;

$\bar{x}$ is the mean difference in relative reflectance values within moving window; and

x is the reflectance value.

The red band was chosen because it is a good representation of the bands in the visible spectrum (high autocorrelation of all visible bands) and is least affected by the atmosphere. The mean variation $\bar{x}$ denotes the mean difference in relative reflectance values between pixels within the moving window.

According to Baraldi, Boschetti & Humber (2014), in many cases, no single summary statistic is capable of describing a complex property. A range of additional quality measures were therefore selected and used in combination to describe compositing quality.

In addition to the standard deviation measure, a new assessment measure was designed for the purpose of evaluating high resolution data. The measure aims to describe the relative quality of composites by comparing products of the same area. It is based on the principle that a large proportion of cloud pixels in a composite will lead to a larger proportion of pixels with high TC1 (brightness) values, as well as a higher standard deviation in brightness. Similarly, a higher ratio of shadow will lead to a larger proportion of low TC1 values and a higher standard deviation of TC1. The compositing techniques compared in this study are known for their efficiency in eliminating clouds (Luo, Trishchenko & Khlopenkov 2008), but are probably not as adept at removing cloud shadow. An additional test to evaluate a composite technique's ability to remove cloud shadow was consequently introduced by comparing composites and checking for increases in high TC3 (wetness) values. An increase in high TC3 is a good indication of a higher fraction of shadow, because the scattering of light in the blue and green part of the electromagnetic spectrum is far more pronounced than in the longer wavelengths, where it becomes negligible, especially in moist atmospheres which have an increased fraction of sky light. This ratio of relatively higher reflection in the shorter wavelengths, versus the long wavelengths over cloud shadow areas, is characterised effectively by the TC3 component as high positive coefficients, which are used with the blue and green band, whereas high negative coefficients are used for the near-infrared (NIR), shortwave infrared (SWIR) 1.6, and SWIR 2.1 bands (see Table 2-2). Cloud shadow, particularly over bright surfaces such as urban areas, is therefore more pronounced in

TC3 than TC1. Another motivation for including TC3 in the assessments was to reduce bias towards the RBC technique, as TC1 is a compositing criterion in this method.

The TC1 was calculated from reflectance values scaled by 10 000, and by using thresholds 2700 and 4,000, it was classified into low and high values respectively. Cloud shadow was synthesised using TC3 values of greater than -300. These thresholds effectively isolated areas with cloud and haze (*TC1 high*) and cloud shadow (*TC1 low* and *TC3 high*).

The composites of each study area were ranked from best to worst by considering the lowest mean values for *TC1 high* and *TC3 high*, and the highest mean value for *TC1 low*. In addition, a low standard deviation within these data segments was used as an indicator of a good composite, together with the smallest proportional area covered by these classes. A smaller proportion of cloud shadow will therefore lead to fewer pixels falling in the *TC1 low* and *TC3 high* classes.

All of the above compositing evaluation criteria can lead to incorrect assumptions, depending on the cloud cover percentage and surface features present. The following list describes exceptions when each criterion will fail to describe the quality of a composite.

1. High TC1: Low/dark cloud covering bright bare objects will not increase the mean of high TC1 values in a composite;
2. Low TC1: Cloud shadow covering naturally dark areas will not change the low TC1 values dramatically; and
3. TC3: In the case where clouds cover water or actively growing vegetation**,** there will be less picture elements with high TC3 values in a composite present. The relationship of these features to compositing quality can therefore not be quantitatively defined. This suggests an ordinal ranking of criteria performance.

For each of the above mentioned criteria, composites were ranked from best to worst, thereby scoring products from 3–0 (from best to worst). These scores were summed to produce an overall ranking for each composite per study area.

2.4 RESULTS

2.4.1 RBC results

Site C is used for illustrating the pre-processing, classification, topographic normalisation, and RBC compositing results. The automatic spectral pre-classification (Figure 2-6) produced a kappa coefficient of 0.82. The classes were defined by surface types with considerably different BRDF characteristics (e.g. woody versus herbaceous vegetation or bare surfaces) or classes that are not affected by topography (e.g. water and cloud), as these are either above the ground or on flat terrain.

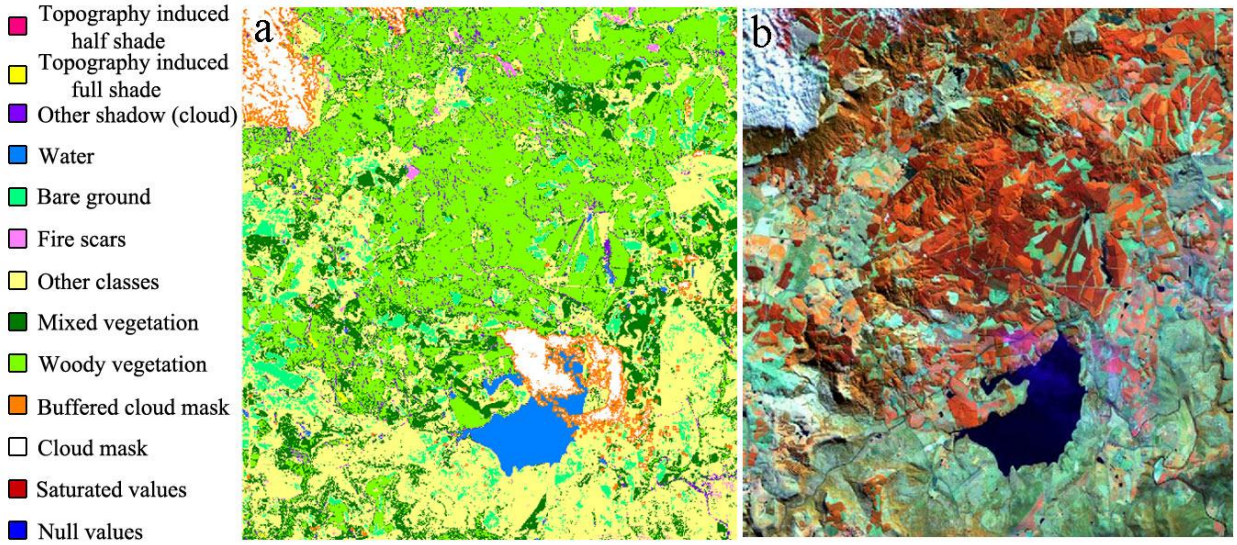

Figure 2-6 (a) Result of the spectral pre-classification for (b) the Landsat 5 TM image acquired on 28 May 2009 of a section of Site C

Figure 2-7 shows the effect of the topographic normalisation. After the correction there was no distinct relationship between solar incidence angle and TOA reflectance values per class, as can be seen in Figure 2-7. However, areas in complete shade or saturated pixels remained unchanged.

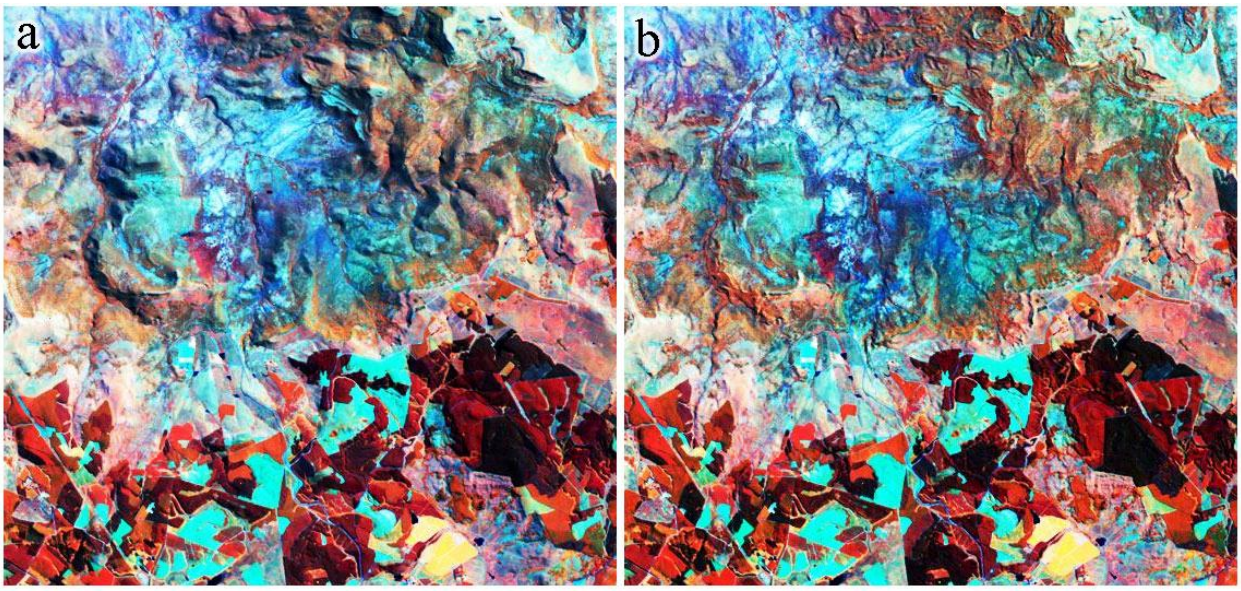

Figure 2-7 Topographically uncorrected (a) and normalised (b) Landsat 5 TM 453 band composite acquired on 25 March 2009 for Site C, illustrating the dramatic improvement in radiometry with a clearer identification of surface cover types and next-to-no shadow effects

Figure 2-8 shows the six images that underwent SRC and topographic normalisation. These images were used to generate the composite in c. The set of images include substantial cloud cover and SLC off error gaps, and pose a challenging case study due to the very limited number of suitable candidate pixels for a cloud and error-free composite. The pronounced phenological differences between the acquisitions caused a banding in the composite over natural woodlands.

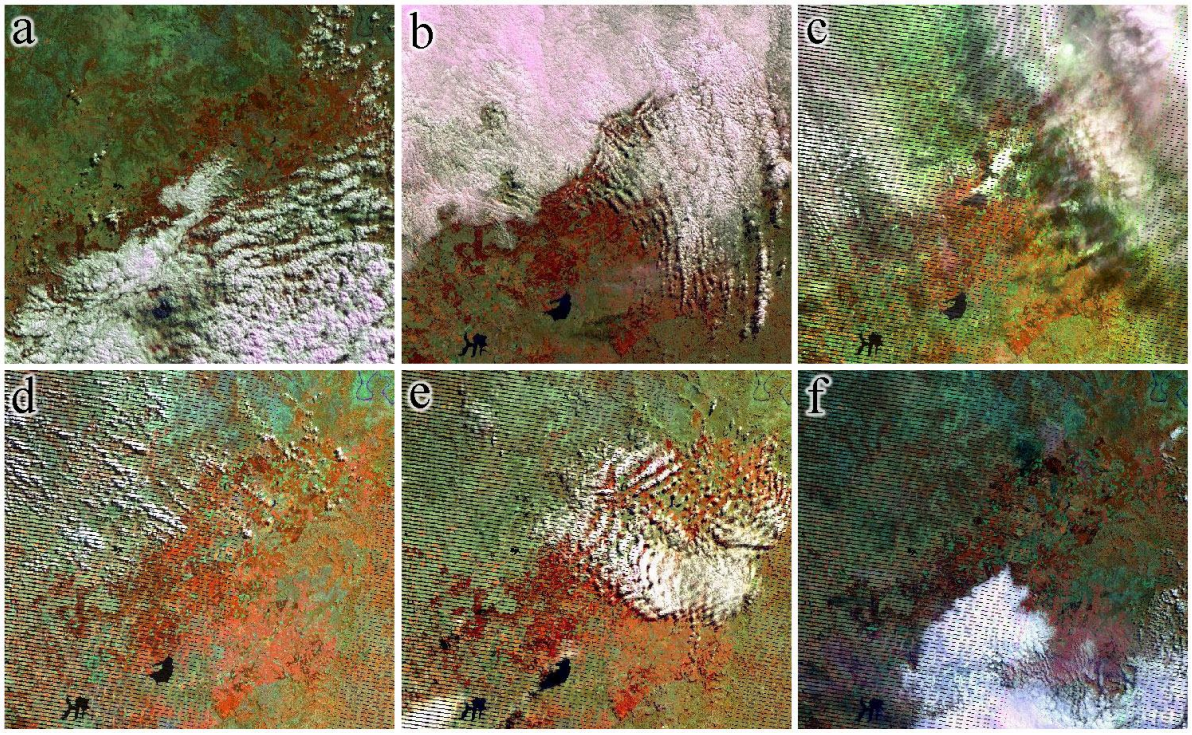

Figure 2-8 Topographically normalised Landsat 453 images used for Site C (Natal Midlands) to illustrate the compositing procedure. The images where acquired on (a) 26 April 2009, (b) 28 May 2009, (c) 4 May 2009, (d) 15 April 2008, (e)2 June 2008, and (f) 2 April 2009. Images (a) and (b) were captured using TM and the rest are from ETM+.

Figure 2-9 shows that the RBC produced almost seamless cloud and shadow-free mosaics. A slight corrugation effect is observed in the composite of Site A. This is due to the pronounced BRDF characteristics of forests and the right and left orientated acquisition angles of imagery from two Worldwide Reference System (WRS) paths being composited together.

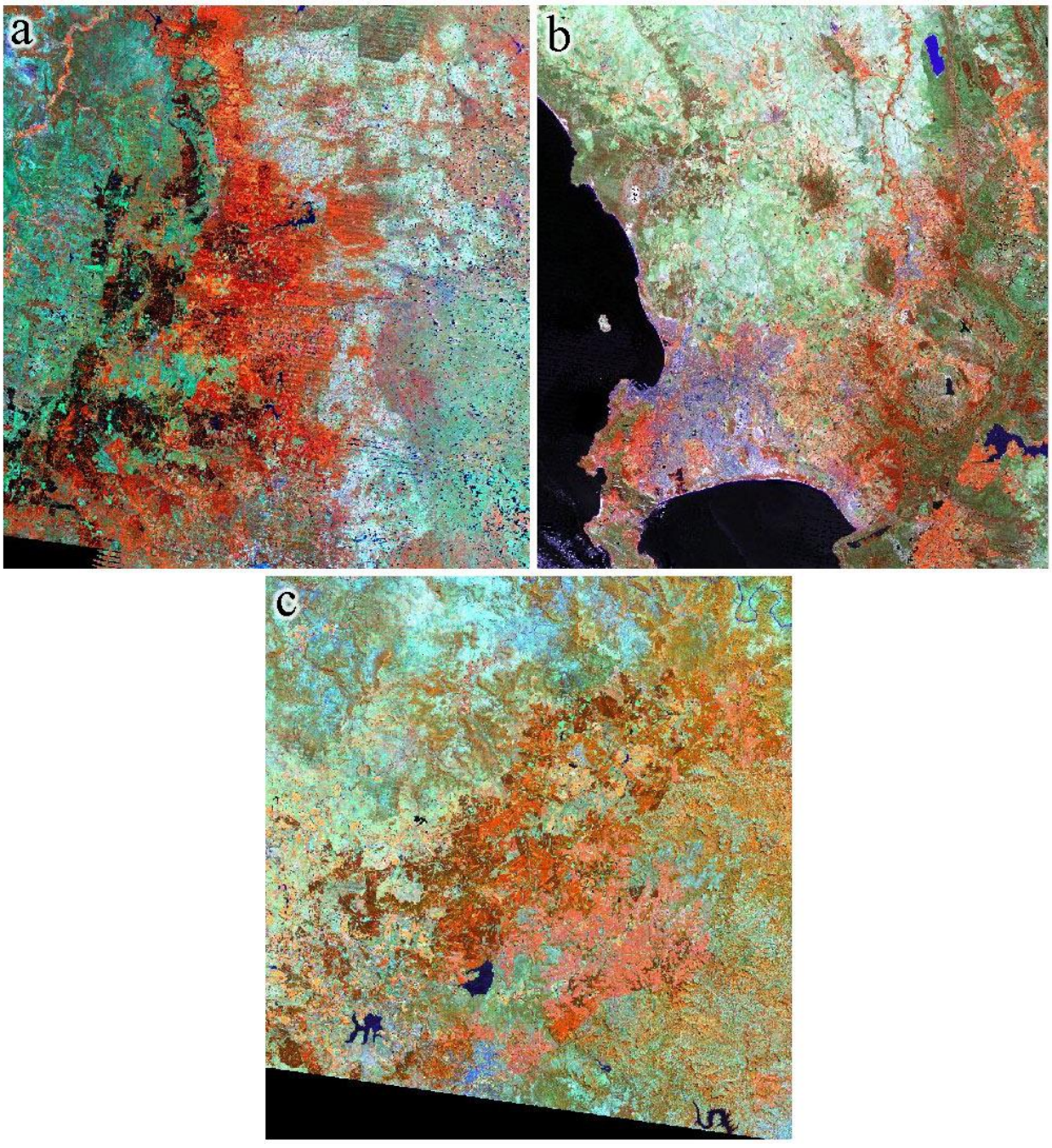

Figure 2-9 RBC results for (a) Site A, (b) Site B, and (c) Site C

2.4.2 Comparison of compositing techniques

The mean variance composite quality measures (Hagolle et al. 2005: 172) for each composite are shown in Table 2-3. Based on this quality measure, the MinRed composite scores the highest result as it contains a large proportion of cloud shadow areas with very little contrast. This is in contrast to a visual inspection of Figure 2-10, which clearly shows that the mean variance composite measure is not a suitable measure for composites generated from high resolution imagery.

Table 2-3 Mean variance in % reflectance of the red band between products and sites

Site	MaxNDVI	MaxRatio	MinRed	RBC	MaxNDVI Score	MaxRatio Score	MinRed Score	RBC Score
A	0.528	0.583	0.497	0.535	3	0	3	1
B	0.897	0.913	0.723	0.854	1	0	3	2
C	0.480	0.579	0.432	0.482	3	0	3	1
Total Score					**7**	**0**	**9**	**4**

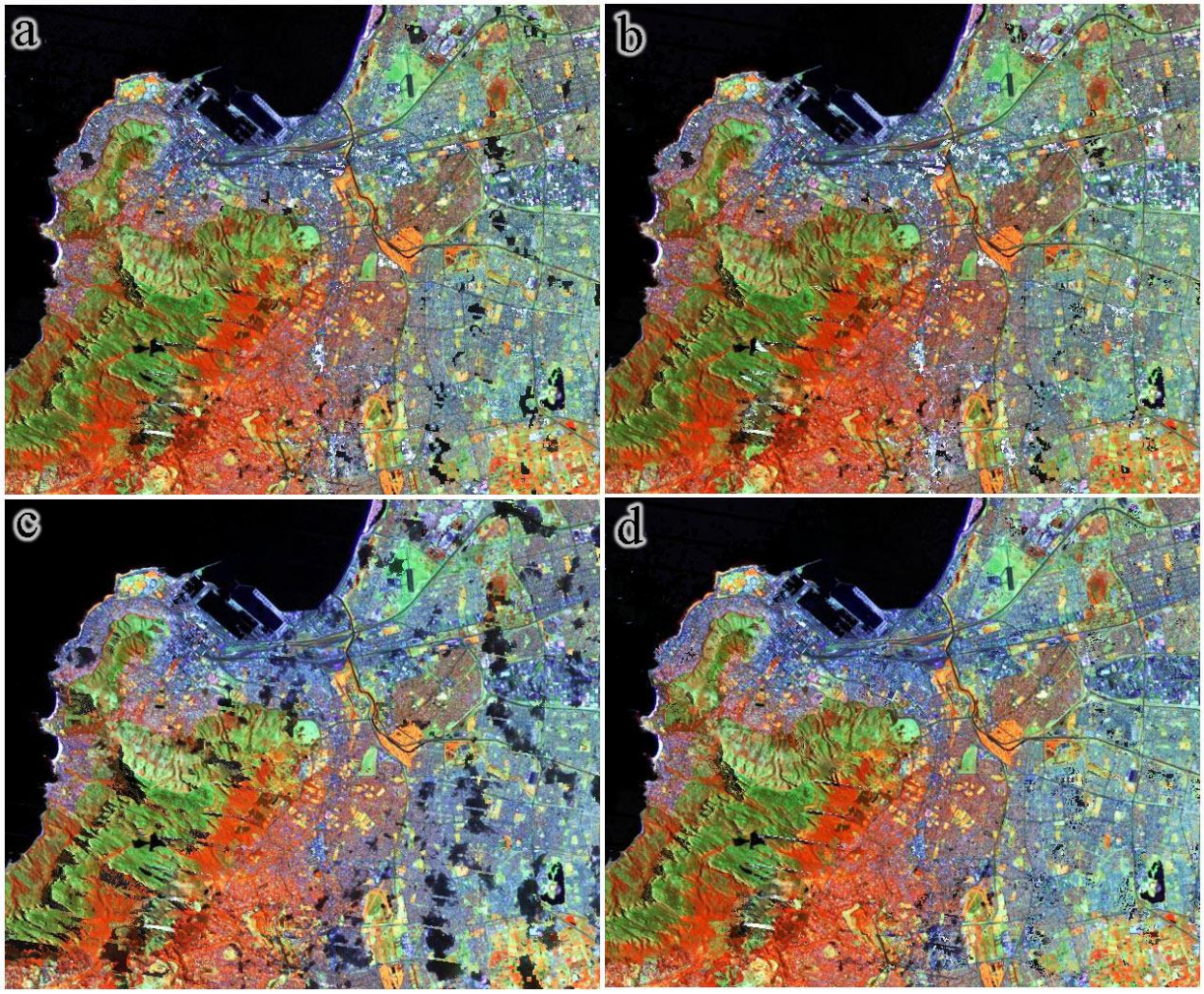

Figure 2-10 Visual comparison of (a) MaxNDVI, (b) MaxRatio, (c) MinRed, and (d) RBC

The results of the newly developed image composite quality measures based on TC1 and TC3 are summarised in Table 2-4. According to these measures, the RBC method outperformed all the other compositing techniques in each study area, with a total score of 56. When compared to

Figure 2-10, it is clear that the RBC was the most successful in reducing cloud shadow and haze over both urban areas and water bodies. MaxRatio also performed relatively well, with an overall score of 42. This is attributed to its ability to minimise cloud shadow; however, it failed to remove haze over water bodies and urban areas. This becomes apparent over the dam on Table Mountain and the urban area to the east of Table Mountain as depicted in

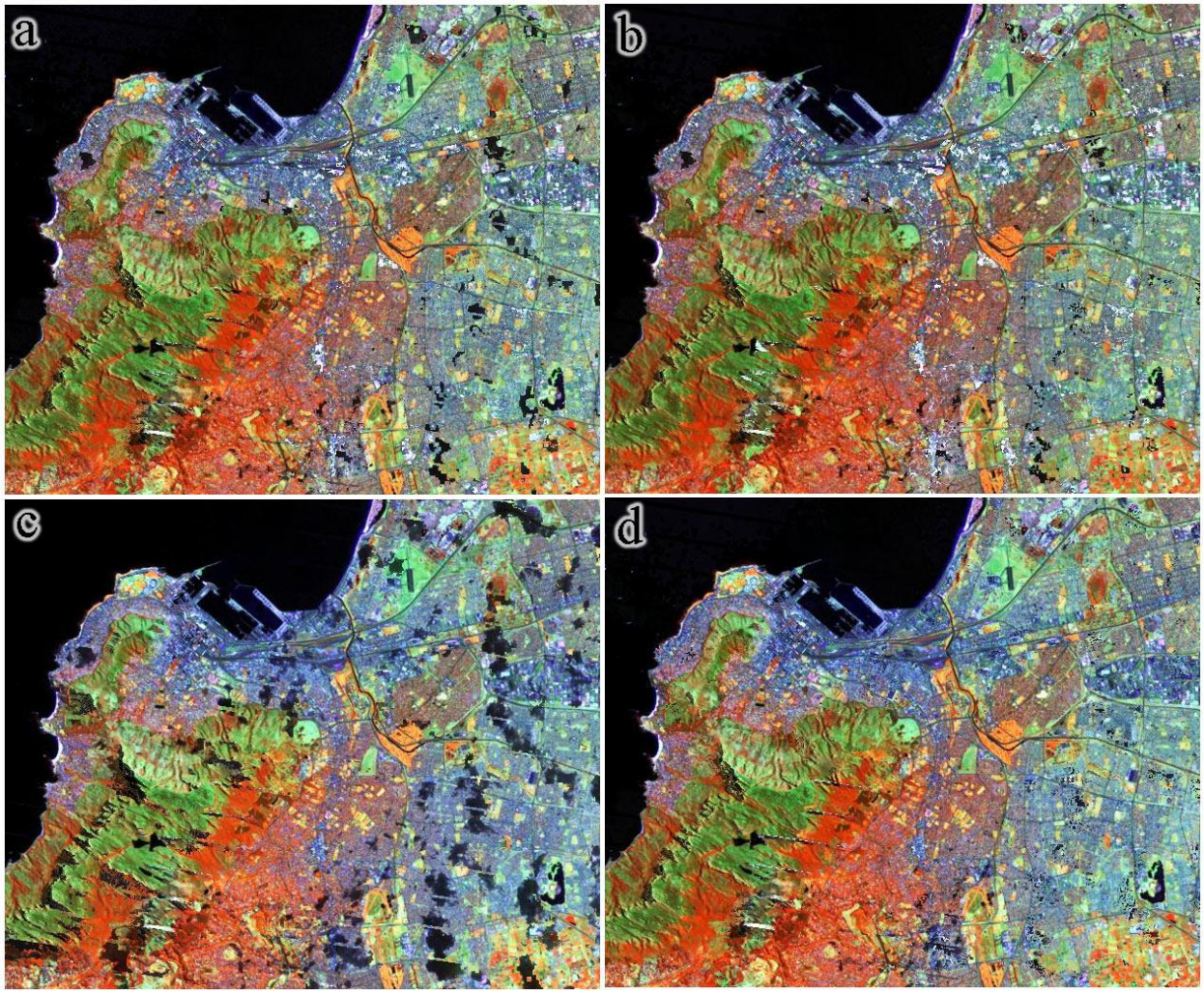

Figure 2-10 Visual comparison of (a) MaxNDVI, (b) MaxRatio, (c) MinRed, and (d) RBC

b. MinRed received the poorest overall score (27), mainly due to its inclusion of large areas of shadow. MaxNDVI had the lowest score (11) for Site B, confirming that this technique is less effective over non-vegetated surfaces. It has to be noted, however, that in some instances numeric differences between features are relatively small and may change depending on the levels of precision used for the comparison. In fact, high TC3$\bar{x}$ only differs for MaxNDVI and RBC at the third decimal. This emphasises once again that no single feature can be used for compositing quality assessment because the sensitivity varies depending on surface and cloud cover characteristics. This supports the argument for using only ordinal values as evaluation criteria, which is confirmed by the visual quality of the compositing products.

Table 2-4 Results of tasselled cap-based quality indicators for each site and composite method.

Feature	Site A				Site B				Site C			
	MaxNDVI	MaxRatio	MinRed	RBC	MaxNDVI	MaxRatio	MinRed	RBC	MaxNDVI	MaxRatio	MinRed	RBC
Low TC1 $\bar{x}$	23.18	23.38	20.67	23.30	15.14	14.47	15.20	15.21	23.96	24.13	21.56	23.99
High TC1 $\bar{x}$	43.55	43.78	43.63	43.48	46.85	47.34	45.53	46.55	42.92	43.33	42.74	42.72
High TC3 $\bar{x}$	-1.61	-1.67	-0.90	-1.65	2.51	2.64	2.22	2.50	-1.08	-1.06	-0.59	-1.08
Low TC1 σ	2.96	2.78	4.43	2.84	7.48	7.26	7.66	7.37	3.11	2.99	4.83	3.03
High TC1 σ	4.57	4.85	4.86	4.39	6.22	6.49	5.51	5.59	3.71	5.11	2.50	2.57
High TC3 σ	1.34	1.36	1.40	1.32	1.70	1.57	1.99	1.63	1.55	1.64	1.60	1.55
Low TC1 n	9.45	7.81	21.49	9.20	29.93	27.11	37.49	30.30	25.91	23.22	42.58	25.80
High TC1 n	10.04	11.13	6.94	10.50	30.21	34.75	20.29	29.81	1.86	2.51	1.14	1.96
High TC3 n	6.19	5.15	15.26	6.02	20.01	19.28	23.46	20.34	9.90	8.83	20.30	9.87
o Low TC1 $\bar{x}$	1	3	0	2	1	0	2	3	1	3	0	2
o High TC1 $\bar{x}$	2	0	1	3	1	0	3	2	1	0	2	3
o High TC3 $\bar{x}$	1	3	0	2	1	0	3	2	2	1	0	3
o Low TC1 σ	1	3	0	2	1	3	0	2	1	3	0	2
o High TC1 σ	2	1	0	3	1	0	3	2	1	0	3	2
o High TC3 σ	2	1	0	3	1	3	0	2	3	0	1	2
o Low TC1 n	1	3	0	2	2	3	0	1	1	3	0	2
o High TC1 n	2	0	3	1	1	0	3	2	2	0	3	1
o High TC3 n	1	3	0	2	2	3	0	1	1	3	0	2
Score Sum	**13**	**17**	**4**	**20**	**11**	**12**	**14**	**17**	**13**	**13**	**9**	**19**
Total Score	**37**	**42**	**27**	**56**								

The values represent the mean ($\bar{x}$), standard deviation (σ), and % coverage of each indicator. The bottom part of the table contains the ordinal numbers (indicated with prefix "o") for each indicator from best (3) to worst (0), as well as the cumulated ordinal numbers and total score for each composite method.

2.5 DISCUSSION

The spectral pre-classification used in the RBC proved to be robust across all three study sites. This classification ensured that surface types with similar BRDF characteristics are grouped together. Clouds were effectively separated from the remaining land cover types with the aid of the HOT, which is a prerequisite for pre-classification, topographic normalisation, and image compositing. The topographic normalisation dramatically improved the comparability of images acquired at different solar geometries, and laid the foundation for seamless composites that are suitable for the automatic extraction of thematic information. This is true for surfaces that have a low phenological response.

The qualitative comparison of the results suggest that existing techniques used for the evaluation of composites from medium to low resolution imagery (Hagolle et al. 2005) are not suitable for the evaluation of high resolution imagery. The tasselled cap-based indicators developed and implemented in this study seem to provide a better quantification of image composite quality, and correspond much better with visual (qualitative) interpretations of composite results. The study also demonstrated that a single statistical descriptor cannot adequately describe the quality of a composite. This can be attributed to the fact that no individual indicator can represent a low shade component, as it may not describe shade over vegetation, bare ground, or low cloud components well enough. In order for an adequate description of the quality of a composite, a

percentage of low or high TC values therefore has to be paired with standard deviation and mean values for each of these TC indicators.

The evaluation of compositing techniques confirmed the findings of Luo, Trishchenko & Khlopenkov (2008) who demonstrated that the MaxRatio technique outperformed the MaxNDVI and MinRed compositing techniques. The study showed that the MinRed technique was very successful in eliminating clouds, but was biased towards cloud shadow and brought most shadow- contaminated pixels into the composite. This also applied to topography-induced full shade on steep slopes, which could not be corrected with topographic normalisation due to a very low signal or no-signal.

The MaxNDVI technique was able to eliminate cloud and shadow when the underlying surface was vegetated, but performed poorly over bare surfaces. It was particularly unsuccessful in eliminating cloud and haze over bare or urban areas, as can be seen in Figure 2-10a (urban areas of Cape Town).

The MaxRatio technique was relatively successful in eliminating cloud shadow, but, as with MaxNDVI, struggled over bare areas. It was biased towards haze and cloud pixels over water, even more so than MaxNDVI. But unlike MaxNDVI, it did not favour the strongest vegetation signal (a property the NDVI is renowned for). This was confirmed by its poor performance in the *TC1 High* and *TC3 n* (percentage cover) indicators.

The RBC technique combines the advantages of both MaxNDVI and MaxRatio, and the use of maximum HOT for bare surfaces ensures that pixels of urban areas and water bodies are atmospherically clear.

It is hereby deduced that this novel approach performs better than traditional ones because it uses a hybrid inference whereby inductive data-learning, provided by the pre-classification, is better suited to the application of a compositing technique optimised for surface types.

2.6 CONCLUSION

In this paper a new method for the generation of image composites was introduced. This method, called RBC, incorporates a range of pre-processing techniques and has the ability to transform a set of cloudy images with many missing observations (e.g. Landsat ETM+ post SLC error data) to cloud- and shadow-free composites suitable for forestry applications. The input data is converted to TOA reflectance, after which a pre-classification allows for a stratified topographic normalisation.

The RBC was compared to three other compositing techniques, of which the MinRed method provided the best results. These results were based on an existing quality indicator that quantifies variability across seam lines. A visual assessment of the MinRed composite images, however, revealed that the technique transfers all shady pixels in the input imagery to the composite. This defect is not reflected in the existing quantitative measure. The MaxRatio compositing technique was found to favour bright surfaces and thus showed a relatively high variability across the seam lines.

A new set of quantitative indicators was developed to better reflect image composite quality. The new indicators are based on tasselled cap components and were found to provide a much better quantification of the proportion of cloudy and shady pixels. When applied to the outputs of compositing techniques, RBC was found to outperform the other three methods evaluated. This outcome was confirmed using visual interpretation of the composite images. The success of RBC is attributed to its ability to combine the advantages of several techniques, while at the same time relying on prior knowledge of underlying spectral classes, as the areas to be composited are stratified according to different criteria. Although RBC is more computationally intensive, it provides the greatest scope for adaptation to various spectral criteria. More work, however, is required to optimise this technique.

CHAPTER 3: AUTOMATIC CLASSIFICATION OF INDIGENOUS AND PLANTATION FORESTS FROM LANDSAT TM AND ETM+ IMAGERY

3.1 ABSTRACT

The mapping of indigenous and plantation forests from satellite imagery has received considerable attention during the last few decades. Advanced classifiers such as support vector machines (SVM) and random forest (RF) have become popular as they often provide superior results on a case-by-case basis. This study compared the performance of fully-automated machine learning classifiers when applied to segments extracted from composite Landsat 5 and 7 imagery – i.e. in an geographic object-based image analysis (GEOBIA) paradigm – for classifying evergreen subtropical rain and plantation forests. Three sites with different types of forests, spaced 500 to 1500 km from one another within South Africa, were used to validate the transferability of the techniques and signatures. Three rule-based classification techniques and two machine learning classifications were evaluated and compared. The rule-based classification techniques are: spectral rule-based classification (SRC) developed by the European Joint Research Centre, spectral rules as implemented in SPECL and developed by the German Space Agency (DLR), and a novel optimised spectral rule-based classification (OSRBC). The two machine learning classifiers considered are SVM and RF.

The findings are that generic rule-based classifiers such as SPECL and the SRC are too generalised to discriminate and isolate specific forest classes. Furthermore, it was found that a direct comparison between these classifiers was not possible as a one-to-one mapping of the forest classes could not be achieved. The OSRBC produced an accuracy of 80% with a kappa value of 0.78, but requires a good separation of classes in feature space and leads to a non-exhaustive classification. The machine learning techniques show great promise, with both the RF and SVM achieving classification accuracies of 93–98%, with SVM slightly outperforming RF. Classification accuracies were not significantly different when training samples from areas 1500 km away were used. This implies that the class signatures of the machine learning classifiers can be applied to sites across space and time, so long as good image normalisation (with the preservation of spectral, textural, and contextual properties) is implemented.

Keywords: image compositing, automatic forest classification, spectral rule-based classification

3.2 INTRODUCTION

Indigenous forests and forest plantations are important global natural resources and are subject to natural and anthropogenic disturbances that need to be monitored by governments (Boqo & Mashate 2010), natural resource management agencies (Dyk et al. 2015), and forestry companies (Von Gadow & Murray 1989). As these natural resources are threatened by over-exploitation and natural disasters such as fires, drought, pests, and diseases, a rapid, frequent, inexpensive, and accurate mapping of forests is required (Ozdogan & Schumann 2014). Remote sensing provides a suitable technology to generate these information layers, and free, well-calibrated Landsat imagery makes this feasible (Köhl, Magnussen & Marchetti 2006). This is particularly important in light of climate change mitigation and carbon trading activities facilitated through the REDD+ programme (Achard 2012). For REDD+, the fluctuations of carbon stocks and the delineation of areas containing above ground woody biomass within the areas are important (Parker et al. 2009). To facilitate carbon trading, errors of carbon stock and their fluctuations need to be known and should be sufficiently small to allow a confidently measured increase in carbon stock or a decrease in depletion rates to be traded (Kollmuss 2010). Forestry companies need a good understanding of the type, volume, and location of forest plantations. This is particularly relevant in the Southern African environment where commercial forestry companies need to purchase dilapidated plantations in neighbouring countries, or need to purchase their timber from private growers (Mead 2001) who do not have or do not want to share this confidential information. Government bodies, in turn, also need to know the extent, cover changes, and nature of forest plantations for legislation enforcement (South Africa 1998). Landsat data's spatial resolution and coverage, spectral properties, and systematic acquisition makes it ideal for forest resource assessment, which has been one of the first applications of this data (Hildebrandt 1990).

With the Landsat program's goal of a cloud-free quarterly acquisition of all land masses within a year (Arvidson, Gasch & Goward 2001), the forestry sector, with its relatively low rates of cover change compared to that of agriculture, can be ideally served with this data (Kim et al. 2014). The free access to the Landsat archives via the USGS since 2009 (Roy et al. 2010) allows the full use of this imagery for operational applications. This means that with a minimum mapping unit of a hectare, forest classifications can be updated at a quarterly interval while providing discrimination between broad forest classes.

Over the past few years, the use of machine learning classifiers and GEOBIA techniques have become popular. Neural network (NN) classifiers, SVM, and RF are examples of machine learning classifiers. NN classifiers have evolved to artificial neural network and deep learning or

deep neural networks popular in research fields of artificial intelligence. SVMs are popular in cases where a relatively small and uneven distribution of samples for classes exist, whereas RF performs well with an evenly distributed set of samples over all classes. Deep neural networks, however, require a very large number of samples to be effective (but then often outperforms all other techniques).

RF have been successfully used to predict the age of *Pinus patula* using ASIA Eagle hyperspectral imagery with a model accuracy of $R^2 = 0.6$ (Dye, Mutanga & Ismail 2011). It has also been used on spectral and textural features extracted from QuickBird imagery to get an estimated age with $R^2 = 0.68$ for *Pinus patula* forests in KwaZulu-Natal, South Africa (Dye, Mutanga & Ismail 2012).

RF and SVM classifiers have been found to have a similar performance for a land cover classification using ETM+ imagery over the UK when an equalised random sample for observations per class is ensured, as required by RF classifications (Pal 2005). It has been shown that while there is an age-dependant spectral variability in forests, it is less pronounced than a species-dependant spectral variability (i.e. the spectral variability between stands of different age classes of a single species is less pronounced than the spectral variability between stands of different species made up of all age classes). Even so, taking the effect of age into account has increased the classification accuracy from 85% to 97% on a hyperspectral dataset for plantation species in KwaZulu-Natal when using a classification and regression tree (CART) classification (Van Aardt & Norris-Rogers 2008). Age and structure was estimated as early as 1995 by Cohen, Spies & Fiorella (1995) using Landsat TM imagery over the western Oregon USA.

Satellite imagery consists of picture elements (pixels) representing radiation measurements taken over different spectral bands. These pixels are arranged spatially in context to the land surface they represent, providing textural, relational, and contextual information. Over the last decade, object-based image analysis (OBIA), also known as GEOBIA, has become popular through the software package eCognition, released in 1999. In GEOBIA images are abstracted into segments or objects representing pixels of similar properties. Segments are constructed over areas with similar textural and spectral properties, and confined to scale and compactness thresholds. Rule-based classifications work well with GEOBIA, as a multitude of features (such as texture and topological relations) can be calculated for each image segment. Given that contextual information becomes more prominent in high resolution imagery – and that such imagery is expensive and seldom radiometrically normalised – GEOBIA image exploitation techniques have focused on spectrally insensitive features or the development of rulesets that can be manually adapted from image to image. GEOBIA, however, has traditionally been considered

computation intensive when implemented in specialised and expensive software such as eCognition (Lewinski & Bochenek 2008; Lewinski 2005).

Over the past few years, GEOBIA has been combined successfully with machine learning classifiers (such as NN classification) to discriminate between pitch canker-infected *Pinus radiata* trees. Following the segmentation of individual tree crowns, an overall detection accuracy of 82.15% was achieved when using very high resolution QuickBird imagery (Poona & Ismail 2013).

For geoinformation service delivery to be operational, the extraction of thematic and spatial content from imagery must be of a high quality, be stable, show the desired thematic content, and preferably be fully automated, as demonstrated by Rasi et al. (2013) in a study detecting forest change. In the past, satellite imagery was expensive, poorly calibrated, and radiometric and geometric correction methods were poorly understood. This led to the implementation of qualitative, labour intensive, scene-based image classification techniques, often reliant on statistical classifiers (Landgrebe 1997). In recent years, there has been a paradigm shift to the adoption of physical vs. empirical models for image correction, and pre-processing and classification have been performed based on a better radiometric, spectral and geometric characterisation of the imagery, resulting in improved calibration of historic and recent Landsat TM and ETM+ imagery (Baraldi 2009). This enhanced image quality can be attributed mainly to the sound ground segment infrastructure at some Landsat ground receiving stations that use the USGS in-house developed LPGS (Landsat Product Generation System) software (Ihlen 2012).

A trend towards automating classification approaches for forest cover assessment has been observed. Large mapping projects such as the EOSD in Canada for the year 2000 timeframe required some degree of radiometric normalisation to TOA reflectance, followed by an automatic NDVI-based stratification and an unsupervised K means classification with manual recoding (Wulder et al. 2008).

With well-calibrated Landsat imagery, an accurate conversion to TOA reflectance has become feasible. This normalisation has enabled the development of automated SRCs, such as the one developed at the European Joint Research Council, which thematically segments Landsat imagery into 46 spectral classes (Baraldi et al. 2006). This classification is based on the calculation of special features and indices, as well as the direct spectral values of bands that are in turn classified into high, medium, and low categories. Spectral pre-classifications can support further radiometric normalisation techniques developed by radiation transfer specialists with their respective atmospheric correction software packages such as Atcor (Richter 2011a) and 6S (Ouaidrari & Vermote 1999).

With the failure of the scan line correction mirror on Landsat-7 ETM+, approximately 24% of a scene consists of no data, making image compositing commonly performed on MODIS and AVHRR products vitally important. This was done effectively in the WELD system developed by Roy et al. (2010), producing cloud-free annual, seasonal, monthly, and weekly seamless image composites at TOA reflectance and at surface (AS) reflectance (Lück & Van Niekerk 2016).

Automated spectral rule-based classifiers, such as those developed by Baraldi et al. (2006) and implemented in his SIAM software package, provide a pre-classification necessary for automated cloud and cloud shadow masking and produce sound topographic normalisations using the modified Minnaert correction. This in turn is a prerequisite for quantitative classification methods in areas of strong topographic relief and low solar illumination angles (Baraldi, Gironda & Simonetti 2010), both of which are generally prominent in forested areas.

The ability to extend signatures and develop classification techniques that can address large area mapping from satellite images has been identified as a research priority by Chilar (2000). Inter-image spectral variation, which affects the ability to discriminate between different land cover classes over large geographic extents, has been studied by Verhulp & Van Niekerk (2016). Furthermore, it has been found to be particularly difficult to discriminate between land cover classes that vary greatly in spectral properties over distance and time. Forest plantations generally consist of uniform blocks of trees with distinct spectral properties that are not expected to vary greatly over space and time.

It is the objective of this research to examine if signatures for forestry classes can be transferred between distant geographic areas for use in machine learning classifiers. Furthermore, the performance of these machine learning classifiers trained on geographically unrelated samples are to be compared with existing and new rule-based classifiers.

This study compares two machine learning classifiers, SVM and RF, and three rule-based classifications, namely SRC, SPECLE, and optimised spectral rule-based classification (OSRBC), a newly developed technique. OSRBC examines the optimal separability of classes to define specific thresholds that can be used to automatically construct an effective rule base. The imagery used as input to the different methods was preprocessed according to methodologies developed by Roy (2011), Baraldi, Gironda & Simonetti (2010), and Lück & Van Niekerk (2016). These processes were embedded into a single automated processing chain, which was implemented in PCI Geomatica 2012 (PCI Geomatics 2012). All classifications are performed on a segmentation layer generated with the PCI Geomatica 2017 GEOBIA tool for consistency and comparability.

3.3 MATERIALS AND METHODS

3.3.1 Study areas

To test the transferability of the developed techniques, three study areas in South Africa were chosen. Each area contains some degree of indigenous forest cover and forestry plantation. Site selection was based on accessibility for ground-based validation and to provide a representative range of different forest types, climatic zones, and strong topographic relief with frequent cloud cover. The study areas are within one-by-one degree blocks, as depicted in Figure 3-1.

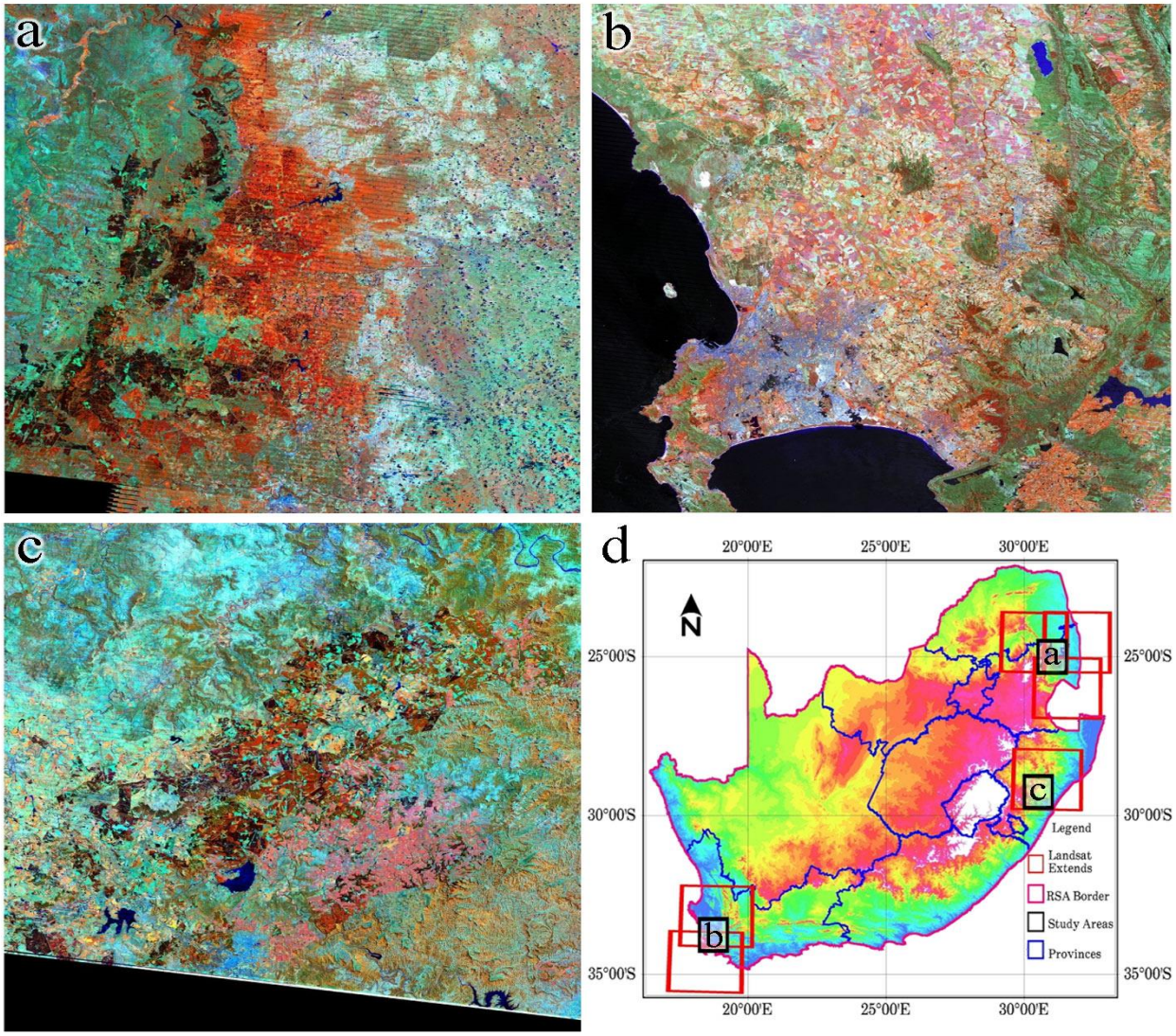

Figure 3-1 Study areas used to evaluate the selected automatic image classification: (a) KNP 2430 Low Veld, (b) CPT 3318 Western Cape, (c) KZN 2930 Natal Midlands, with their respective location shown in (d) an elevation map of South Africa. Image composites are Landsat ETM+ false colour image composites displayed in a 453 band combination.

Each study area is shortly described below:

Site A 2530 Low Veld Figure 3-1(a): The area is defined by the following bounding coordinates: 30.5° E, 24.5° S and 31.5° E, 25.5° S. An abbreviation of KNP is used for this area throughout the chapter. This region includes the biggest extent of contiguous commercial forestry in South Africa, with dominant plantation species being *Pinus patula*, *Pinus elliotii*, *Pinus taeda*, *Eucalyptus grandis*, and *Eucalyptus nitens*, as well as various Eucalyptus hybrids. Afromontane rainforests occur along the steep slopes of the escarpment and are often found in steep gorges. Elevation ranges between 283 m to 2255 m. The area experiences a subtropical climate with a distinct rainy and dry season cycle that is responsible for strong phonological spectral response fluctuations over the course of the year. This effect is particularly prominent in the lower-lying savannah and dry forest areas.

Site B 3318 Western Cape Figure 3-1 (b): The area is defined by the following bounding coordinates: 18.25° E, 33.25° S and 19.25° E, 34.25° S. Abbreviated as CPT, it includes parts of the Cape Town metropolitan area and the towns of Stellenbosch, Paarl, and Grabouw, with forest plantations of *Pinus pinea*, *Pinus radiata* and *Eucalyptus grandis* as well as some remnants of Afromontane rainforests in the gorges of steep mountain slopes. Elevation ranges between zero to 1976.4 m above mean sea level, and clouds over the mountains are frequent. Most forests found in this area grow on steep slopes of the Hottentots Holland Mountains, Stellenbosch Mountain, Jonkershoek Mountains, Simonsberg, and Table Mountain. The area has a Mediterranean climate, with most of the rainfall emanating from subtropical cyclones in winter.

Site C 2930 Natal Midlands Figure 3-1 (c): The area is defined by the following bounding coordinates: 30° E, 28.75° S and 31° E, 29.75 ° S. Abbreviated as KZN, it is situated in the Natal Midlands in the province of Kwa-Zulu Natal. The Natal Midlands is a major forestry area, particularly the areas north of Pietermaritzburg. *Pinus patula*, *Pinus elliotii*, *Pinus taeda*, *Eucalyptus grandis*, *Eucalyptus nitens*, and *Acacia mearnsii* are the main plantation forestry species in this area. Afromontane rainforests occur in larger patches on the slopes of the escarpments and in steep gorges. The landscape is characterised by steep escarpment slopes and rolling hills. Elevation ranges from 44 m to 1761 m above mean sea level, and rainfall is relatively high (600–1000 mm/a); however, the north-eastern corner of the study area is dryer and is covered by grassland.

Although forest classification is the focus of this research, classification techniques often require a full thematic segmentation of the data. For this reason, major thematic classes, as described in the South African Land Cover Class Definition Report (Lück & Diemer 2008), have been incorporated into the classifications and are listed in Table 3-1. These classes are prefixed with their class code and a generic description. Classes with a 1xx prefix represent natural vegetation,

3xx cover cultivated classes, 500 is bare, 6xx include man-made infrastructure and settlements, and 700 is water. Class labels in bold are the desired forest classes to be extracted.

Table 3-1 Land cover classes used to isolate forest classes

101 dry woodland	Areas with trees of various tree cover densities from 15% upwards, with remaining woody cover consisting of shrubs and bushes of no more than twice that of tree cover. Trees are considered as woody vegetation with a distinct crown elevated >1.5 m above ground with a total height of >3 m (considering that the crown elevation above ground is difficult to measure with conventional remote sensing, total height is the dominant classifier here).
101 green woodland	
101 rain forest	
101 riparian forest	
102 shrubs	Areas dominated by shrubs and bushes with a woody cover of >15% and a tree cover of less than twice that of the remaining woody cover. Shrubs and bushes may vary in height of up to 3 m.
104 dry grassland	Areas dominated by graminoids with >4% vegetation cover.
104 green grassland	
301 *Pinus*	All trees bearing needle leaves or leaves of similar leaf structure (e.g. beefwood).
302 *Eucalyptus*	All trees shedding leaves thought the year while maintaining a fair amount of foliage throughout.
302 *Acacia*	
303 fruit trees	Broad-leaved trees losing all their foliage as part of a natural annual cycle during a specific season.
304 vineyards	Broad-leaved bushes and shrubs not exceeding the height of 3 m.
305 maize	All herbaceous graminoids such as grasses, maize, sugar cane, and cereals.
305 sugar	
306 banana	All herbaceous non-graminoids such as cotton, sunflower, peanuts, potatoes, etc.
500 bare	This class describes areas that do not have an artificial cover as a result of human activities. These areas include areas with less than 4% vegetative cover. Included are bare rock areas, sands, and deserts.
601 linear feature	Built-up linear feature with a length of over 500 m consisting of runways, landing strips, roads, railways, utility lines, and other.
602 commercial	Built-up areas supporting any form of industry and commerce including non-residential areas.
603 residential	Any built-up areas where people live on a permanent or semi-permanent basis. This includes rural dwellings of low settlement density.
700 water	Natural non-vegetated aquatic or regularly flooded water bodies.

3.3.2 Data and imagery used

A total of 174 Landsat 5 TM and Landsat-7 ETM+ scenes between 2008–2010 with a cloud cover of less than 50% were selected for the study sites. These acquisitions were ordered from the USGS GLOVIS catalogue and downloaded in batch mode. All images were processed by the USGS to L1T with the LPGS system prior to download. A 5 m DEM generated by the Centre for Geographical Analysis (CGA) was used for the radiometric topographic normalisation of imagery. Imagery was preprocessed as described in Lück & Van Niekerk (2016). All preprocessed and corrected data was provided in top of atmosphere (TOA) reflectance, scaled to 1:10 000 and stored in signed 16 bit format.

3.3.3 Experimental design

The workflow of this study is illustrated in Figure 3-2. Field campaigns were undertaken for each study area on the dates outlined in Table 3-2. The field campaigns consisted of both ground-based road transects and aerial transects. For the road transects, circular routes were selected, which were evenly distributed over each study area. Sample points were then extracted from the road vector dataset using stratified random sampling weighted according to land cover

classes of an existing land cover map generated in 2000. These points were then visited and geo-tagged photographs were taken from the roadside. Four evenly-spaced aerial transects over the Low Veld study area were selected and studied from a helicopter flying at low altitude. A continuous sequence of geo-tagged photographs were taken from the helicopter during the flight, following a systematic sampling design. A total of 1165 samples were collected.

Table 3-2 Field campaign dates for ruleset development and validation

Study area	Dates
Site A: KNP (2530 Low Veld)	2009/07/30 to 2009/08/01
Site B: CPT (3318 Western Cape)	2009/07/10 to 2009/07/18
Site C: KZN (2930 Natal Midlands)	2009/11/07 to 2009/11/11

All geo-tagged photographs were interpreted and corresponding land cover classes digitised on screen from orthorectified 2.5 m pan-sharpened, false colour Spot 5 imagery from the high resolution geometry (HRG) sensor. Resulting vector polygons were used to select image segments attributed to classes for training and validation. The downloaded Landsat 5 TM and Landsat-7 ETM+ imagery (at the orthorectified L1T processing level) were incorporated into a workflow management framework called the image resource management and information system (IRMI), which was equipped with libraries and functions provided by PCI Geomatica 2012 software (PCI Geomatics, 2012). Metadata required for radiometric and geometric image processing was extracted from accompanying image header files. Image manipulation and processing were handled by automated processing chains scripted in the EASI modelling language of PCI Geomatica 2012. Imagery was clipped to the extents of the study areas, converted to TOA reflectance, scaled to 1:10 000, and stored as signed 16 bit integer images. SRC was used to classify each image into classes with different BRDF properties (excluding clouds and water), which were then used to calculate the Minnaert coefficient for the topographic normalisation as proposed by Baraldi, Gironda & Simonetti (2010).

Rules for image compositing were applied to imagery based on SRC classes favouring the forest classes. Compositing provided a seamless, cloud-, shadow-, and gap-free image tile as described by Roy (2011). Details on these image processing techniques are described in Lück & Van Niekerk (2016). The spectral characterisation of classes to be extracted are described in Section 3.3.4.1, and the transformation of these spectral signatures to meaningful indices and features are described in Section 3.3.4.2. A general temporal characterisation illustrating the sensitivity of spectral signatures to annual phenological and life cycle fluctuations is provided in Section 3.3.4.3. The three SRCs, a SVM and a RF classification are subsequently compared and evaluated. For the OSRBC, SVM, and RF classifications, samples from all three study areas were separated into a training dataset and a validation dataset in order to compare these methods

with one another objectively.

The accuracy results of the three classifiers will be used to test the hypothesis that signatures can be successfully transferred between sites that are up to 1500 km away from one another (e.g. CPT and KNP). To test the feasibility of signature extension, SVM and RF classifications are compared by training the classifier only on samples from within a specific study area, versus training the classifier on the combined sample set from the two remaining study areas. In other words, for the classification of Site A (KNP), the combined training samples from Site B (CPT) and Site C (KZN) were used; for Site B, the training samples from Sites A and C were used; and for Site C, the training samples from Site A and B were used.

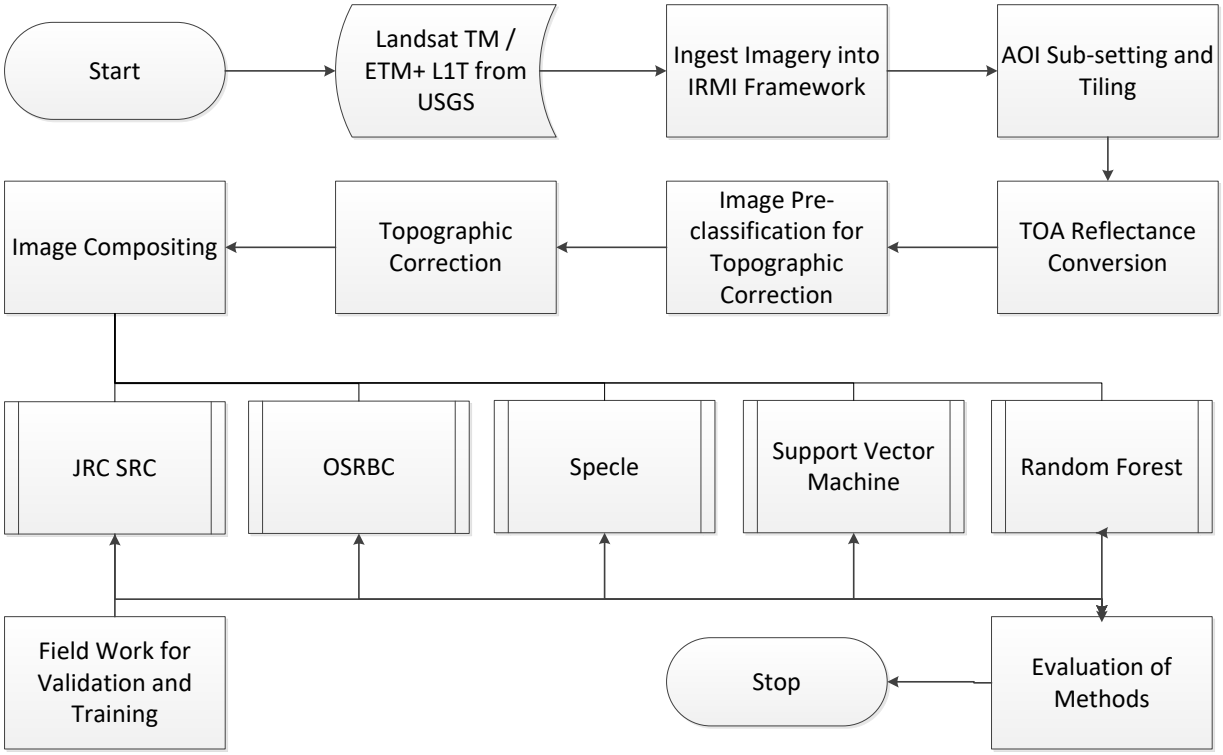

Figure 3-2 Workflow leading to the evaluation of different classifiers for forest type classification

3.3.4 Spectral/temporal characteristics of classes

3.3.4.1 Spectral characteristics

The Landsat TM and ETM+ imagery used in this study has seven spectral bands that represent specific parts of the electromagnetic spectrum. Their common names are denoted in Table 3-3 and will henceforth be used.

Table 3-3 Landsat TM and ETM+ spectral bands, common names, and wavelength ranges

Band	Common Name	Wavelength
1	Blue	0.45 µm–0.52 µm
2	Green	0.52 µm–0.60 µm
3	Red	0.63 µm–0.69 µm
4	NIR	0.76 µm–0.90 µm
5	SWIR 1.6	1.55 µm–1.75 µm
6	Thermal	10.40 µm–12.50 µm
7	SWIR 2.1	2.08 µm–2.35 µm

Adjusted from Irish (2012)

A good calibration of spectral data is a prerequisite for the definition of stable classification rulesets as highlighted by Baraldi (2009). In this study, forests are classified from single image composites, and the spectral resolution of Landsat is used as the main information contributor for each classification. Figure 3-3 below illustrates the spectral signatures of land cover classes selected for classification, with signatures derived from the mean value per class. The figure does not illustrate the within-class variation as this could not be displayed effectively in a 20-class line graph; however, it is presented in Table 3-4. From Figure 3-3, it becomes evident that classes cannot be easily discriminated from each other by considering spectral bands alone, thus indicating that spectral transformations in the form of indices and linear combinations need to be used to provide better separation.

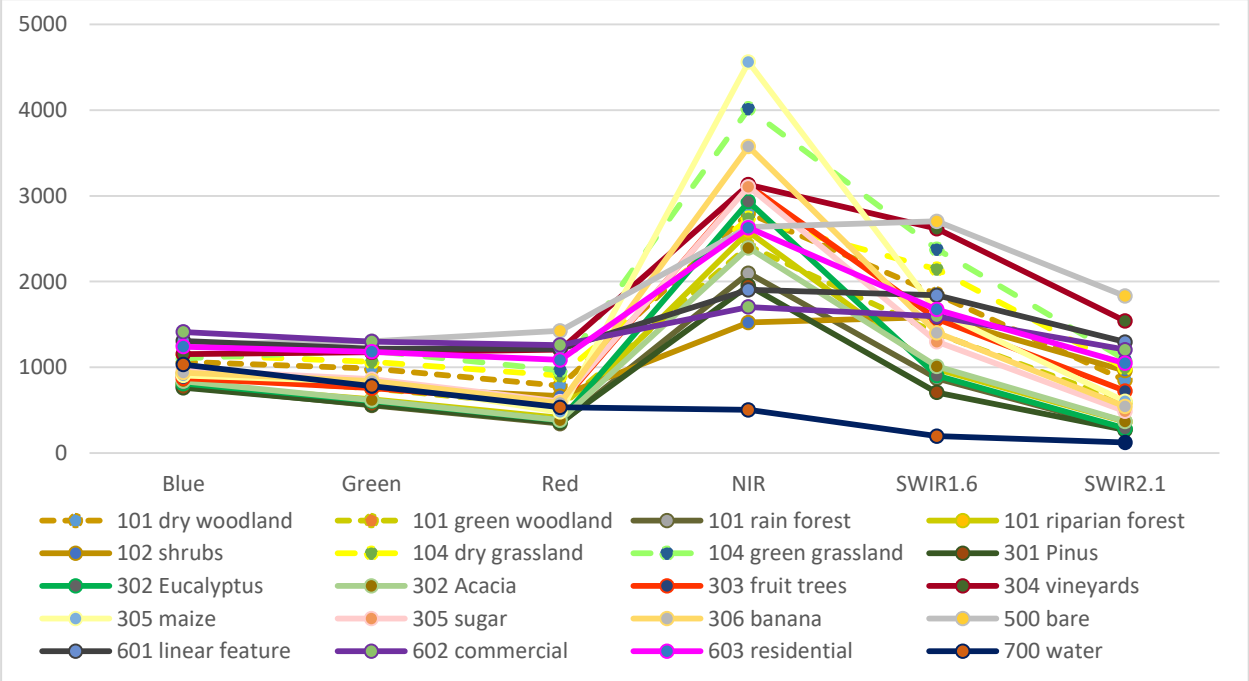

Figure 3-3 Spectral signatures illustrating the similarity between selected land cover classes across Landsat TM/ETM+ bands in TOA reflectance scaled to 10 000

Table 3-4 Mean and standard deviation values per spectral band and land cover class as measured in TOA reflectance scaled to 10 000

Class	Blue		Green		Red		NIR		SWIR1.6		SWIR2.1	
	MEAN	SD	MEAN	SD	MEAN	SD	MEAN	SD	MEAN	SD	MEAN	SD
101 dry woodland	1064	83	986	77	784	102	2797	174	1853	248	849	168
101 green woodland	902	47	754	80	543	87	2418	596	1396	206	592	119
101 rain forest	776	26	555	26	342	24	2099	223	871	149	280	63
101 riparian forest	801	26	627	48	410	45	2580	218	977	144	366	85
102 shrubs	929	95	767	108	663	130	1523	172	1586	313	961	260
104 dry grassland	1149	59	1064	51	903	58	2739	108	2144	123	991	106
104 green grassland	1104	58	1192	87	963	157	4016	520	2378	274	1090	216
301 *Pinus*	761	36	564	36	356	28	1953	260	707	108	268	57
302 *Eucalyptus*	809	33	608	42	380	42	2933	226	904	125	286	56
302 *Acacia*	838	42	616	46	384	51	2393	260	1011	136	370	77
303 fruit trees	872	70	757	87	580	111	3123	312	1563	262	724	181
304 vineyards	1155	111	1176	171	1208	241	3130	325	2616	348	1539	320
305 maize	904	57	829	37	479	39	4561	388	1656	78	602	32
305 sugar	970	86	863	114	600	118	3106	347	1300	127	487	82
306 banana	938	84	839	90	583	95	3574	286	1404	189	543	124
500 bare	1265	251	1305	403	1425	607	2637	508	2703	759	1831	816
601 linear feature	1308	97	1219	123	1216	170	1905	256	1839	292	1295	215
602 commercial	1412	304	1301	340	1260	372	1703	290	1596	360	1205	349
603 residential	1242	118	1182	143	1085	189	2628	291	1675	268	1047	210
700 water	1032	110	781	107	534	98	504	211	198	93	123	66

3.3.4.2 Spectral features and indices

Indices and linear combinations of bands allow for better discrimination between spectral classes. A tasselled cap transformation, as first published by Kauth & Thomas (1976) and parameterised for Landsat-7 reflectance data by Huang et al. (2002), transforms the spectral information of different bands into thematic principal components with predefined eigen vectors. This method condenses information captured in spectral bands with a linear transformation, so that over 95% of the image variability is accounted for by the first three components, which represent brightness, greenness, and wetness. Shadow has a proportionally higher value in the wetness component inverse to either greenness or brightness.

With the strong absorption of red light due to photosynthetic activity, and the strong reflection of near-infrared light in the moist palisade tissue of leaves, vegetation can easily be discriminated with the Red and NIR spectral bands. As denoted by Equation 3-1, taking the simple ratio (SR) (Jordan 1969) between these two bands provides an index for the identification of vegetation. These values may vary between 0 and infinity.

$$SR = \frac{\rho_{NIR}}{\rho_{RED}}$$ Equation 3-1

where SR is the simple ratio between NIR band and RED band;

ρ_{NIR} is the TOA reflectance of the NIR band; and

ρ_{RED} is the TOA reflectance of RED band.

The normalised difference vegetation index (NDVI) is commonly used to indicate the presence of actively growing vegetation (Asrar et al. 1984; Curran 1980; Tucker et al. 1981) and is denoted by Equation 3-2. Values can vary between -1 and +1, with a value below 0.2 normally being considered bare of vegetation.

$$NDVI = \frac{\rho_{NIR} - \rho_{RED}}{\rho_{NIR} + \rho_{RED}}$$ Equation 3-2

where $NDVI$ is the normalised difference vegetation index;

ρ_{NIR} is the TOA reflectance of the NIR band; and

ρ_{RED} is the TOA reflectance of the RED band.

The NDVI is known to be sensitive to high water vapour concentrations and red soil in areas with open plant canopies, which can result in lower than expected values. The NDVI is also known to saturate over dense vegetation, making it difficult to discriminate between different vegetation states in such areas. A range of indices have been developed to address the shortcomings of the NDVI by incorporating the short wave infrared and the blue bands.

The enhanced vegetation index (EVI) (Huete, Justice & Liu 1994; Hui Qing Liu & Huete 1995) was developed for MODIS (Vicente-Serrano, Pérez-Cabello & Lasanta 2008), a sensor whose first seven spectral bands are very similar to that of Landsat. The EVI is one of the most popular vegetation indices in forestry applications as it does not suffer from the shortcomings of the NDVI. The formula for the EVI is denoted by:

$$EVI = G \times \frac{\rho_{NIR} - \rho_{RED}}{\rho_{NIR} + C_1 \times \rho_{RED} - C_2 \times \rho_{BLUE} + L}$$ Equation 3-3

where EVI is the enhanced vegetation index;

ρ_{NIR} is the TOA reflectance of the NIR band;

ρ_{RED} is the TOA reflectance of the RED band;

ρ_{BLUE} is the TOA reflectance of the BLUE band;

C_1 is the aerosol resistance term 1 set to 6;

C_2 is the aerosol resistance term 2 set to 7.5;

G is a gain factor set to 2.5; and

L is the canopy background adjustment constant set to 1.

Discrimination between herbaceous and woody vegetation was an important objective of this study. A customised index that exploits the cumulative high reflectance of woody vegetation in the green and near-infrared bands and its low reflectance in the two shortwave infrared bands is denoted as follows:

$$ND42 \cdot 57 = \frac{\left(\rho_{NIR} + \rho_{GREEN}\right) - \left(\rho_{SWIR_{1.6}} + \rho_{SWIR_{2.1}}\right)}{\left(\rho_{NIR} + \rho_{GREEN}\right) + \left(\rho_{SWIR_{1.6}} + \rho_{SWIR_{2.1}}\right)}$$ Equation 3-4

where $ND42 \cdot 57$ is the normalised difference of NIR and GREEN band with $\boldsymbol{SWIR_{1.6}}$ and $\boldsymbol{SWIR_{2.1}}$;

ρ_{NIR} is the TOA reflectance of NIR band;

ρ_{GREEN} is the TOA reflectance of GREEN band;

$\rho_{SWIR_{1.6}}$ is the TOA reflectance of $\boldsymbol{SWIR_{1.6}}$ band; and

$\rho_{SWIR_{2.1}}$ is the TOA reflectance of $\boldsymbol{SWIR_{2.1}}$ band.

3.3.4.3 Temporal characteristics

Spectral signatures of vegetation change over time. These fluctuations are attributed to phenology and occur on a daily, seasonal, and lifetime cycle of the vegetation. In order to produce usable results, any automated SRC technique has to be tolerant of, or account for, such fluctuations. For this reason, the stability of spectral signatures of forest classes in the subtropics of Southern Africa had to be investigated in this study. Two-time series plots by major forestry class and study area were extracted and analysed using the Web EOM tool (http://www.earth-observation-monitor.net/map.php) developed by the Friedrich Schiller University of Jena using the Google Earth Engine-hosted MODIS Terra EVI – 250 m 16-Daily (MOD13Q1) dataset (Eberle et al. 2013). Figure 3-4 illustrates the relatively low EVI fluctuations of *Eucalyptus grandis* over its peak growth period between 2003 (plant date) and 2010 (harvest), whereas the deciduous savannah woodland displays strong fluctuations. Due to these strong fluctuations, the latter class cannot be reliably extracted automatically from a single date or single image composite. To address this challenge, vegetation classes portraying a strong seasonal phenological behaviour, such as woodland and grassland, were split into dry and green classes, as both vegetation states were present in the image composites to be classified. Spectral signature samples from cultivated classes were extracted only during the vegetative phase of the respective crop. The relative low phenologic variability (also referred to as pseudo invariant feature characterisation) of the evergreen plantations and afro-montane-rain forests makes it possible to characterise and identify these classes from a single image composite.

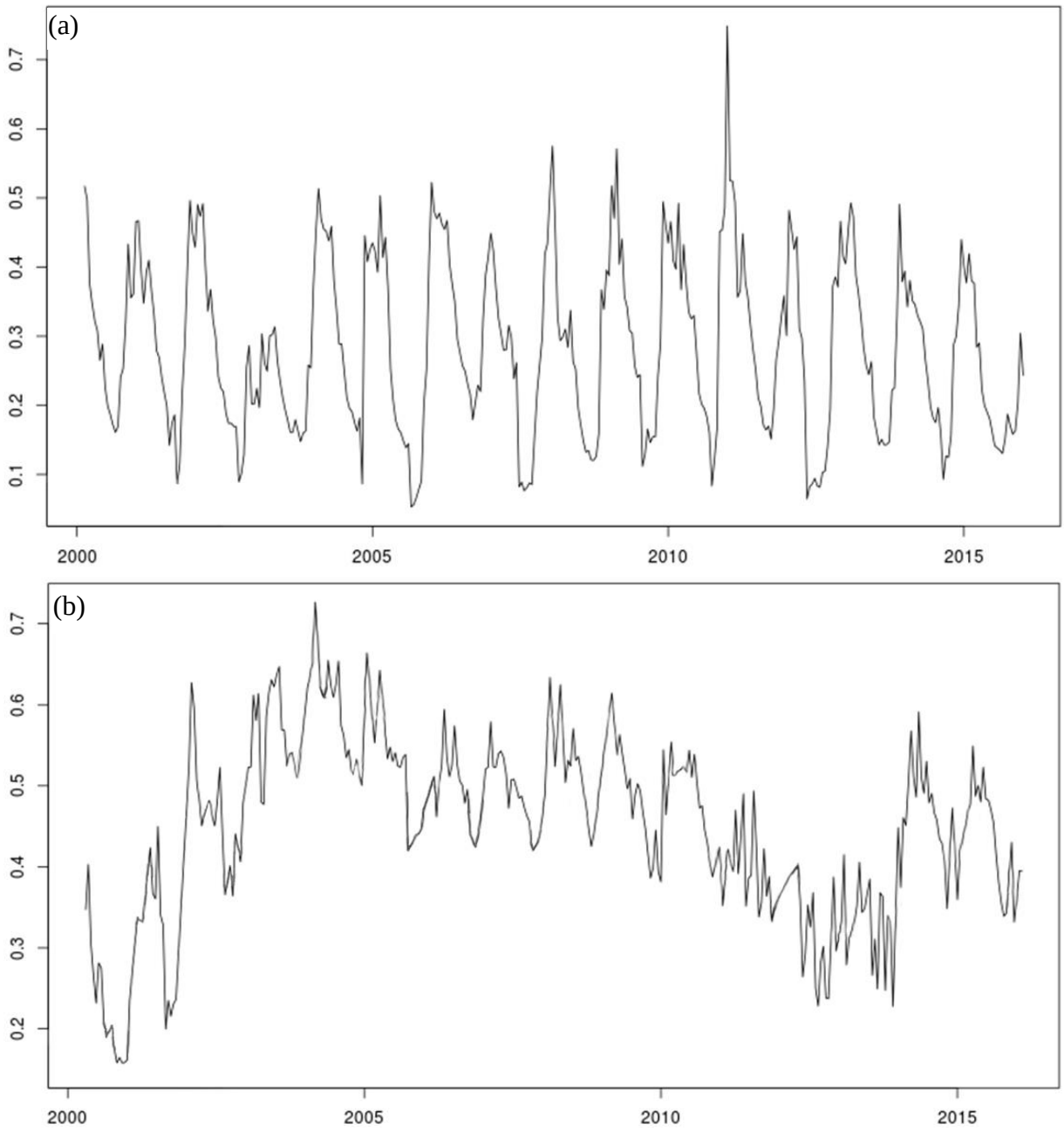

Figure 3-4 Time series of MOD13Q1 EVI (y) in years AD (x) for (a) a deciduous savannah woodland versus that of (b) an *Eucalyptus grandis* plantation with an eight-year rotation

3.3.5 Classification

Most large-scale forest classifications were undertaken using semi-automated techniques that still require operators to select forestry areas, from which statistics of the spectral properties could be derived (Wulder et al. 2008; Lewinski 2005; Potapov et al. 2008; Potapov 2012). Such semi-automated approaches should be fully automatable, provided that input imagery is properly normalised and classes do not show significant spectral variability over time. To test this hypothesis, two classification approaches were considered. In the first approach, two generic rule-based classifiers, namely SRC (Baraldi et al. 2006) and SPECL (Richter 2011a), were selected as neither requires any prior knowledge of classes to be extracted. A new set of

classification rules, inspired by Lewinski & Bochenek (2008), who created a similar ruleset in e-Cognition software, were developed for these classifiers. These rulesets were implemented in the rule-based engine (RBE), a function of PCI Geomatica 2017, as part of the OSRBC. The second classification approach was to develop machine learning models based on a set of samples collected in one area, and to then apply the models to a different area (i.e. perform signature extension). SVM and RF were used for the model building. The following subsections discuss each classification approach separately.

3.3.5.1 Geographic object-based image analysis

The concepts of GEOBIA were pioneered by a company called Definiens, who developed the eCognition software (now belonging to Trimble) in 1999 (Benz et al. 2004). Since then, image segmentation and feature extraction have been implemented in other software packages. In this study, the object analyst (OA) tool of PCI Geomatica 2017 was used. The radiometrically normalised Landsat TM/ETM+ composites were segmented using the region growing segmentation algorithm, with bands 3, 4, and 5 (Red, NIR, SWIR1.6) as input. A scale of 25 and weighting of 0.5 for both “shape” and “compactness” was applied. The original image and resulting segments are shown in Figure 3-5. All classifications for this study were based on image segments generated with this method.

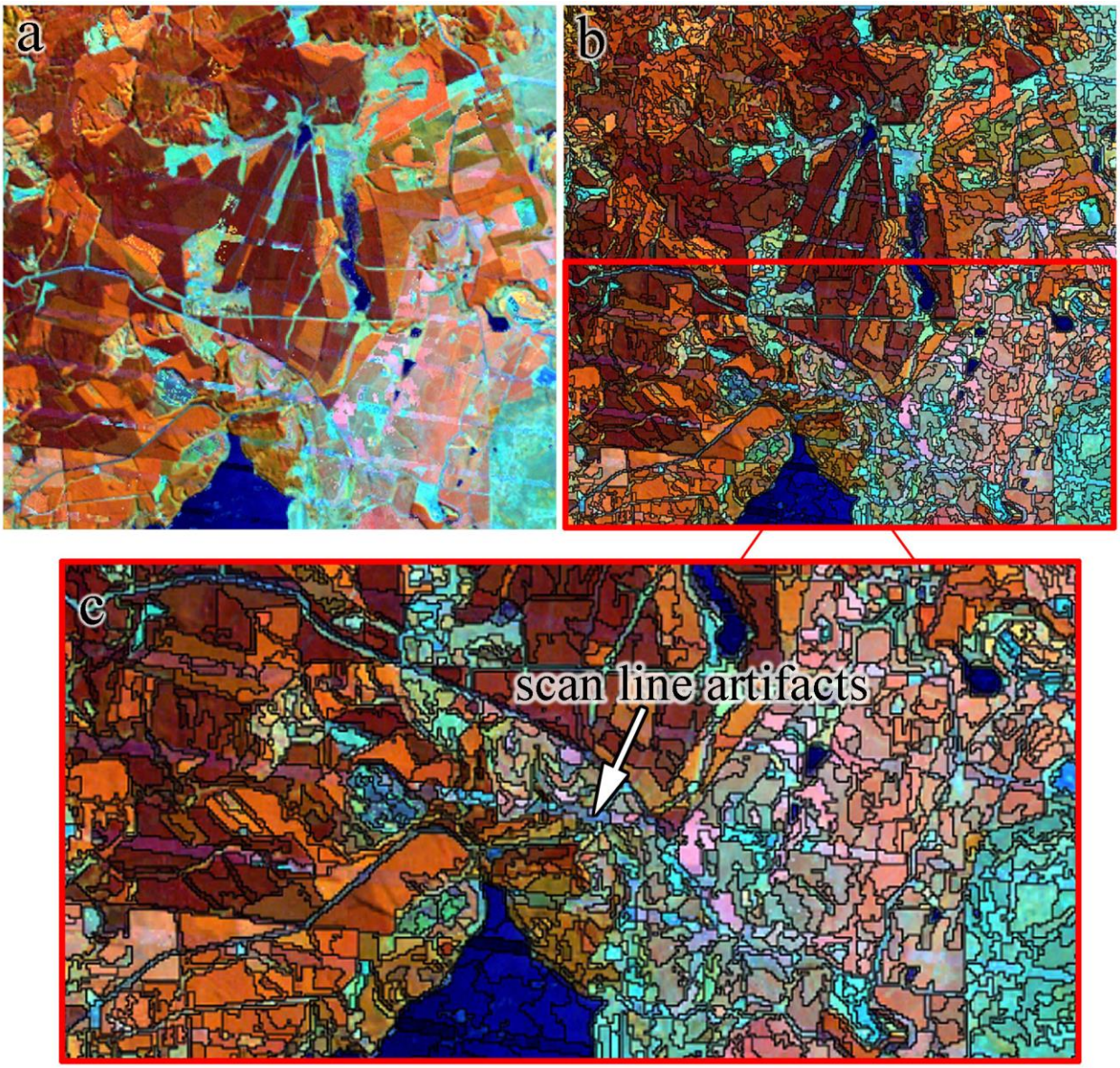

Figure 3-5 Landsat TM/ETM+ composite, 453 band combination, subset over the Natal Midlands study area: (a) unsegmented, and (b) segmented image, with an expanded view (c) showing the segmentation and scan line artefacts resulting from the ETM+ SLC failure. The segmentation was done using a scale of 25 and shape/compactness parameters of 0.5 determined experimentally.

Object features were calculated for all bands except the thermal band. The minimum, maximum, mean, and standard deviation of pixel values within each object were calculated. In addition, the area, compactness, circularity, perimeter, elongation, and rectangularity of each object were quantified. Some of the resulting image objects were manually selected as representative samples per class by overlaying polygons captured during field work for the three study sites. To avoid feature contamination, special care was taken not to select objects that have undergone a class change (i.e. due to harvest, fire, disease, etc.). The mean spectral value of each band was extracted for each object and these were used in the SRCs.

3.3.5.2 JRC SRC

The JRC SRC (Baraldi et al. 2006) was applied using mean spectral values per band from each object. All forest objects were isolated with the vegetation spectral rule, and further subdivisions were made by applying *medium* and *high* thresholds to NDVI and NIR reflectance values, as illustrated in Figure 3-6. In Baraldi et al. (2006), threshold values for *low*, *medium*, and *high* are provided as unit-less values and could, therefore, not be translated to this study. Consequently, new thresholds to maximise forest class separability were defined using the normalised difference bare soil index shown in Equation 3-5. The section of the relevant EASI code is shown in Appendix II. Variables MIR1 and MIR2 represent the SWIR1.6 and SWIR2.1 band values respectively. Threshold values of 0.63 and 0.56 were used in the first step to discriminate between *high*, *medium*, and *low* NDVI, while thresholds of 0.23 (NIR), 0.11 (SWIR1.6), and 0.05 (SWIR2.1) were used in the second step to separate *low* and *high* categories. All thresholds were determined experimentally.

$$NDBSI = \frac{\rho_{SWIR_{1.6}} - \rho_{NIR}}{\rho_{SWIR_{1.6}} + \rho_{NIR}} \qquad \text{Equation 3-5}$$

Where $NDBSI$ is the normalised difference bare soil index (Baraldi et al. 2006);

ρ_{NIR} is the TOA reflectance of NIR band; and

$\rho_{SWIR_{1.6}}$ is the TOA reflectance of SWIR1.6 band.

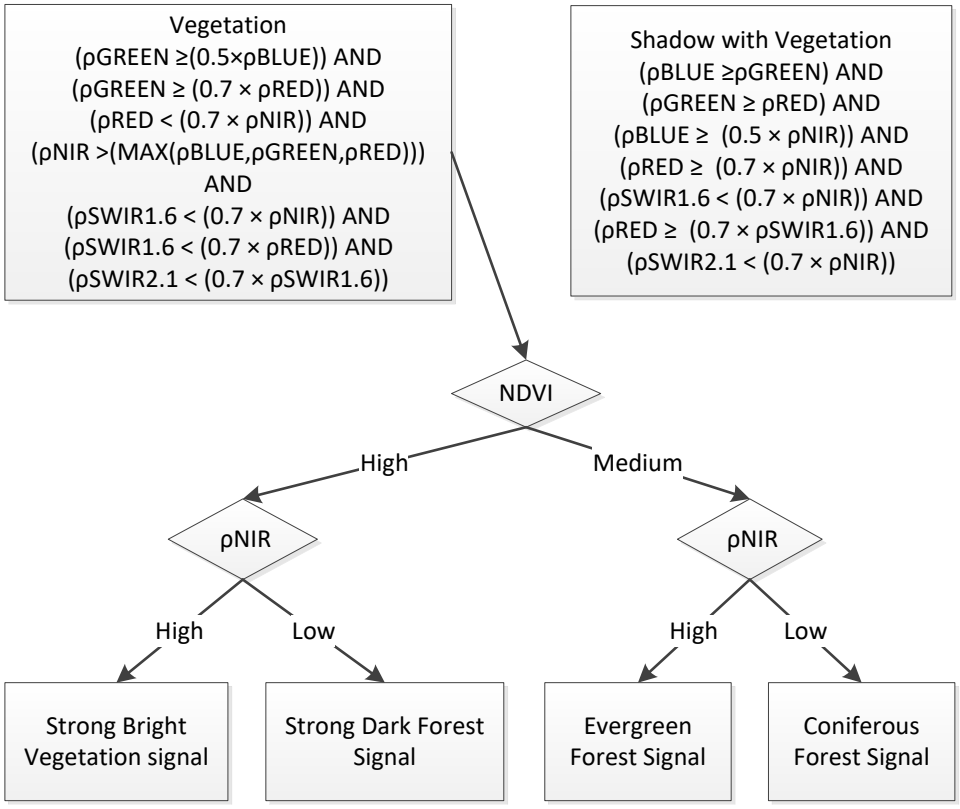

Figure 3-6 SRC adapted from Baraldi et al. (2006) for classes associated with forests and strong bright vegetation

The Table 3-5 provides a key between class codes and descriptive names associated with these codes.

Table 3-5 Codes for classes of the JRC SRC

Code	Descriptive name
V_SR	Vegetation Spectral Rule
SVHNIR_LSC	Strong Vegetation High NIR Leaf Spectral Category
SVLNIR_LSC	Strong Vegetation Low NIR Leaf Spectral Category
AVLNIR_LSC	Average Vegetation Low NIR Leaf Spectral Category
AVHNIR_LSC	Average Vegetation High NIR Leaf Spectral Category
DR_LSC	Dark Rangeland Leaf Spectral Category
R_SR	Rangeland Spectral Rule
TKCL_SR	Thick Cloud Spectral Rule
TNCL_SR	Thin Cloud Spectral Rule
BBC_SR	Barren Land or Build Up or Clouds Spectral Rule
DB_SR	Dominant Blue Spectral Rule
WASH_SR	Water or Shadow Spectral Rule

3.3.5.3 SPECL

SPECL (Richter 2011b: 161) isolates 17 broad spectral classes, characterised by unique spectral response curves, by applying a rule-based classification. Figure 3-7 shows the spectral response curves of the seven classes that relate to vegetation. Although none of these vegetation classes explicitly represents forests, it was determined from visual assessments that the dark vegetation class mostly represents dark coniferous forests. The classifier identifies classes by applying simple reflectance thresholds to each band, as illustrated in Table 3-6. Variables *b1* to *b7* represent the Landsat TM/ETM+ bands 1–7 respectively and were not substituted with common names for the sake of consistency with the original SPECL documentation and to enable shorter query strings.

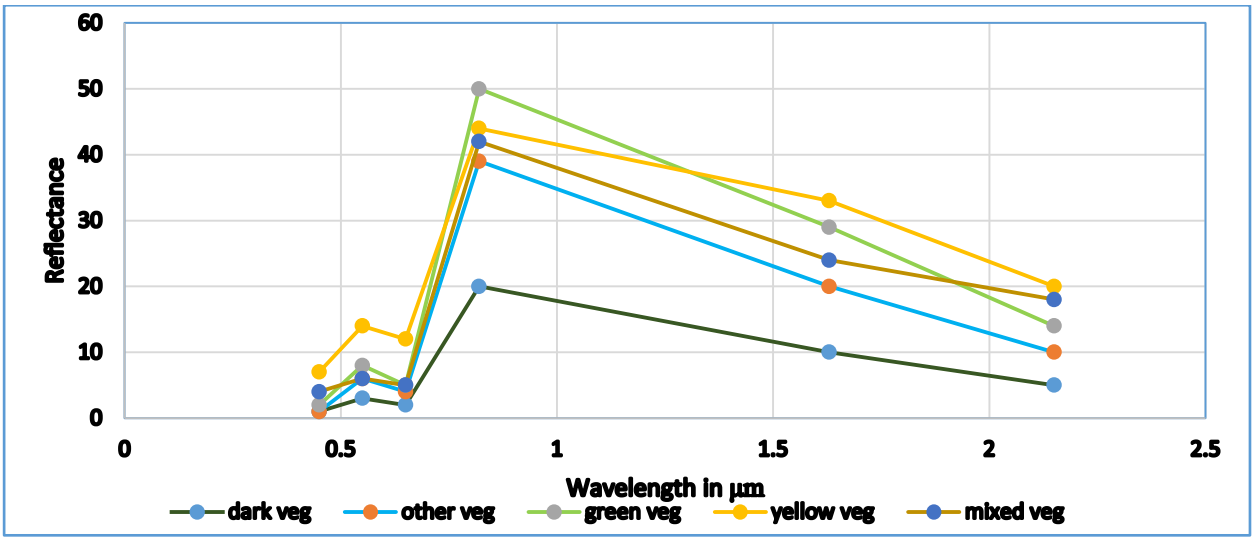

Figure 3-7 Spectral signatures of SPECL vegetation classes (Richter 2011b: 161)

Table 3-6 Set of spectral rules used in SPECL

Class	Spectral Rule
Snow	b4/b3 ≤ 1.3 and b3 ≥ 0.2 and b5 ≤ 0.12
Cloud	b4 ≥ 0.25 and 0.85 ≤ b1/b4 ≤ 1.15 and b4/b5 ≥ 0.9 and b5 ≥ 0.2
Dark bare soil	b4 ≥ 0.15 and 1.3 ≤ b4/b3 ≤ 3.0 and b2 ≤ 0.10
Bright bare soil	b4 ≥ 0.15 and 1.3 ≤ b4/b3 ≤ 3.0
Average vegetation	b4/b3 ≥ 3.0 and (b2/b3 ≥ 0.8 or b3 ≤ 0.15) and 0.28 ≤ b4 ≤ 0.45
Bright vegetation	b4/b3 ≥ 3.0 and (b2/b3 ≥ 0.8 or b3 ≤ 0.15) and b4 ≥ 0.45
Dark vegetation	b4/b3 ≥ 3.0 and (b2/b3 ≥ 0.8 or b3 ≤ 0.15) and b3 ≤ 0.08 and b4 ≤ 0.28
Yellow vegetation	b4/b3 ≥ 2.0 and b2 ≥ b3 and b3 ≥ 0.08 and b4/b5 ≥ 1.5
Mix veg/soil	2.0 ≤ b4/b3 ≤ 3.0 and 0.05 ≤ b3 ≤ 0.15 and b4 ≥ 0.15
Asphalt/dark sand	b4/b3 ≤ 1.6 and 0.05 ≤ b3 ≤ 0.20 and 0.05 ≤ b4 ≤ 0.20 and 0.05 ≤ b5 ≤ 0.25 and b5/b4 ≥ 0.7
Sand/bare soil/cloud	b4/b3 ≤ 2.0 and b4 ≥ 0.15 and b5 ≥ 0.15
Bright sand/bare soil/cloud	b4/b3 ≤ 2.0 and b4 ≥ 0.15 and (b4 ≥ 0.25 or b5 ≥ 0.30)
Dry vegetation/soil	(1.7 ≤ b4/b3 ≤ 2.0 and b4 ≥ 0.25) or (1.4 ≤ b4/b3 ≤ 2.0 and b7/b5 ≤ 0.83)
Sparse vegetation/soil	(1.4 ≤ b4/b3 ≤ 1.7 and b4 ≥ 0.25) or (1.4 ≤ b4/b3 ≤ 2.0 and b7/b5 ≤ 0.83 and b5/b4 ≥ 1.2)
Clear water over sand	b3 ≥ 0.02 and b3 ≥ b4+0.005 and b5 ≤ 0.02
Clear water	b4 ≤ 0.02 and b5 ≤ 0.02
Turbid water	b4 ≤ 0.11 and b5 ≤ 0.05

Adopted from Richter Schlapher (2014)

SPECL is iterative and based on the systematic elimination of each class until an appropriate one is identified (based on the threshold values compared against the extracted values of each object). For this reason, all classes (including non-vegetation ones) must be included and assessed in the proper order during analysis.

3.3.5.4 Optimised spectral rule base

In order to assess the performance of the OSRBC with the desired classes, samples were extracted from the dataset and analysed. Only the mean spectral and spectral feature values (i.e. texture, topological relations, and indices) for each object were used for this analysis. It was assumed that feature values have normal distributions and are suitable for discriminant analysis. Within each class, the arithmetic mean ($\overline{x}$ in Equation 3-6) and standard deviation (σ in Equation 3-7) were calculated for each feature. These measures were normalised by feature across all classes so that values from different features could be compared directly with one another. Linear scaling of the mean values to a range of 0 to 1 was done by extracting the minimum and maximum values of each feature. The minimum value was subtracted from each value, and the remainder was divided by the difference between the maximum and minimum values (Equation 3-8). The standard deviation was normalised in a similar manner using the difference between the maximum and minimum mean values as denominator (Equation 3-9). The weighted distance between normalised mean values of classes, weighted by the sum of their normalised standard deviation, was then calculated per feature. This enabled the calculation of absolute feature distance, or hyperplane (Δ), expressed in standard deviations between two

classes with values distributed normally, and resulted in an equal value for the consumer and producer accuracy at the given hyperplane. Equations derived from Sokal & Rohlf (1995).

$$\overline{x} = \frac{x_1 + x_2 + x_3 + \cdots + x_n}{n} \quad \text{Equation 3-6}$$

$$\sigma = \sqrt{\frac{1}{n-1}\sum_{i=1}^{n}(x_i - \overline{x})^2} \quad \text{Equation 3-7}$$

$$X' = \frac{X - X_{min}}{X_{max} - X_{min}} \quad \text{Equation 3-8}$$

$$\sigma' = \frac{\sigma}{X_{max} - X_{min}} \quad \text{Equation 3-9}$$

$$\Delta = \frac{X'_{class1} - X'_{class2}}{\sigma'_{class1} + \sigma'_{class2}} \quad \text{Equation 3-10}$$

Assuming a normal distribution of values by feature and class, a distance (Δ) of one indicates that the hyperplane is separated by one standard deviation between the mean feature value of two classes, which implies that 16% of all cases (samples) will likely be misclassified. A distance of two implies an error of 2.2%, and a distance of three implies an error of 0.1%. Consequently, the maximum distance across all features between two classes was calculated to assess whether classes can be reliably separated. The maximum distance between any two classes for a given feature was also calculated to determine the feature that provides the highest level of discrimination across all classes.

3.3.5.5 Random forest (RF)

An RF classification was performed using the statistical analysis package R. Samples for a given experiment defined in the training column of the matrix were split randomly into an algorithm training (predictor) set and accuracy assessment (validation) set. The RF was trained using the "predictor" samples, and the resulting model was then used to classify the complete dataset. This classification was independently performed for each study area by using samples collected over its area. To assess the transferability of samples between areas, a second classification was performed on each area using samples from the other two study areas to train the RF model.

3.3.5.6 Support vector machine

The SVM classifier as implemented using the OA tool of PCI Geomatica 2017. Internally optimised parameter settings and the RBF kernel were applied. The same classification permutations (with respect to study areas and samples) that were applied to the RF classification were carried out for the SVM classifications.

3.3.6 Accuracy assessment

The only measure of performance that could be applied to the two generic (versus forest specific) rule-based classifications was a mapping of spectral rule-based classes to the sampled land cover classes. A simple matrix comparing occurrence frequency was generated for this evaluation. The accuracy of RF, OSRBC, and SVM was assessed using the *Accuracy Assessment* option of the PCI Geomatica 2017 OA tool. This produced a confusion matrix with the *producer accuracy* (Equation 3-11) and *user accuracy* (Equation 3-12), and accuracy statistics with the kappa value (K) (Equation 3-14) calculated from the expected frequency by chance that a class would occur (*ef*) (Equation 3-13).

$$producer\ accuracy = \frac{\sum correct\ allocation\ to\ class}{\sum validation\ samples\ of\ class}\ x\ 100 \qquad \text{Equation 3-11}$$

$$user\ accuracy = \frac{\sum correct\ allocation\ to\ class}{\sum allocations\ to\ class}\ x\ 100 \qquad \text{Equation 3-12}$$

$$ef = \frac{\sum samples\ in\ class\ \ x\ \sum allocations\ to\ class}{\sum samples\ in\ all\ classes} \qquad \text{Equation 3-13}$$

$$K = \frac{\sum correct\ classifications - \sum ef}{\sum samples\ in\ all\ classes - \sum ef} \qquad \text{Equation 3-14}$$

3.4 RESULTS

Figure 3-8 compares a Landsat TM image to the associated product after topographic correction and compositing were applied as described in Lück & Van Niekerk (2016). Different forest classes are more distinguishable in the corrected image, and within-class variability is substantially reduced. Some artefacts, such as fringes of cloud shadow or boundaries between Landsat-7 ETM+ scan lines (Figure 3.5 (c)), are, however, noticeable in the composite. These artefacts are mainly attributed to temporal variations (especially over vegetation with a strong seasonal spectral variation) as imagery collected over a year was used to generate the composite

(listed in Appendix I). Atmospheric conditions also varied between image acquisitions, which most strongly affected shorter wavelengths.

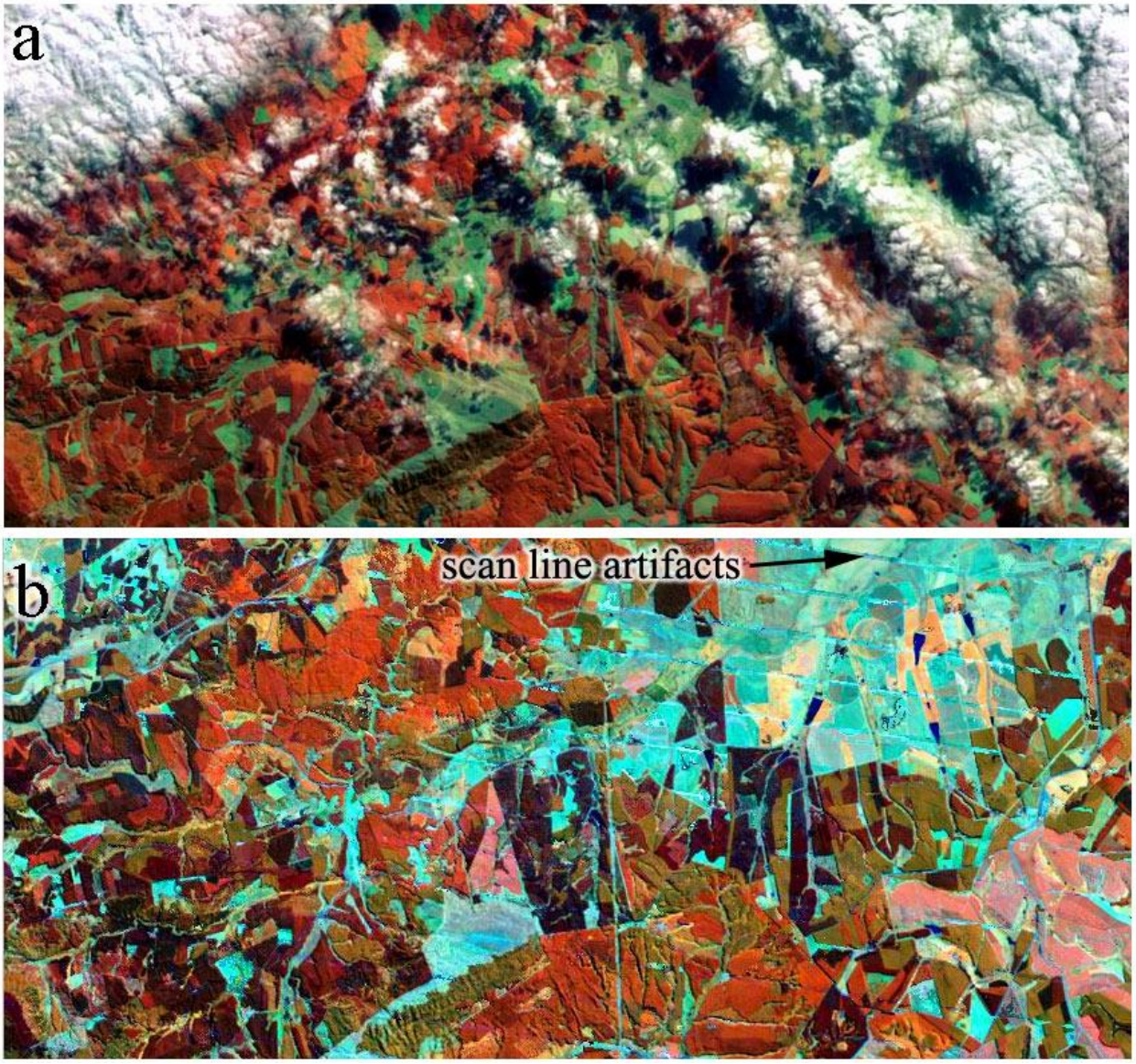

Figure 3-8 Landsat 5 TM, 453 band composite acquired over Natal Midlands on (a) 28 May 2009 and (b) topographically normalised and multi-image TM/ETM+ composite

The class mapping of the SRC results is shown in Table 3-7. The majority of *302 Eucalyptus* (99%) and *101 riparian forests* (86%) samples were associated with spectral class *SVHNIR_LSC*, whereas *301 Pinus* (78%) and *101 rain forests* (70%) are strongly related to *SVLNIR_LSC*. Cells shaded in red indicate no match between the SRC class and land cover class, while poor matches are shaded yellow and italicised, and good matches are shaded green and written in bold, and almost exact matches are further underlined. The last column of the table provides the total number of samples from all three sites used for the comparison.

Table 3-7 Class mapping of the SRC classification (horizontal) and land cover classes (vertical) expressed as percentage of samples occurring in the respective classes

	V_SR	SVHNIR_LSC	SVLNIR_LSC	AVLNIR_LSC	AVHNIR_LSC	DR_LSC	R_SR	TKCL_SR	TNCL_SR	BBC_SR	DB_SR	WASH_SR	TOTAL
101 dry woodland	22%	0%	0%	0%	0%	0%	39%	39%	0%	0%	0%	0%	92
101 green woodland	76%	2%	0%	0%	0%	0%	14%	8%	0%	0%	0%	0%	59
101 rain forest	10%	20%	70%	0%	0%	0%	0%	0%	0%	0%	0%	0%	20
101 riparian forest	7%	86%	7%	0%	0%	0%	0%	0%	0%	0%	0%	0%	28
102 shrubs	0%	0%	0%	0%	0%	0%	95%	0%	0%	0%	5%	0%	39
104 dry grassland	0%	0%	0%	0%	0%	0%	96%	4%	0%	0%	0%	0%	57
104 green grassland	8%	0%	0%	0%	0%	0%	12%	80%	0%	0%	0%	0%	25
301 *Pinus*	11%	9%	78%	1%	0%	1%	0%	0%	0%	0%	0%	0%	169
302 *Acacia*	29%	50%	21%	0%	0%	0%	0%	0%	0%	0%	0%	0%	14
302 *Eucalyptus*	1%	99%	0%	0%	0%	0%	0%	0%	0%	0%	0%	0%	93
303 fruit trees	65%	6%	0%	0%	2%	0%	4%	24%	0%	0%	0%	0%	54
304 vineyards	0%	0%	0%	0%	0%	0%	92%	8%	0%	0%	0%	0%	61
305 maize	100%	0%	0%	0%	0%	0%	0%	0%	0%	0%	0%	0%	12
305 sugar	72%	19%	0%	0%	0%	0%	0%	8%	0%	0%	0%	0%	36
306 banana	80%	13%	0%	0%	0%	0%	0%	7%	0%	0%	0%	0%	15
500 bare	0%	0%	0%	0%	0%	0%	57%	0%	0%	43%	0%	0%	96
601 linear feature	0%	0%	0%	0%	0%	0%	48%	0%	28%	10%	14%	0%	29
602 commercial	0%	0%	0%	0%	0%	0%	27%	0%	51%	0%	21%	1%	89
603 residential	5%	0%	0%	0%	0%	0%	22%	74%	0%	0%	0%	0%	87
700 water	0%	0%	0%	0%	0%	0%	0%	0%	0%	0%	29%	71%	87
TOTAL	16%	13%	13%	0%	0%	0%	27%	13%	5%	4%	4%	5%	1162

In the SPECL classification (

Table 3-8), *101 riparian forest*, *101 rain forest*, *301 Pinus*, and *302 Acacia* are all strongly associated with the *dark vegetation* SPECL class, whereas *302 Eucalyptus*, *303 fruit trees*, *305 sugar*, and *306 banana* are all grouped with the *average vegetation* class.

Table 3-8 Class mapping of the SPECL classification (horizontal) and land cover classes (vertical) expressed as percentage occurring in the respective classes

	cloud	dark bare soil	bright bare soil	average vegetation	bright vegetation	dark vegetation	yellow vegetation	mix vegetation / soil	asphalt / dark sand	sand / bare soil / cloud	bright sand / bare soil/cloud	dry vegetation / soil	clear water	turbid water	Total
101 riparian forest	0%	0%	0%	21%	0%	79%	0%	0%	0%	0%	0%	0%	0%	0%	28
101 green woodland	0%	2%	0%	34%	0%	64%	0%	0%	0%	0%	0%	0%	0%	0%	59
101 rain forest	0%	0%	0%	0%	0%	100%	0%	0%	0%	0%	0%	0%	0%	0%	20
101 dry woodland	0%	0%	8%	10%	11%	12%	13%	14%	15%	17%	0%	0%	0%	0%	84
102 shrubs	0%	72%	8%	5%	0%	13%	0%	0%	3%	0%	0%	0%	0%	0%	39
104 green grassland	0%	0%	8%	64%	28%	0%	0%	0%	0%	0%	0%	0%	0%	0%	25
104 dry grassland	0%	0%	40%	23%	0%	2%	0%	0%	0%	35%	0%	0%	0%	0%	57
301 *Pinus*	0%	0%	0%	0%	0%	100%	0%	0%	0%	0%	0%	0%	0%	0%	169
302 *Eucalyptus*	0%	0%	0%	72%	0%	28%	0%	0%	0%	0%	0%	0%	0%	0%	93
302 *Acacia*	0%	0%	0%	7%	0%	93%	0%	0%	0%	0%	0%	0%	0%	0%	14
303 fruit trees	0%	0%	0%	85%	0%	15%	0%	0%	0%	0%	0%	0%	0%	0%	54
304 vineyards	0%	7%	75%	16%	0%	0%	0%	0%	0%	2%	0%	0%	0%	0%	61
305 maize	0%	0%	0%	42%	58%	0%	0%	0%	0%	0%	0%	0%	0%	0%	12
305 sugar	0%	0%	0%	83%	0%	17%	0%	0%	0%	0%	0%	0%	0%	0%	36
306 banana	0%	0%	0%	100%	0%	0%	0%	0%	0%	0%	0%	0%	0%	0%	15
500 bare	0%	23%	60%	2%	0%	4%	0%	0%	0%	2%	9%	0%	0%	0%	97
601 linear feature	0%	0%	86%	0%	0%	0%	0%	0%	14%	0%	0%	0%	0%	0%	29
602 commercial	1%	25%	13%	0%	0%	0%	0%	0%	58%	0%	0%	2%	0%	0%	89
603 residential	0%	4%	84%	4%	0%	2%	4%	0%	0%	0%	0%	0%	0%	0%	89
700 water	0%	0%	0%	0%	0%	1%	0%	0%	0%	0%	0%	13%	34%	52%	87
TOTAL	0%	7%	22%	21%	2%	28%	1%	1%	6%	3%	1%	1%	3%	4%	1157

Table 3.9 shows a pairwise comparison of class separability (below the diagonal) and the spectral features (above the diagonal) that produced the strongest differentiation in each case. Most classes have separability values of greater than one, which indicates that classification errors of less than 16% are likely. However, several classes are poorly separated from one another. For instance, the *601 linear feature* and *602 commercial* combination has a separability of only 0.46, which means that the likelihood of an error of more than 50% is high. Similarly, the forest classes *301 Pinus–101 rain forest* have a separability score of 0.64, while *302 Acacia–101 riparian forest* has a score of 0.54. The *302 Acacia–101 rain forest* has a slightly stronger separability of 0.85, but is still unlikely to produce a classification accuracy of more than 50%.

Looking at the inability to separate these classes using mean spectral values alone emphasises the strength of a GEOBIA classification using texture (standard deviation within an object) and a form factor. The class *101 rain forest* shows a much higher within-object standard deviation than *301 Pinus*, making it easy to differentiate between these two classes. Similarly, *101 riparian forest* can be distinguished from 302 *Acacia* by looking at the compactness of the objects, as they

tend to be elongated for *101 riparian forests* compared to the compacter commercial forestry compartment blocks of *302 Acacia*.

Table 3-9 Maximum class separability (below diagonal) and feature used (above diagonal)

Class name	101 dry woodland	101 green woodland	101 rain forest	101 riparian forest	102 shrubs	104 dry grassland	104 green grassland	301 pines	302 acacia	302 Eucalyptus	303 fruit trees	304 vineyards	305 maize	305 sugar	306 banana	500 bare	601 linear feature	602 commercial	603 residential	700 water
101 dry woodland		B1	B10	B2	B7	B4	B6	B12	B2	B10	B1	B8	B9	B4	B7	B11	B10	B7	B2	B3
101 green woodland	1.40		B2	B8	B11	B5	B6	B5	B8	B5	B3	B2	B7	B12	B11	B9	B7	B10	B0	B4
101 rain forest	2.91	1.80		B6	B8	B12	B8	B4	B1	B3	B5	B3	B8	B2	B7	B0	B4	B0	B12	B11
101 riparian forest	2.54	1.24	1.12		B5	B12	B3	B3	B0	B11	B6	B12	B4	B6	B1	B5	B4	B2	B10	B9
102 shrubs	2.01	1.90	3.08	1.94		B7	B7	B12	B9	B8	B12	B3	B6	B3	B10	B6	B0	B9	B1	B4
104 dry grassland	0.79	1.77	2.14	3.38	2.01		B6	B12	B12	B0	B9	B5	B2	B9	B10	B11	B2	B7	B8	B3
104 green grassland	2.24	2.24	3.08	1.71	2.56	2.24		B12	B0	B8	B6	B11	B1	B5	B4	B12	B7	B10	B3	B9
301 *Pinus*	3.47	1.84	0.64	1.31	3.47	3.38	3.38		B8	B6	B5	B12	B1	B0	B2	B5	B1	B2	B10	B7
302 *Acacia*	2.54	1.24	0.85	0.54	3.90	3.38	2.65	1.03		B7	B6	B12	B4	B1	B1	B5	B4	B2	B10	B11
302 *Eucalyptus*	2.91	1.84	1.85	1.01	3.08	3.66	3.08	1.93	1.24		B5	B1	B8	B4	B6	B5	B1	B2	B8	B9
303 fruit trees	1.40	0.78	1.85	1.47	1.63	2.07	2.24	1.84	1.47	1.85		B9	B3	B8	B12	B10	B12	B12	B0	B11
304 vineyards	1.39	2.03	1.85	3.38	3.23	1.29	1.36	3.38	3.38	2.67	2.07		B3	B9	B10	B7	B9	B11	B4	B6
305 maize	2.92	2.21	3.08	3.00	1.28	4.37	2.94	4.13	3.00	3.08	2.05	2.05		B6	B11	B3	B1	B7	B12	B9
305 sugar	1.48	1.13	1.80	1.47	3.23	2.07	1.92	1.71	1.54	1.58	1.03	2.07	1.91		B3	B10	B0	B5	B5	B11
306 banana	1.75	1.24	1.75	1.53	2.35	2.35	2.11	2.26	1.53	1.86	0.87	2.35	1.72	0.74		B8	B5	B2	B9	B10
500 bare	1.35	1.45	1.77	1.94	1.28	1.35	1.43	1.84	1.94	1.84	1.97	0.79	2.05	1.97	1.54		B3	B4	B12	B5
601 linear feature	2.53	2.56	3.00	3.00	1.97	1.37	2.56	4.13	3.00	2.67	1.63	1.71	2.67	1.97	2.22	0.96		B8	B11	B6
602 commercial	2.01	1.93	1.77	2.26	1.32	2.01	1.93	2.26	2.26	2.26	1.63	1.83	2.01	1.92	2.26	0.99	0.46		B3	B8
603 residential	1.03	1.97	2.14	2.71	1.65	0.96	1.71	2.71	2.71	3.08	1.97	1.53	2.14	1.92	2.32	1.43	1.44	1.59		B6
700 water	5.94	3.42	4.76	4.08	3.42	5.94	4.08	4.24	4.76	4.08	4.76	4.27	2.92	4.76	2.35	1.94	4.27	3.24	4.27	

Note: Colours illustrate poor (red) to good (green) seperability; B Note: Colours illustrate poor (red) to good (green) seperability; B0 to B12 represent Blue, Green, Red, NIR, SWIR1.6, SWIR2.1, Brightness, Greeness, Wetness, NDVI, SR, EVI & ND24_57 respectively

Lower and upper boundary threshold tables were populated using the mean and standard deviation values per feature and class, as illustrated in Table 3-10 and Table 3-11 respectively.

Table 3-10 Lower boundary separation thresholds providing maximum separability

Class name	B0	B1	B2	B3	B4	B5	B6	B7	B8	B9	B10	B11	B12
101 dry woodland		879	525	1761	1487			114	-1475		2236	4375	
101 green woodland			386		515	390		52		5265	2384	2961	
101 rain forest					776				-574		5265	3189	1806
101 riparian forest				2293			2569		-568	5837	3948		2278
102 shrubs					515	251				3342			
104 dry grassland	932		651	1761	2048	803		114				4375	
104 green grassland	950	937		3127	1801	645	3983	52		5837	2384	4907	797
301 *Pinus*								-60	-308		3948		2278
302 *Acacia*	815	577							-568	5825	3948	3189	1946
302 *Eucalyptus*				2513			2608	1090	-171	5837	5265	6487	
303 fruit trees				2881		372	3040			5702	3362	3189	658
304 vineyards		720	719	2513	2085	1128	2280	171		3439		3053	
305 maize		711		3763	1421		2905	176		4003		8557	3218
305 sugar	822	688	386	2080	1100		3040		-668	5657	3362	3189	3260
306 banana		687	418	3362			3323	1000	-910	6099	3626	6635	3446
500 bare	821			2150	1952	390	2905						
601 linear feature	1117	927	982		1411	817	2280						
602 commercial	821		512			645			-1134				
603 residential	1010	945	890	2165		645	2280		-1241			2708	797
700 water									24				

Note: Values are scaled by 10 000; B0 to B12 represent Blue, Green, Red, NIR, SWIR1.6, SWIR2.1, Brightness, Greenness, Wetness, NDVI, SR, EVI & ND24_57 respectively

Table 3-11 Upper boundary separation thresholds providing maximum separability

Class name	B0	B1	B2	B3	B4	B5	B6	B7	B8	B9	B10	B11	B12
101 dry woodland			890		2048		3983	1000		7292	5265		1889
101 green woodland	1010	879	719	2881		803	3983	1509	-568			6635	3260
101 rain forest	821	577	386	2513	1411	390	2569	1000					
101 riparian forest	815	701	512	3127	1411	251	3040					6487	
102 shrubs	1117	945		2080			2905	114	-171	5825	3626	2961	658
104 dry grassland			982			1128	3983		-1241	5657	3626		1806
104 green grassland									-574				1946
301 *Pinus*	822	711	418	2293	776	372	2608						
302 *Acacia*	950	687	500		1421	251	3040	1090	-308				
302 *Eucalyptus*	932	720	512		1100	390	3323						
303 fruit trees	1010	879		3763			3983		-668				3446
304 vineyards				3763					-1475	5702	3626	4907	1946
305 maize		927	651						-603				
305 sugar	1117			3362	1487	645	3993						
306 banana			512		1801	817						8557	
500 bare				3763				171	-910	5265	3362	4375	797
601 linear feature				2150				52	-1134	3439	2236	2708	1403
602 commercial				2165	1952			176	24	3342	2384	3053	1403
603 residential				3127	2085				-603	6099	3948		3218
700 water				1761	515	251	2280	-60		4003	3626	3189	

Note: Values are scaled by 10 000; B0 to B12 represent Blue, Green, Red, NIR, SWIR1.6, SWIR2.1, Brightness, Greenness, Wetness, NDVI, SR, EVI & ND24_57 respectively

The variables and thresholds in Tables 3-10 and 3-11 were used to generate the OSRBC. The OSRBC was applied to all three areas and the resulting confusion matrix is provided in Table 3-12. Note that *101 riparian forest* and *302 Acacia* could not be classified.

Table 3-12 Confusion matrix of the OSRBC for all areas combined

Classified class	101 dry woodland	101 green woodland	101 rain forest	101 riparian forest	102 shrubs	104 dry grassland	104 green grassland	301 *Pinus*	302 *Acacia*	302 *Eucalyptus*	303 fruit trees	304 vineyards	305 maize	305 sugar	306 banana	500 bare	601 linear feature	602 commercial	603 residential	700 water	Total (user)
101 dry woodland	27	1	0	0	0	10	0	0	0	0	0	1	0	0	0	0	0	0	0	0	39
101 green woodland	0	31	0	1	0	0	0	0	1	0	3	0	0	2	0	1	0	0	0	0	39
101 rain forest	0	0	10	0	0	0	0	0	1	0	0	0	0	0	0	0	0	0	0	0	11
101 riparian forest	0	0	0	0	0	0	0	1	0	1	0	0	0	0	0	0	0	0	0	0	2
102 shrubs	0	0	0	0	30	0	0	0	0	0	0	0	0	0	0	4	0	1	0	0	35
104 dry grassland	11	0	0	0	0	34	0	0	0	0	0	2	0	0	0	3	0	0	0	0	50
104 green grassland	0	0	0	0	0	0	2	0	0	0	0	0	0	0	0	0	0	0	0	0	2
301 *Pinus*	0	0	5	0	0	0	0	110	0	0	0	0	0	0	0	0	0	0	0	0	115
302 *Acacia*	0	0	0	0	0	0	0	0	0	0	0	0	0	0	0	0	0	0	0	0	0
302 *Eucalyptus*	0	0	0	0	0	0	0	0	0	14	0	0	0	0	0	0	0	0	0	0	14
303 fruit trees	2	9	0	0	0	0	0	0	0	0	33	0	0	1	0	0	0	0	0	0	45
304 vineyards	3	0	0	0	0	5	2	0	0	0	0	37	0	0	0	13	0	0	2	0	62
305 maize	0	0	0	0	0	0	0	0	0	0	0	0	12	0	0	0	0	0	0	0	12

305 sugar	1	2	0	0	0	0	0	0	1	2	0	0	0	15	2	0	0	0	0	0	23
306 banana	0	1	0	0	0	0	0	0	0	0	1	0	0	2	2	0	0	0	0	0	6
500 bare	2	0	0	0	0	0	0	0	0	0	0	13	0	0	0	53	3	3	2	0	76
601 linear feature	0	0	0	0	0	0	0	0	0	0	0	0	0	0	0	0	16	20	0	0	36
602 commercial	0	0	0	0	0	0	0	0	0	0	0	0	0	0	0	0	6	49	1	0	56
603 residential	0	0	0	0	0	1	0	0	0	0	0	0	0	1	0	0	0	0	52	0	54
700 water	0	0	0	0	0	0	0	0	0	0	0	0	0	0	0	0	0	0	0	84	84
Not classified	46	15	5	27	9	7	21	58	11	76	17	8	0	15	11	23	4	16	32	3	404
Total (producers)	92	59	20	28	39	57	25	169	14	93	54	61	12	36	15	97	29	89	89	87	1165

Despite the misclassifications and non-class allocated samples, the classification has an overall accuracy of 80.3%, with lower and upper confidence intervals of 77.4% and 83.2% respectively. This produces a kappa value of 0.79 with a quantity disagreement of 5.8% and allocation disagreement of 13.9%. Classification results for individual classes are provided in Table 3-13 below, which shows kappa values and producer and user accuracies with their respective 95% confidence intervals.

Table 3-13 Individual OSRBC class accuracies

Class name	Producer accuracy (%)	Producer 95% confidence interval lower (%)	Producer 95% confidence interval upper (%)	User accuracy (%)	User 95% confidence interval lower (%)	User 95% confidence interval upper (%)	Kappa statistic
101 dry woodland	58.7	43.4	74	69.2	53.5	85	0.7
101 green woodland	70.5	55.8	85.1	79.5	65.5	93.4	0.8
101 rain forest	66.7	39.5	93.9	90.9	69.4	100	0.9
101 riparian forest	0	0	50	0	0	25	0
102 shrubs	100	98.3	100	85.7	72.7	98.7	0.9
104 dry grassland	68	54.1	81.9	68	54.1	81.9	0.7
104 green grassland	50	0	100	100	75	100	1
301 *Pinus*	99.1	96.9	100	95.7	91.5	99.8	0.9
302 *Acacia*	0	0	0	0	0	0	0
302 *Eucalyptus*	82.4	61.3	100	100	96.4	100	1
303 fruit trees	89.2	77.8	100	73.3	59.3	87.4	0.7
304 vineyards	69.8	56.5	83.1	59.7	46.7	72.7	0.6
305 maize	100	95.8	100	100	95.8	100	1
305 sugar	71.4	49.7	93.1	65.2	43.6	86.9	0.6
306 banana	50	0	100	33.3	0	79.4	0.3
500 bare	71.6	60.7	82.6	69.7	58.8	80.7	0.7
601 linear feature	64	43.2	84.8	44.4	26.8	62.1	0.4
602 commercial	67.1	55.7	78.6	87.5	77.9	97.1	0.9
603 residential	91.2	83	99.4	96.3	90.3	100	1
700 water	100	99.4	100	100	99.4	100	1

To illustrate the performance of machine learning using all features calculated with GEOBIA, a confusion matrix of the SVM classification with samples selected over only the KZN study area

and applied to the same area is provided in Table 3-14 as example. There is clearly some confusion between *301 Pinus*, *302 Eucalyptus*, and *302 Acacia*, which led to a user accuracy of 80%, 87%, and 96.6% for these classes respectively.

Table 3-14 Confusion matrix of the SVM classification for the KZN study area using local signatures only as opposed to signatures from other areas

Classified class	101 green woodland	101 rain forest	301 *Pinus*	302 *Acacia*	302 *Eucalyptus*	305 maize	305 sugar	500 bare	602 commercial	700 water	Total (user)
101 green woodland	35	0	0	0	0	0	0	0	0	0	35
101 rain forest	0	18	2	0	0	0	0	0	0	0	20
301 *Pinus*	0	0	16	1	3	0	0	0	0	0	20
302 *Acacia*	1	0	0	14	1	0	0	0	0	0	16
302 *Eucalyptus*	0	0	0	0	28	0	1	0	0	0	29
305 maize	0	0	0	0	0	12	0	0	0	0	12
305 sugar	0	0	0	0	1	0	36	2	0	0	39
500 bare	0	0	0	0	0	0	0	30	1	0	31
602 commercial	0	0	0	0	0	0	0	1	27	0	28
700 water	0	0	0	0	0	0	0	0	0	41	41
Total (Producers)	36	18	18	15	33	12	37	33	28	41	271

The overall performance of the SVM classifier for the KZN study area is summarised in Table 3-15. The low kappa value of 0.79 of *301 Pinus* should be noted, but is still above what was achieved with the OSRBC.

Table 3-15 SVM classification accuracy summary for the KZN study area

Class name	Producer accuracy (%)	Producer 95% confidence interval lower (%)	Producer 95% confidence interval upper (%)	User accuracy (%)	User 95% confidence interval lower (%)	User 95% confidence interval upper (%)	Kappa statistic
101 green woodland	97.20	90.50	100.00	100.00	98.60	100.00	1.00
101 rain forest	100.00	97.20	100.00	90.00	74.40	100.00	0.89
301 *Pinus*	88.90	71.60	100.00	80.00	60.00	100.00	0.79
302 *Acacia*	93.30	77.40	100.00	87.50	68.20	100.00	0.87
302 *Eucalyptus*	84.80	71.10	98.60	96.60	88.20	100.00	0.96
305 maize	100.00	95.80	100.00	100.00	95.80	100.00	1.00
305 sugar	97.30	90.70	100.00	92.30	82.70	100.00	0.91
500 bare	90.90	79.60	100.00	96.80	88.90	100.00	0.96
602 commercial	96.40	87.80	100.00	96.40	87.80	100.00	0.96
700 water	100.00	98.80	100.00	100.00	98.80	100.00	1.00

The effectiveness of signature extension between study sites is illustrated in Table 3-16. In most cases, using the combined training samples from the respective other two external study sites improved the classification accuracy, but this difference is well within the confidence interval. In

general it seems that the SVM classification outperforms the RF classification slightly during signature extension, but this is not significant as values are within each other's error budgets at 95% confidence intervals.

Table 3-16 Summary of RF and SVM classification results using signatures from within the study site (INT) versus using the combined signatures from the two exterior areas (EXT)

	KZN RF EXT	KZN RF INT	KNP RF EXT	KNP RF INT	CPT RF EXT	CPT RF INT	KZN SVM EXT	KZN SVM INT	KNP SVM EXT	KNP SVM INT	CPT SVM EXT	CPT SVM INT
Overall accuracy (%)	94.7	93.4	93.9	93.6	95.7	95.9	95.2	94.8	94.9	93.8	95.0	97.9
95% confidence lower	91.7	90.2	91.5	91.0	93.8	94.1	93.9	92.0	93.6	91.3	93.7	96.5
95% confidence upper	97.6	96.5	96.4	96.1	97.6	97.8	96.5	97.7	96.2	96.3	96.3	99.4
Overall kappa statistic	0.94	0.93	0.93	0.92	0.95	0.95	0.95	0.94	0.95	0.92	0.95	0.98
Quantity disagree (%)	3.1	2.2	1.5	1.2	3.1	2.9	1.5	2.6	1.4	2.2	1.5	1.8
Allocation disagree (%)	2.3	4.4	4.5	5.2	1.2	1.2	3.3	2.6	3.7	4.0	3.5	0.2

3.5 DISCUSSION

Lück & Van Niekerk (2016) showed that extensive image pre-processing in the form of radiometric normalisation to TOA reflectance and topographic normalisation significantly reduced the variability between imagery and allowed the production of image composites suitable for automatic classifications. This is supported by the visual comparison of raw input data and normalised composites in Figure 3-8. The composites generated in this study were suitable for input to classification processes as long as the seasonal variability over classes of interest was not too pronounced.

The results of the classification experiments showed that SRC and SPECL rule-based classifications were not suitable for discriminating forest classes (Table 3-7 and Table 3-8). Specifically, SRC's use of thresholds to group objects into high, medium, and low spectral classes were not effective in discriminating between natural land cover and forest class boundaries. SPECL, on the other hand, used no indices except for band ratios, and worked on thresholds derived purely from spectral data. Based on spectral curves plotted in Figure 3-3, the difficulty of achieving a clean separation between these classes is illustrated.

In contrast, OSRBC's definition of a hyperplane at equal standard deviation distances from class means was the most effective. These thresholds can be automatically calculated and provide the user with feedback on the classification accuracy.

As with SPECL and JRC, however, OSRBC also uses thresholds that can be close to one another in feature space. When applied to highly correlated features, such thresholds can produce a non-exhaustive classification, similar to the parallelepiped statistical classifier. Nonetheless, the

classification results of the OSRBC were acceptable with an accuracy of 80.3% and a kappa value of 0.79. A definition of a hyperplane, which is the infliction point in feature space between two classes with equal standard deviations away from one another's mean values, reduces classification error and should be used as the threshold level to differentiate between these two classes within a rule-based classification.

To address this shortcoming of the OSRBC, an iterative approach can be used whereby new indices can be calculated and data transformed with eigen vectors to eliminate class overlap in feature space during a following iteration of OSRBC. This can be repeated until sufficient separability between classes is achieved, or a decision is made to merge similar classes. In cases where there are many classes, other studies have found that the most successful approach is to group those with similar properties, thereby separating these clusters in a decision tree first, before using rules that provide an exhaustive classification. Classes within a cluster can be teased out in a separate feature space analysis. If the feature space is transformed into principal components and decorrelated features, the effect of a boxed feature space delineation is reduced. This iterative rule-based development was not assessed in this study and should be examined closer in further research studies.

The classification results of the two machine learning classifiers were high, with overall kappa values above 0.9. SVM slightly outperforming RF, but the differences between the accuracies of the two techniques are within the 95% confidence limits. Generally speaking, the RF classifier performs better when the number of samples per class is balanced. The samples in this study were somewhat imbalanced due to the expensive method of field data collection and statistical sampling, which may have contributed to RF's lower accuracies when compared to the SVM classifier.

Using signatures from other study areas (located in other climatic regions) did not reduce the performance of the two machine learning classifiers. This is very promising as it suggests that signatures for predefined forestry classes can be used in sub-tropic and tropic areas with marginal seasonal spectral fluctuations, irrespective of temporal and spatial distances. When training the classifier with samples from outside the study area, a slight increase in classification accuracy was observed for the RF classifier in both the KZN and KNP study areas. This suggests that the RF classification can be improved with more samples, and thus the RF classification generally requires more samples than a SVM classification. When the classifier was trained with samples from outside the study area for the CPT study area, the classification accuracy was lower both for the RF and SVM methods. This suggests that the spectral variability between CPT versus the other two sites is greater, and classification performance cannot be offset by

increasing the sample size. The Mediterranean climate in the CPT study area that contains *Pinus radiata* and other *Eucalyptus* species suggests that these species produce a different spectral response than other members of their genus that are found in the KZN and KNP study areas. It needs to be noted, however, that these differences are not statistically significant as they fall within the 95% confidence interval of each individual classification.

3.6 CONCLUSION

In conclusion, we can say that radiometric normalisation of satellite imagery is critical in producing accurate and reliable classification results. With proper radiometric normalisation to TOA reflectance, topographic normalisation, and pixel-based spectral classification, it is possible to evaluate different image-compositing techniques. This research has shown that preprocessed imagery composited in the above mentioned way allows for the automatic classification of forests, and it even extends classification models to areas from which no training samples were initially collected – a technique referred to as signature extension.

This study also successfully evaluated the use of three rule-based classifications versus two machine learning classifiers. The results showed that the SRC and SPECLE rule-based classifiers were less suitable for generating thematic land cover classes and should rather be used for image pre-processing such as topographic normalisation, atmospheric correction, and image compositing (Lück & Van Niekerk 2016). This is primarily due to the difficulty of remapping thematic classes from one classification to another, and secondly due to the rather primitive set of spectral features and thresholds used for these classifications.

The similarity of spectral signatures between classes, as illustrated in Figure 3-3, makes it apparent that spectral indices and linear transformations of data improved the ability to discriminate between spectral classes. This is further illustrated in Table 3-9, where the better performance of the OSRBC was compared to the other two rule-based classifications.

This study has shown that machine learning classifiers such as RF and SVM outperform rule-based classifications such as SPECL, JRC SRC, and the OSRBC. Both the RF and SVM classifiers performed well in discriminating forest classes when trained with samples collected within an area of interest. Furthermore, this study has shown that when training samples are taken from outside the area to be classified, those signatures can be extended to forest classes when using machine learning classifiers. This implies that once trained, both the RF and SVM classifiers can be used on other imagery from the same sensor, namely for different time periods, extended geographic areas, or both.

Future research should determine how a critical geographic distance can be determined, so that libraries of geographically- and thematically-indexed training samples can be constructed. This technique has the potential to reduce sample collection effort globally for automated machine learning classifications.

CHAPTER 4: CONCLUDING SYNTHESIS AND RECOMMENDATIONS FOR FUTURE RESEARCH

4.1 REFLECTING ON THE RESEARCH

Geoinformation products are needed for strategic, tactical, and operational planning, and for the monitoring and management of sustainable and optimal forest use. This thesis concentrated on the extraction of thematic geoinformation products relating to forest type and cover, with specific emphasis on genus classification in plantation forests. Remote sensing was identified as a viable technology to reliably and efficiently extract this information.

The overarching research question was formulated as: *How can existing freely available remote sensing data be used to automatically generate geoinformation products required for forestry applications?*

To address this question, four objectives were set. The first objective was to develop and evaluate an image compositing technique that is completely automated and that produces an image output that is suitable for the extraction of geoinformation. The second objective focused on the development of automatic image classification techniques for extracting thematic forestry information from the imagery. The third objective was to compare the resulting classification techniques to existing rule-based and machine learning classifiers, while the final objective was to identify research gaps and make suggestions.

A range of remote sensing methods and techniques were considered to address the objectives. Optical multispectral imagery was chosen, in particular Landsat data, because it is well calibrated and has a sufficient spatial, spectral, and temporal resolution for many forest applications. Its low cost and the large archive of available historical images were other motivations for choosing Landsat imagery as main data source for this research. Three study sites in South Africa with diverse climatic and topographical conditions and varied forest types were chosen with the aim to develop automated, transferable techniques that are consistent, accurate, and applicable to large geographic areas.

Chapter 2 addressed the first Objective and reported on the development of a new methodology called rule-based compositing (RBC), which is optimised for Landsat imagery. RBC involved masking invalid or poor observations and combining good observations in a temporal stack of images into a single artefact-free composite. The new method was compared to three existing compositing techniques, namely NDVI maximum value compositing (MaxNDVI), minimum red band reflectance (mRed), and maximum ratio method (maxRatio). The results showed that RBC provided a 55% increase in performance compared to the next best method (maxRatio). RBC's

better performance was attributed its use of a hybrid inference procedure in which inductive data-learning is used in a pre-classification, which allows for applying compositing rules optimised for specific surface types.

Chapter 3 investigated how image composites generated with the RBC can be automatically classified into different land cover classes (Objective 2). Geographical object-based image analysis (GEOBIA) was used as the underlying paradigm for all aspects of this investigation. A novel rule-based classification method, called optimised spectral rule-based classification (OSRBC), was designed and implemented for the purpose of this investigation. The accuracy of the OSRBC was compared to that of four other classification techniques (Objective 3) of which two were rule-based, while the other two belonged to the domain of machine learning. Spectral rule-based classification (SRC) and SPECLE were selected as the rule-based techniques as they are well known in the remote sensing community. The selected machine learning algorithms were support vector machines (SVM) and random forest (RF). The results showed that SRC and SPECLE were not suitable for extracting forest classes and plantation genus classes, as the spectral classes that these algorithms produce could not be translated to the desired informational classes. OSRBC was better suited for forest classification and performed reasonably well in all areas, resulting in an overall accuracy of 80% and kappa value of 0.78. This was attributed to OSRBC's use of optimal features and thresholds to discriminate between classes, thereby identifying linear hyperplanes. It was, however, unable to provide an exhaustive classification (i.e. not all image elements were classified) and performed poorly with features that are highly correlated and classes with strong overlaps in feature space. In contrast, the two machine learning classification techniques produced excellent results and achieved overall classification accuracies of between 93% and 98%. The SVM performed slightly better than RF, but the difference in performance was insignificant.

The main disadvantage of the machine learning classifiers is their reliance on local data to train the models. The two machine learning techniques' ability to be trained with samples collected from a remote site (up to 1500 km away) – a remote sensing concept called signature extension – was therefore evaluated. For classes that are relatively spectrally invariant, such as forests, it was demonstrated that signature extension could be applied reliably without significant deterioration of classification accuracy. This finding suggests that it is feasible to use generic signature libraries for training machine learning classifiers within certain geographic strata, thereby facilitating fully automated and accurate forest classifications. Based on the results of this study, one can deduce that machine learning classifiers are superior to rule-based classifiers and that

research should focus on the development and use of machine learning classifiers for forest classifications.

The final objective (Objective 4) was to identify the remaining research gaps and to make recommendations for future research, which will be addressed in the next section and in the Appendices II–VI.

4.2 REMAINING RESEARCH GAPS

Many challenges for the automatic, cost effective, and accurate extraction of thematic information from remotely sensed imagery for forestry applications remain. This study was conducted within traditional remote sensing and forestry domains. As the work progressed, it became apparent that some of the encountered problems are not unique to these domains, and have been the focus of electronic engineering, sensor design, computer vision, and high performance computing research for some time. It seems that these domains offer solutions to many of the problems encountered in this study, but the potential solutions only became evident towards the end of the research activities, and as such, they were not incorporated into this study. These technologies and approaches are, however, critical for automated product development for the forestry and other industries and should be the focus of future research. As a starting point, the remaining gaps and opportunities for future research are briefly summarised in this section. For the sake of brevity, some of the ideas and concepts are expanded upon in appendixes.

A fundamental challenge faced in many fields of remote sensing is the use of multi-temporal, multi-resolution, and multi-source (MTMRMS) imagery for the generation of a single informational product. Existing methods for storing, pre-processing, analysing, and presenting such data are often cumbersome and inefficient, and would benefit from revision. More research is needed to investigate alternative methods; however, some suggestions are made below:

- To reduce storage requirements and to enable analyses of multi-resolution (e.g. spatial, temporal, spectral, radiometric, polarimetric, and multi-angular) data from a wide range of sensors within one framework, an irregular lattice data model should be investigated. Such a model is scalable and can thus accommodate big data volumes. It will also allow for the ingestion of data in the original sensor geometry. For a conceptual overview of this data model, see Appendix III.
- The development of reliable rule-based classifications for pre-processing and quality assessment (see Chapter 2) needs attention. The rule base should define appropriate classes that do not overlap in feature space. Some ideas on how to improve the existing rule-based methods are provided in Appendix IV.

- More work on cross-sensor calibration is needed to enable direct comparison of measurements between different sensors.
- Image pre-processing techniques to improve radiometric and geometric corrections should receive further attention. Specifically, techniques for the co-registration of data to at least 1/10 (preferably 1/100th) of a pixel is needed. This is necessary for the preservation of radiometric fidelity, as the majority of the signal comes from the centre 30% of the picture element, depending on the point spread function of the sensor (see Appendix III for more details). Radiometric conditioning in terms of BRDF correction, topographic normalisation, and atmospheric corrections would benefit from automation to make these processes more reliable and accessible. Here the integration of measurements from different sensors will be required (refer to Appendix V for a conceptual overview of how this can be achieved).
- Analysis techniques that expand on object-orientated classifications using deep learning and artificial intelligence should receive much more attention. The analysis and rapid information extraction of hyper-temporal data cubes are research priorities. Some specific image classification research ideas are provided in Appendix VI.

4.3 THE FUTURE OF REMOTE SENSING IN FORESTRY

The future of using remote sensing as a tool to support sustainable forestry operations is bright. We are at a time in history where technologies for sustainable forest management and remote sensing are converging. These technologies include the automatic generation of analysis-ready data, computerised harvesting systems using robotics, individual tree-crown detection, and multi-temporal, multi-source image analysis in data cubes. As highlighted in Section 1.1, ensuring the sustainable use and management of this valuable resource is essential for the survival of mankind.

A new range of datasets and sensors that have tremendous potential for the methods highlighted or developed in this research are becoming available on the remote sensing market. These datasets include the following:

1. Sentinel-2, with 2A being launched in 2015 and 2B launched in 2017. These super-spectral sensors have a higher resolution and similar but more bands to Landsat 8, thereby making the missions complimentary. The spatial resolution of 10 m for VISNIR, 20 m for vegetation bands, and 60 m for coastal and atmospheric bands allow for accurate pre-processing and unprecedented analysis opportunities. The revisit time of five days allows for the development of operational remote sensing services from free and open data.

Image compositing as developed in Chapter 2 and automatic classification techniques validated in Chapter 3 should be of great relevance, as they can optimise this data for forestry applications. This data will allow the early detection of growth anomalies and plant/tree stress at a continental scale, map damage from fire, windfall, pest attack, and deforestation within a week of the event taking place.

2. Landsat 9 (to be launched in 2020) will be an exact copy of Landsat 8, flying in tandem with its twin, thereby reducing the revisit time to eight days. With the Landsat satellites being well-calibrated and considered to be the golden standard with respect to radiometric accuracy and fidelity, imagery from these two satellites will play a vital role in the cross-sensor calibration of other missions that may be used for advanced forestry-related remote sensing applications. Research of this thesis used data from Landsat 5 and 7 and these techniques are easily transferred to present and future Landsat missions such as 8 and 9.

3. Planet Labs Inc., also simply referred to as Planet, have launched a constellation of 175+ shoebox-sized Dove satellites that are acquiring 3 m spatial resolution multispectral imagery and are capable of covering the world on a daily basis. Although this data is of poorer radiometric and spectral quality as either the Landsat or Sentinel-2 data, it is available at higher resolution and frequency than these missions. Together with the archive of RapidEye imagery and 13 very high spatial resolution SkySat satellites, which are producing imagery at a spatial resolution of 80 cm, they are able to serve operational and commercial forestry applications for high value products. Planet is the first commercial satellite vendor that is offering analysis-ready data from their Planetscope Doves. This makes it a prime candidate for implementing advanced image compositing techniques and automatic classification methodologies highlighted in this thesis.

4. UrtheDaily is a constellation of six satellites equipped with super-spectral sensors similar to those from Sentinel-2, albeit at a spatial resolution of 5 m. Once operational, they will acquire all land masses of the world on a daily basis and are set to compete with Planet. These satellites, which are planned to be launched in 2020, should produce a much higher quality of data compared to Planetscope Doves, and could thus capture a considerable market share for forestry applications. Image compositing and automatic image classification, as well as time-series analysis of ARD in a data cube, will form the core competency of this mission. Technology challenges and developments highlighted in Appendix III–Appendix VI should receive considerable attention in preparation for this mission.

5. High Altitude Pseudo Satellites are large solar powered drones, capable of flying for months on end in the stratosphere at altitudes between 50 000–70 000 feet. These systems have been prototyped and are operated by Airbus to acquire high quality and high resolution remotely sensed imagery for forestry and other applications in the near future. These systems will target forestry markets at national level and will enable the digitalisation and automation of forest inventories and other forestry geoinformation requirements mentioned in Section 1.2 of this thesis. Data from these systems will rely on imagery from Landsat and Sentinel, as well as on the above mentioned commercial missions, to derive the greatest value for operational applications.

As highlighted above, the research carried out in the present study can be used for and applied to datasets from new sensors and missions. Image compositing is a critical processing step for the normalisation and reduction of data that will be subjected to time-series analysis and automatic classification of imagery. This thesis demonstrated how forest masks can be automatically generated. Such forest masks are a prime geoinformation source for national forest planning and monitoring activities required for carbon trading and participation in the REDD+ initiative.

4.4 CONCLUDING REMARKS

Forests are critical for our wellbeing and survival as they bind CO_2, play an active role in the water cycle through evapotranspiration, and bind nutrients to the soil. They also contribute to the biodiversity of the planet, with potential value for improving our wellbeing both spiritually, intellectually, and physically. Forests provide renewable wood, fibre, and other by-product resources. All of these factors make the pursuit of sustainable use and management of our biotic environment, and the many valuable resources within it, a worthwhile endeavour.

This research highlighted and addressed several remote sensing challenges and has provided a foundation for operational geoinformation service delivery from Landsat imagery for a narrowly defined forestry application. It has been demonstrated that the pre-processing and radiometric normalisation of imagery enable a rule-based compositing that can, in turn, produce suitable input data for an automatic spectral classification. It was shown that machine learning techniques (e.g. random forests and support vector machines) and signature extension can be used to fully automate the classification of remote sensing imagery, especially when dealing with forest land cover types. The main contribution of this research was thus the generation of image composites and large-scale automated plantation genus cover mapping in the subtropics. The use of these images to assess the forest type, its extent, and the land cover change can facilitate and aid the sustainable management of this precious natural resource.

REFERENCES

Achard F (ed) 2012. *A sourcebook of methods and procedures for monitoring and reporting anthropogenic greenhouse gas emissions and removals associated with deforestation, gains and losses of carbon stocks in forests remaining forests, and forestation*. GOFC-GOLD sourcebook. The Netherlands: Wageningen University.

Anderson DA 2010. *Environmental economics and natural resource management*. London; New York: Routledge.

Maps Population, Landscape and Climate Estimates (PLACE), v3: National Aggregates of Geospatial Data Collection (NAGDC) | SEDAC 2013. Available from: http://sedac.ciesin.org/data/set/nagdc-population-landscape-climate-estimates-v3/maps2013 [Accessed].

Forest resources and plantations of the Gambia 2015. Available from: http://www.fao.org/docrep/004/X6808E/X6808E03.htm [Accessed 15 April 2015].

Arvidson T Gasch J & Goward SN 2001. Landsat-7's Long-Term Acquisition Plan — an iInnovative aApproach to bBuilding a gGlobal iImagery aArchive. *Remote Sensing of eEnvironment*, 78, 1-2: 13-26.

Asner GP, Levick SR & Cleland E 2012. Landscape-Scale Effects of Herbivores on Treefall in African Savannas. *ELE Ecology Letters*, 15, 11: 1211-1217.

Asrar G, Fuchs M, Kanemasu ET & Hatfield JL 1984. Estimating Absorbed Photosynthetic Radiation and Leaf Area Index from Spectral Reflectance in Wheat1. *Agron.J* 76, 2: 300-306.

Baraldi A & Boschetti L 2012a. Operational Automatic Remote Sensing Image Understanding Systems: Beyond Geographic Object-Based and Object-Oriented Image Analysis (GEOBIA/GEOOIA). Part 1: Introduction. *Remote Sensing* 4, 12: 2694-2735.

Baraldi A & Boschetti L 2012b. Operational Automatic Remote Sensing Image Understanding Systems: Beyond Geographic Object-Based and Object-Oriented Image Analysis (GEOBIA/GEOOIA). Partcc 2: Novel System Architecture, Information/Knowledge Representation, Algorithm Design and Implementation. *Remote Sensing* 4, 12: 2768-2817.

Baraldi A 2009. Impact of Radiometric Calibration and Specifications of Spaceborne Optical Imaging Sensors on the Development of Operational Automatic Remote Sensing Image Understanding Systems. , *IEEE Journal of Selected Topics in Applied Earth Observations and Remote Sensing* 2, 2: 104-134.

Baraldi A, Boschetti L & Humber ML 2014. Probability Sampling Protocol for Thematic and Spatial Quality Assessment of Classification Maps Generated from Spaceborne/Airborne very High Resolution Images. *IEEE Transactions on Geoscience and Remote Sensing* 52, 1: 701-760.

Baraldi A, Durieux L, Simonetti D, Conchedda G, Holecz F & Blonda P 2010a. Automatic Spectral Rule-Based Preliminary Classification of Radiometrically Calibrated SPOT-4/-5/IRS, AVHRR/MSG, AATSR, IKONOS/QuickBird/OrbView/GeoEye, and DMC/SPOT-1/-2 Imagery—Part II: Classification Accuracy Assessment. *IEEE Transactions on Geoscience and Remote Sensing* 48, 3: 1326-1354.

Baraldi A, Durieux L, Simonetti D, Conchedda G, Holecz F & Blonda P 2010b. Automatic Spectral-Rule-Based Preliminary Classification of Radiometrically Calibrated SPOT-4/-5/IRS, AVHRR/MSG, AATSR, IKONOS/QuickBird/OrbView/GeoEye, and DMC/SPOT-1/-2 Imagery—Part I: System Design and Implementation. *IEEE Transactions on Geoscience and Remote Sensing* 48, 3: 1299-1325.

Baraldi A, Durieux L, Simonetti D, Conchedda G, Holecz F & Blonda P 2010c. Corrections to "Automatic Spectral Rule-Based Preliminary Classification of Radiometrically Calibrated SPOT-4/-5/IRS, AVHRR/MSG, AATSR, IKONOS/QuickBird/OrbView/GeoEye, and DMC/SPOT-1/-2 Imagery" [Mar 10 1299-1325 and 1326-1354]. *IEEE Transactions on Geoscience and Remote Sensing* 48, 3: 1635-1635.

Baraldi A, Gironda M & Simonetti D 2010. Operational Two-Stage Stratified Topographic Correction of Spaceborne Multispectral Imagery Employing an Automatic Spectral-Rule-Based Decision-Tree Preliminary Classifier. *IEEE Transactions on Geoscience and Remote Sensing* 48, 1: 112-146.

Baraldi A, Puzzolo V, Blonda P, Bruzzone L & Tarantino C 2006. Automatic Spectral Rule-Based Preliminary Mapping of Calibrated Landsat TM and ETM+ Images. *IEEE Transactions on Geoscience and Remote Sensing* 44, 9: 2563-2586.

Barbosa, PM, Pereira JMC & Grégoire J 1998. Compositing Criteria for Burned Area Assessment using Multitemporal Low Resolution Satellite Data. *Remote Sensing of Environment* 65, 1: 38-49.

Beaudoin D, Frayret J & LeBel L 2008. Hierarchical Forest Management with Anticipation: An Application to Tactical-Operational Planning Integration. *Canadian Journal of Forest Research* 38, 8: 2198-2211.

Benz UC, Hofmann P, Willhauck G, Lingenfelder I & Heynen M 2004. Multi-Resolution, Object-Oriented Fuzzy Analysis of Remote Sensing Data for GIS-Ready Information. *ISPRS Journal of Photogrammetry and Remote Sensing* 58, 3-4: 239-258.

Blaschke T 2010. Object Based Image Analysis for Remote Sensing. *ISPRS Journal of Photogrammetry and Remote Sensing* 65, 1: 2-16.

Boqo S & Matshate J 2010. Global Forest Resource Assessment 2010, Country Reports, South Africa. FRA2010/195.

Breaker LC, Armstrong EM & Endris CA 2010. Establishing an Objective Basis for Image Compositing in Satellite Oceanography. *Remote Sensing of Environment* 114, 2: 345-362.

Bredenkamp BV & Upfold SJ 2012. *South African forestry handbook*. Menlo Park: Southern African Institute of Forestry.

Brems E, Lissens G & Veroustraete F 2000. MC-FUME: A New Method for Compositing Individual Reflective Channels. *IEEE Transactions on Geoscience and Remote Sensing* 38, 1: 553-569.

Brownlee, J 2017. *Machine Learning Mastery*.
Available from: https://machinelearningmastery.com/ [Accessed on 31 August 2017].

Campbell J 1996. *Introduction to remote sensing*. London: Taylor & Francis.

Chuvieco E & Huete A 2010. *Fundamentals of satellite remote sensing*. Boca Raton: CRC Press.

Chuvieco E, Ventura G, Martín MP & Gómez I 2005. Assessment of Multitemporal Compositing Techniques of MODIS and AVHRR Images for Burned Land Mapping. *Remote Sensing of Environment* 94, 4: 450-462.

Cihlar, J 2000. Land cover mapping of large areas from satellites: Status and research priorities. *International Journal of Remote Sensing* 21, 6-7: 1093-1114.

Cihlar J, Guindon B, Beaubien J, Latifovic R, Peddle D, Wulder M, Fernandes R & Kerr J, 2003. From need to product: a methodology for completing a land cover map of Canada with Landsat data. *Canadian Journal of Remote Sensing* 29, 2: 171-186.

Cihlar J, Latifovic R, Chen J, Beaubien J & Li Z 2000. Selecting Representative High Resolution Sample Images for Land Cover Studies. Part 1: Methodology. *Remote Sensing of Environment* 71, 1: 26-42.

Cihlar J, Latifovic R, Chen J, Trishchenko A, Du Y, Fedosejevs G & Guindon B, 2004. Systematic corrections of AVHRR image composites for temporal studies. *Remote Sensing of Environment* 89, 2: 217-233.

Cohen WB, Spies TA & Fiorella M 1995. Estimating the age and, structure of forests in a multi-ownership landscape of western Oregon, U.S.A. *International Journal of Remote Sensing* 16, 4: 721-746.

Curran PJ 1980. Multispectral Remote Sensing of Vegetation Amount. *Progress in Physical Geography* 4: 174-184.

Danaher T, Xiaoliang W & Campbell N 2001. *Bidirectional reflectance distribution function approaches to radiometric calibration of Landsat ETM+ imagery*, 2654-2657. Proceedings of the Geoscience and Remote Sensing Symposium held 2001,

Dennison PE, Roberts DA & Peterson SH 2007. Spectral Shape-Based Temporal Compositing Algorithms for MODIS Surface Reflectance Data. *Remote Sensing of Environment* 109, 4: 510-522.

Dickinson C, Siqueira P, Clewley D & Lucas R 2013. Classification of Forest Composition using Polarimetric Decomposition in Multiple Landscapes. *Remote Sensing of Environment* 131, 0: 206-214.

Dube T, Mutanga O, Elhadi A & Ismail R 2014. Intra-and-Inter Species Biomass Prediction in a Plantation Forest: Testing the Utility of High Spatial Resolution Spaceborne Multispectral RapidEye Sensor and Advanced Machine Learning Algorithms. *Sensors* 14, 8: 15348-15370.

Duque S, Lopez-Dekker P & Mallorqui JJ 2010. Single-Pass Bistatic SAR Interferometry using Fixed-Receiver Configurations: Theory and Experimental Validation. *IEEE Transactions on Geoscience and Remote Sensing* 48, 6: 2740-2749.

Dye M, Mutanga O & Ismail R 2012. Combining Spectral and Textural Remote Sensing Variables using Random Forests: Predicting the Age ofPinus Patulaforests in KwaZulu-Natal, South Africa. *Journal of Spatial Science Journal of Spatial Science* 57, 2: 193-211.

Dye M, Mutanga O & Ismail R 2011. Examining the Utility of Random Forest and AISA Eagle Hyperspectral Image Data to Predict Pinus Patula Age in KwaZulu-Natal, South Africa. *Geocarto International* 26, 4: 275-289.

Dyk A, Leckie D, Tinis S & Ortlepp S 2015. Canada's National Deforestation Monitoring System: System Description.

Eberle J, Clausnitzer S, Hüttich C & Schmullius C 2013. Multi-Source Data Processing Middleware for Land Monitoring within a Web-Based Spatial Data Infrastructure for Siberia. *International Journal of Geo-Information* 2, 3: 553-576.

Elachi C & Van Zyl J 2006. *Introduction to the physics and techniques of remote sensing*. New Jersey: John Wiley & Sons.

Esch T, Thiel M, Schenk A, Roth A, Muller A & Dech S 2010. Delineation of Urban Footprints from TerraSAR-X Data by Analyzing Speckle Characteristics and Intensity Information. *IEEE Transactions on Geoscience and Remote Sensing* 48, 2: 905-916.

FAO 2015. *Forest resources and plantations of the Gambia*. Available from: http://www.fao.org/docrep/004/X6808E/X6808E03.htm [Accessed on 15 April 2015].

Fearnside PM 2003. Deforestation Control in Mato Grosso: A New Model for Slowing the Loss of Brazil's Amazon Forest. *Ambio* 32, 5: 343-345.

Fontana FMA, Trishchenko AP, Khlopenkov KV, Luo Y & Wunderle S 2009. Impact of Orthorectification and Spatial Sampling on Maximum NDVI Composite Data in Mountain Regions. *Remote Sensing of Environment* 113, 12: 2701-2712.

Fowler MJF 2011. Modelling the Acquisition Times of CORONA Satellite Photographs: Accuracy and Application. *International Journal of Remote Sensing* 32, 23: 8865-8879.

Frampton WJ, Dash J, Watmough G & Milton EJ 2013. Evaluating the Capabilities of Sentinel-2 for Quantitative Estimation of Biophysical Variables in Vegetation. *ISPRS Journal of Photogrammetry and Remote Sensing* 82, 0: 83-92.

Franklin SE 2001. *Remote sensing for sustainable forest management*. Boca Raton: Lewis.

Freer-Smith PH, Broadmeadow MSJ & Lynch JM 2007. Forestry and climate change. Wallingford; Cambridge: CABI Pub.

Friedlander SK 2000. *Smoke, dust, and haze: Fundamentals of aerosol dynamics*. New York: Oxford University Press.

Garestier F, Dubois-Fernandez PC & Papathanassiou KP 2008. Pine Forest Height Inversion using Single-Pass X-Band PolInSAR Data. *IEEE Transactions on Geoscience and Remote Sensing* 46, 1: 59-68.

Gobron N, Pinty B, Verstraete MM, Widlowski J & Diner DJ 2002. Uniqueness of Multiangular Measurements-Part II: Joint Retrieval of Vegetation Structure and Photosynthetic Activity from MISR. *IEEE Transactions on Geoscience and Remote Sensing* 40: 1574-1592.

Govender M, Chetty K & Bulcock H 2007. A Review of Hyperspectral Remote Sensing and its Application in Vegetation and Water Resource Studies. *Water SA* 33, 2: 145-151.

Gutman G 2008. Towards Monitoring Land-Cover and Land-use Changes at a Global Scale: The Global Land Survey 2005. *Photogrammetric Engineering and Remote Sensing* 75, 1: 6-10.

Gutman GG, Ignatov AM & Olson S 1994. Towards Better Quality of AVHRR Composite Images Over Land: Reduction of Cloud Contamination. *Remote Sensing of Environment* 50, 2: 134-148.

Guyon D 1992. *Relating Forest Biomass to SAR Data*.

Hagolle O, Lobo A, Maisongrande P, Cabot F, Duchemin B & De Pereyra A 2005. Quality Assessment and Improvement of Temporally Composited Products of Remotely Sensed

Imagery by Combination of VEGETATION 1 and 2 Images. *Remote Sensing of Environment* 94, 2: 172-186.

Hanafy ME, Roggemann MC & Guney DO 2014. Detailed Effects of Scattering and Absorption by Haze and Aerosols in the Atmosphere on the Average Point Spread Function of an Imaging System. *Journal of the Optical Society of America*. 31, 6: 1312-1319.

Hanssen RF 2001. *Radar interferometry: Data interpretation and error analysis*. Dordrecht; Boston: Kluwer Academic.

Hargrove EC 1989. *Foundations of environmental ethics*. Englewood Cliffs: Englewood Cliffs, N.J. : Prentice-Hall

Hildebrandt G 1990. Operational Remote Sensing for Forest Damages. ISPRS Journal of Photogrammetry and Remote Sensing, 45(1). :55-56.

Hinckley AD 1980. *Renewable resources in our future*. Oxford; New York: Pergamon Press.

Hirschmüller H 2008. Stereo Processing by Semiglobal Matching and Mutual Information. *IEEE Transactions on Pattern Analysis and Machine Intelligence* 30, 2: 328-341.

Ho SP, Smith WL & Huang HL 2002. Retrieval of Atmospheric-Temperature and Water-Vapor Profiles by use of Combined Satellite and Ground-Based Infrared Spectral-Radiance Measurements. *Applied Optics* 41, 20: 4057-4069.

Honig JM 1999. *Thermodynamics*. San Diego: Academic Press

Houghton JT 1997. *Global warming: The complete briefing*. Cambridge; New York: Cambridge University Press.

Hu B, Lucht W, Strahler AH, Barker-Schaaf C & Smith M 2000. Surface Albedos and Angle-Corrected NDVI from AVHRR Observations of South America. *Remote Sensing of Environment* 71, 2: 119-132.

Huang C, Wylie B, Yang L, Homer C & Zylstra, G 2002. Derivation of a tasselled cap transformation based on Landsat-7 at-satellite reflectance. *International Journal of Remote Sensing* 23, 8: 1741-1748.

Huete A, Justice C & Liu H 1994. Development of Vegetation and Soil Indices for MODIS-EOS. *Remote Sensing of Environment* 49, 3: 224-234.

Huiqing L & Huete A 1995. A Feedback Based Modification of the NDVI to Minimize Canopy Background and Atmospheric Noise. *IEEE Transactions on Geoscience and Remote Sensing* 33, 2: 457-465.

Hüttich C 2011. Assessing Effects of Temporal Compositing and Varying Observation Periods for Large-Area Land-Cover Mapping in Semi-Arid Ecosystems: Implications for Global Monitoring. *Remote Sensing of Environment* 115, 10: 2445-2459.

Ihlen V 2012. *Landsat Data Continuity Mission (LDCM) Level 1 (L1) Data Format Control Book (DFCB).*

Irish RR 2012. *Landsat-7 science data user's handbook; report 430-15-01-003-0, national aeronautics and space administration.* Available from: http://landsathandbook.gsfc.nasa.gov/pdfs/Landsat7_Handbook.pdf [Accessed on 11 December 2012].

Ismail R, Mutanga O, Kumar L & Bob U 2008. Determining the Optimal Spatial Resolution of Remotely Sensed Data for the Detection of Sirex Noctilio Infestations in Pine Plantations in KwaZulu-Natal, South Africa. *South African Geographical Journal* 90, 1: 22-30.

Jordan, C.F. 1969. Derivation of Leaf-Area Index from Quality of Light on the Forest Floor. *Ecology* 50: 663–666

Josh, V. (2017). Why don't the greenhouse gases stop the infrared radiation which gets into the earth? Available from: https://www.quora.com/Why-dont-the-greenhouse-gases-stop-the-infrared-radiation-which-gets-into-the-earth [Accessed on 5 November 2017].

Ju J, Roy DP, Vermote E, Masek J & Kovalskyy V 2012. Continental-Scale Validation of MODIS-Based and LEDAPS Landsat ETM+ Atmospheric Correction Methods. *Remote Sensing of Environment* 122, 0: 175-184.

Karnieli A, Kaufman YJ, Remer L & Wald A 2001. AFRI – Aerosol Free Vegetation Index. *Remote Sensing of Environment* 77, 1: 10-21.

Kauth RJ and Thomas GS 1976. The Tasseled Cap – a Graphic Description of the Spectral-Temporal Development of Agricultural Crops as seen in Landsat. Paper delivered at the Symposium on Machine Processing of Remotely Sensed Data, West Lafayette, Indiana: LARS, Purdue University. June 29-July 1.

Kim D 2014. Global, Landsat-Based Forest-Cover Change from 1990 to 2000. *Remote Sensing of Environment* 155: 178-193.

Köhl M, Magnussen S & Marchetti M 2006. *Sampling methods, remote sensing and GIS multiresource forest inventory*. Berlin: Springer.

Kollmuss A 2010. *Handbook of carbon offset programs : Trading systems, funds, protocols and standards*. London; Washington: Earthscan.

Krieger G 2007. TanDEM-X: A Satellite Formation for High-Resolution SAR Interferometry. *IEEE Transactions on Geoscience and Remote Sensing* 45, 11: 3317-3341.

Kross A, Fernandes R, Seaquist J & Beaubien E 2011. The Effect of the Temporal Resolution of NDVI Data on Season Onset Dates and Trends Across Canadian Broadleaf Forests. *Remote Sensing of Environment* 115, 6: 1564-1575.

Landgrebe D 1997. The Evolution of Landsat Data Analysis. *Photogrammetric Engineering and Remote Sensing* 63, 7: 859-867.

Le Moigne J, Netanyahu NS & Eastman RD 2011. *Image registration for remote sensing*. Cambridge; New York: Cambridge University Press.

Lewinski S & Bochenek Z 2008. Rule-Based Classification of SPOT Imagery using Object-Oriented Approach for Detailed Land Cover Mapping. Paper delivered at the 28th EARSeL Symposium "Remote Sensing for a Changing Europe", 2-5 June 2008, Istanbul, Turkey.

Lewinski S 2005. Land use Classification of ASTER Image - Legionowo Test Site. Paper delivered at the 25th EARSeL Symposium, 6-9 June 2005, Porto, Portugal.

Li Z, Guo M, Wang Z & Zhao L 2014. Forest-Height Inversion using Repeat-Pass Spaceborne polInSAR Data. China Earth Sciences 57, 6: 1314-1324.

Liang S 2004. *Quantitative remote sensing of land surfaces*. New Jersey United States: John Wiley & Sons.

Liang S, Li X & Wang J (eds) 2012. *Advanced remote sensing, terrestrial information extraction and applications*. China: Academic Press.

Liew SC 2013. *Principles of remote sensing - centre for remote imaging and processing CRISP*. Available from: http://www.crisp.nus.edu.sg/~research/tutorial/optical.htm [Accessed on 8 January 2013].

Lück W 2004. *National Land Cover 2000: Satellite Image Processing and Object Orientated Classification Guide*. Centre for Geographical Analysis, Department of Geography and Environmental Studies: University of Stellenbosch.

Lück, W & Diemer N 2008. *Land Cover Class Definition Report*.

Lück W & Van Niekerk A 2016. Evaluation of a Rule-Based Compositing Technique for Landsat-5 TM and Landsat-7 ETM+ Images. *International Journal of Applied Earth Observation and Geoinformation* 47: 1-14.

Luo Y, Trishchenko AP & Khlopenkov KV 2008. Developing Clear-Sky, Cloud and Cloud Shadow Mask for Producing Clear-Sky Composites at 250-Meter Spatial Resolution for the Seven MODIS Land Bands Over Canada and North America. *Remote Sensing of Environment* 112, 12: 4167-4185.

Masek JG, Shock CT & Goward SN 2001. Research Environment for Advanced Landsat Monitoring (REALM): A Computational Approach for Landsat-7 Global Science. *Remote Sensing of Environment* 78, 1-2: 204-216.

Mather P 2004. *Computer processing of remotely sensed images an introduction*. Chichester: John Wiley & Sons.

Mathieu R, Naidoo L, Cho MA, Leblon B, Main R, Wessels K, Asner GP, Buckley J, Van Aardt J, Erasmus BFN & Smit IPJ 2013. Toward structural assessment of semi-arid African savannahs and woodlands: The potential of multitemporal polarimetric RADARSAT-2 fine beam images. *Remote Sensing of Environment* 138: 215-231.

Maxwell SK & Sylvester KM 2012. Identification of “ever-Cropped” Land (1984–2010) using Landsat Annual Maximum NDVI Image Composites: Southwestern Kansas Case Study. *Remote Sensing of Environment* 121: 186-195.

McDonald ER, Wu X, Caccetta P & Campbell N 2001. *Illumination Correction of Landsat TM Data in South East NSW*.

Mead DJ 2001. Forestry Out-Grower Schemes: A Global View. Paper delivered at the Forest Plantations Thematic Papers, March 2001.

Mongus D & Zalik B 2012. Parameter-Free Ground Filtering of LiDAR Data for Automatic DTM Generation. ISPRS J.Photogramm.Remote Sens. *ISPRS Journal of Photogrammetry and Remote Sensing* 67, 1: 1-12.

Moodley D, Simonis I & Tapamo JR 2012. An Architecture for Managing Knowledge and System Dynamism in the Worldwide Sensor Web. *International Journal on Semantic Web and Information Systems (IJSWIS)* 8, 1: 64-88.

Muundjua M, Hart RJ, Gilder SA, Carporzen L & Galdeano A 2007. Magnetic Imaging of the Vredefort Impact Crater, South Africa. *Earth and Planetary Science Letters* 261, 3-4: 456-468.

Nair VS, Moorthy K, Krishna BS & Suresh SSK 2009. Optical and Physical Properties of Atmospheric Aerosols Over the Bay of Bengal during ICARB. *Journal of the Atmospheric Sciences* 66, 9: 2640-2658.

Oliver C & Quegan S 2004. Understanding synthetic aperture radar images [Homepage of SciTech Publ.], [Online].

Olthof I, Pouliot D, Fernandes R & Latifovic R 2005. Landsat-7 ETM+ Radiometric Normalization Comparison for Northern Mapping Applications. *Remote Sensing of Environment* 95, 3: 388-398.

Ouaidrari H & Vermote EF 1999. Operational Atmospheric Correction of Landsat TM Data. *Remote Sensing of Environment* 70, 1: 4-15.

Ozdogan M & Schumann GJ 2014. A Practical and Automated Approach to Large Area Forest Disturbance Mapping with Remote Sensing. PLoS ONE, 9(4). :e78438.

Pal M 2005. Random Forest Classifier for Remote Sensing Classification. *International Journal of Remote Sensing* 26, 1: 217-222.

Parker C, Mitchell A, Trivedi M & Mardas N 2009. The Little REDD+ Book, Global Canopy Programme.

PCI Geomatics. 2012. Geomatica 2013. October 2012.

Perez-Hoyos A, Garcia-Haro FJ & Valcarcel N 2014. Incorporating Sub-Dominant Classes in the Accuracy Assessment of Large-Area Land Cover Products: Application to

GlobCover, MODISLC, GLC2000 and CORINE in Spain. *IEEE Journal of Selected Topics in Applied Earth Observations and Remote Sensing* 7, 1: 187-205.

Pflugmacher D, Cohen WB & Kennedy RE 2012. Using Landsat-Derived Disturbance History (1972–2010) to Predict Current Forest Structure. *Remote Sensing of Environment* 122: 146-165.

Poona NK & Ismail R 2013. Discriminating the Occurrence of Pitch Canker Fungus in Pinus Radiata Trees using QuickBird Imagery and Artificial Neural Networks. *Southern Forests: a Journal of Forest Science* 75, 1: 29-40.

Potapov PV 2012. Quantifying Forest Cover Loss in Democratic Republic of the Congo, 2000–2010, with Landsat ETM + Data. *Remote Sensing of Environment* 122: 106-116.

Potapov P, Turubanova S & Hansen MC 2011. Regional-Scale Boreal Forest Cover and Change Mapping using Landsat Data Composites for European Russia. *Remote Sensing of Environment* 115, 2: 548-561.

Potapov P, Yaroshenko A, Turubanova S, Dubinin M, Laestadius L, Thies C, Aksenov D, Egorov A, Yesipova Y, Glushkov I, Karpachevskiy M, Kostikova A, Manisha A, Tsibikova E & Zhuravleva I 2008. Mapping the world's intact forest landscapes by remote sensing. *Ecology and Society* 13, 2: 51.

Pouliot D, Latifovic R, Fernandes R & Olthof I 2011. Evaluation of Compositing Period and AVHRR and MERIS Combination for Improvement of Spring Phenology Detection in Deciduous Forests. *Remote Sensing of Environment* 115, 1: 158-166.

Przyborski P 2013. *Irrigation and land surface temperature in oregon: Image of the day*. Available from: http://earthobservatory.nasa.gov/IOTD/view.php?id=7199&src=ve [Accessed on 8 January 2013].

Rasi R, Beuchle R, Bodart C, Vollmar M, Seliger R & Achard F 2013. Automatic Updating of an Object-Based Tropical Forest Cover Classification and Change Assessment. *IEEE Journal of Selected Topics in Applied Earth Observations and Remote Sensing* 6, 1: 66-73.

South Africa (Republic of) 1998. *Government Gazette*. National Forests Act.

Richter R & Schläpfer D 2014. Atmospheric / Topographic Correction for Satellite Imagery.

Richter R 2011a. Atmospheric / Topographic Correction of Satellite Imagery. 8.0. April 2011.

Richter R 2011b. Atmospheric correction methods for optical remote sensing imagery of land. In Weng Q (ed), *Advances in environmental remote sensing, sensors, algorithms, and applications*, 161-172. Florida: CRC Press.

Richter R, Kellenberger T & Kaufmann H 2009. Comparison of Topographic Correction Methods. *Remote Sensing* 1, 3: 184-196.

Roy DP, Ju J & Kommadreddy I 2011. Web-Enabled Landsat Data (WELD): A Consistent, Long-Term, Large-Area, 30m Data Record for the Terrestrial User Community. Paper delivered at the 34th International Symposium on Remote Sensing of Environment, April 10-15 2011, Sydney, Australia.

Roy DP 2010. Web-Enabled Landsat Data (WELD): Landsat ETM+ Composited Mosaics of the Conterminous United States. *Remote Sensing of Environment* 114, 1: 35-49.

Roy DP 2011. *Web enabled Landsat data (WELD) products - algorithm theoretical basis document*. South Dacota: State University.

Roy DP 2011. Web Enabled Landsat Data (WELD) Products . 1.0.

Roy DP, Ju J, Mbow C, Frost P & Loveland, T. 2010. Accessing Free Landsat Data Via the Internet: Africa's Challenge. *Remote Sensing Letters* 1, 2: 111-117.

Salim E & Ullsten O 1999. *Our forests, our future: Report of the world commission on forests and sustainable development*. Cambridge; New York: Cambridge University Press.

Sample A 1994. *Remote sensing and GIS in ecosystem management*. Washington: Island Press.

Santoro M, Shvidenko A, McCallum I, Askne J & Schmullius C 2007. Properties of ERS-1/2 Coherence in the Siberian Boreal Forest and Implications for Stem Volume Retrieval. *Remote Sensing of Environment* 106, 2: 154-172.

Schiewe J, Tufte L & Ehlers M 2001. Potential and Problems of Multi-Scale Segmentation Methods in Remote Sensing. GIS – *Zeitschrift für Geoinformationssysteme* 6: 34-39.

Schwab K 2016. The fourth industrial revolution. World Economic Forum

Sester M 2000. Knowledge Acquisition for the Automatic Interpretation of Spatial Data. *International Journal of Geographical information Science* 14, 1: 1-24.

Shuai Y, Masek JG, Gao F & Schaaf CB 2011. An Algorithm for the Retrieval of 30-M Snow-Free Albedo from Landsat Surface Reflectance and MODIS BRDF. *Remote Sensing of Environment* 115, 9: 2204-2216.

Sinha S, Jeganathan C, Sharma LK & Nathawat MS 2015. A Review of Radar Remote Sensing for Biomass Estimation. *International Journal of Environmental Science and Technology* 12, 5: 1779-1792.

Sokal, R., & Rohlf, F. (1995). *Biometry : The principles and practice of statistics in biological research* (3rd ed.). New York, N.Y.: Freeman.

Tan B 2006. The Impact of Gridding Artifacts on the Local Spatial Properties of MODIS Data: Implications for Validation, Compositing, and Band-to-Band Registration Across Resolutions. *Remote Sensing of Environment* 105, 2: 98-114.

Tang X 2013. Influence of Vegetation Phenology on Modelling Carbon Fluxes in Temperate Deciduous Forest by Exclusive use of MODIS Time-Series Data. *International Journal of Remote Sensing* 34, 23: 8373-8392.

Tansey KJ, Luckman AJ, Skinner L, Balzter H, Strozzi T & Wagner W 2004. Classification of Forest Volume Resources using ERS Tandem Coherence and JERS Backscatter Data. *International Journal of Remote Sensing* 25, 4: 751-768.

Thies B & Bendix J 2011. Satellite Based Remote Sensing of Weather and Climate: Recent Achievements and Future Perspectives. *Meteorological Applications* 18, 3: 262-295.

Thompson MW, Van Den Berg HM, Newby TS & Hoare D 2001. Guideline Procedures for National Land-Cover Mapping and Change Monitoring.

Thwaites R 2002. Spatial Terrain Analysis for Matching Native Tree Species to Sites: A Methodology. *New Forests New Forests: International Journal on the Biology, Biotechnology, and Management of Afforestation and Reforestation* 24, 2: 81-95.

Tucker CJ, Holben BN, Elgin Jr JH & McMurtrey III JE 1981. Remote Sensing of Total Dry-Matter Accumulation in Winter Wheat. *Remote Sensing of Environment* 11: 171-189.

Valentini R 2003. *Fluxes of carbon, water, and energy of European forests*. Berlin; New York: Springer.

Van Aardt JAN & Norris-Rogers M 2008. Spectral-Age Interactions in Managed, Even-Aged Eucalyptus Plantations: Application of Discriminant Analysis and Classification and Regression Trees Approaches to Hyperspectral Data. *International Journal of Remote Sensing* 29, 6: 1841-1845.

Van Leeuwen WJD, Huete AR & Laing TW 1999. MODIS Vegetation Index Compositing Approach: A Prototype with AVHRR Data. *Remote Sensing of Environment* , 69, 3: 264-280.

Van Zyl JJ & Kim Y 2011. Synthetic aperture radar polarimetry.

Van Zyl JJ 2001. The Shuttle Radar Topography Mission (SRTM): A Breakthrough in Remote Sensing of Topography. *Acta Astronautica* 48, 5-12: 559-565.

Vaughn NR, Asner GP & Giardina CP 2013. Polar Grid Fraction as an Estimator of Montane Tropical Forest Canopy Structure using Airborne Lidar. *International Journal of Remote Sensing* 34, 21: 7464-7473.

Verhulp J & Van Niekerk A 2016. Effect of inter-image spectral variation on land cover separability in heterogeneous areas. *International Journal of Remote Sensing* 37, 7: 1639-1657.

Vermote EF, Tanre D, Deuze JL, Herman M & Morcette J 1997. Second Simulation of the Satellite Signal in the Solar Spectrum, 6S: An Overview. *IEEE Transactions on Geoscience and Remote Sensing 35*, 3: 675-686.

Vicente-Serrano SM, Pérez-Cabello F & Lasanta T 2008. Assessment of Radiometric Correction Techniques in Analyzing Vegetation Variability and Change using Time Series of Landsat Images. *Remote Sensing of Environment* 112, 10: 3916-3934.

Vierling LA, Martinuzzi S, Asner GP, Jason S & Johnson BR 2011. LiDAR: Providing Structure. *Frontiers in Ecology and the Environment* 9, 5: 261-262.

Von Gadow K & Murray D 1989. Forest inventory systems for Mondi plantations. K D Forest Management Consulting Bosbestuur Konsultasies

Von Gadow K & Bredenkamp B 1992. *Forest management*. Pretoria: Academica.

Wu W, Hall CAS, Scatena FN & Quackenbush LJ 2006. Spatial Modelling of Evapotranspiration in the Luquillo Experimental Forest of Puerto Rico using Remotely Sensed Data. *Journal of Hydrology* 328, 3-4: 733-752.

Wulder MA 2008. Monitoring Canada's Forests. Part 1: Completion of the EOSD Land Cover Project. *Canadian Journal of Remote Sensing* 34, 6: 549-562.

Xiaoliang W, Danaher T, Wallace J & Campbell N 2001. A BRDF-Corrected Landsat-7 Mosaic of the Australian Continent. Paper deliverd at the Geoscience and Remote Sensing Symposium, 2001. IGARSS '01. IEEE 2001 International.

Zhang Y, Guindon B & Cihlar J 2002. An Image Transform to Characterize and Compensate for Spatial Variations in Thin Cloud Contamination of Landsat Images. *Remote Sensing of Environment* 82, 2-3: 173-187.

Zhu X, Helmer EH, Gao F, Liu D, Chen J & Lefsky MA 2016. A Flexible Spatiotemporal Method for Fusing Satellite Images with Different Resolutions. *Remote Sensing of Environment* 172: 165-177.

Zhu Z, Woodcock CE, Holden C & Yang Z 2015. Generating Synthetic Landsat Images Based on all Available Landsat Data: Predicting Landsat Surface Reflectance at any Given Time. *Remote Sensing of Environment* 162: 67-83.

Zhu Z, Woodcock CE & Olofsson P 2012. Continuous Monitoring of Forest Disturbance using all Available Landsat Imagery. *Remote Sensing of Environment* 122: 75-91.

APPENDICES

APPENDIX I: SCENE LIST OF IMAGERY USED FOR STUDY

USGS Scene ID	CSIR / SAC / SANSA EO Scene ID
LE71680772008042ASN00	L7-_ETM_HRF_BUMP_168-_00_077-_77_080211_073951_L3Aa_UTM36S
LE71680772008058ASN00	L7-_ETM_HRF_BUMP_168-_00_077-_77_080227_073946_L3Aa_UTM36S
LE71680772008106ASN00	L7-_ETM_HRF_BUMP_168-_00_077-_77_080415_073941_L3Aa_UTM36S
LE71680772008122ASN00	L7-_ETM_HRF_BUMP_168-_00_077-_77_080501_073938_L3Aa_UTM36S
LE71680772008218ASN00	L7-_ETM_HRF_BUMP_168-_00_077-_77_080805_073847_L3Aa_UTM36S
LE71680772008234ASN00	L7-_ETM_HRF_BUMP_168-_00_077-_77_080821_073841_L3Aa_UTM36S
LE71680772008250ASN00	L7-_ETM_HRF_BUMP_168-_00_077-_77_080906_073833_L3Aa_UTM36S
LE71680772008266ASN00	L7-_ETM_HRF_BUMP_168-_00_077-_77_080922_073824_L3Aa_UTM36S
LE71680772008298ASN00	L7-_ETM_HRF_BUMP_168-_00_077-_77_081024_073823_L3Aa_UTM36S
LE71680772008330ASN00	L7-_ETM_HRF_BUMP_168-_00_077-_77_081125_073850_L3Aa_UTM36S
LE71680772009076ASN00	L7-_ETM_HRF_BUMP_168-_00_077-_77_090317_073944_L3Aa_UTM36S
LE71680772009108ASN00	L7-_ETM_HRF_BUMP_168-_00_077-_77_090418_073955_L3Aa_UTM36S
LE71680772010015ASN00	L7-_ETM_HRF_BUMP_168-_00_077-_77_100115_074105_L3Aa_UTM36S
LE71680772010047ASN00	L7-_ETM_HRF_BUMP_168-_00_077-_77_100216_074129_L3Aa_UTM36S
LE71680772010127ASN00	L7-_ETM_HRF_BUMP_168-_00_077-_77_100507_074143_L3Aa_UTM36S
LE71680772010143ASN00	L7-_ETM_HRF_BUMP_168-_00_077-_77_100523_074140_L3Aa_UTM36S
LE71680772010159ASN00	L7-_ETM_HRF_BUMP_168-_00_077-_77_100608_074142_L3Aa_UTM36S
LE71680772010175ASN00	L7-_ETM_HRF_BUMP_168-_00_077-_77_100624_074144_L3Aa_UTM36S
LE71680772010191ASN00	L7-_ETM_HRF_BUMP_168-_00_077-_77_100710_074146_L3Aa_UTM36S
LE71680772010207ASN00	L7-_ETM_HRF_BUMP_168-_00_077-_77_100726_074147_L3Aa_UTM36S
LE71680782008058ASN00	L7-_ETM_HRF_BUMP_168-_00_078-_78_080227_074010_L3Aa_UTM36S
LE71680782008106ASN00	L7-_ETM_HRF_BUMP_168-_00_078-_78_080415_074005_L3Aa_UTM36S
LE71680782008122ASN00	L7-_ETM_HRF_BUMP_168-_00_078-_78_080501_074002_L3Aa_UTM36S
LE71680782008218ASN00	L7-_ETM_HRF_BUMP_168-_00_078-_78_080805_073911_L3Aa_UTM36S
LE71680782008234ASN00	L7-_ETM_HRF_BUMP_168-_00_078-_78_080821_073904_L3Aa_UTM36S
LE71680782008250ASN00	L7-_ETM_HRF_BUMP_168-_00_078-_78_080906_073857_L3Aa_UTM36S
LE71680782008266ASN00	L7-_ETM_HRF_BUMP_168-_00_078-_78_080922_073848_L3Aa_UTM36S
LE71680782008298ASN00	L7-_ETM_HRF_BUMP_168-_00_078-_78_081024_073847_L3Aa_UTM36S
LE71680782009076ASN00	L7-_ETM_HRF_BUMP_168-_00_078-_78_090317_074008_L3Aa_UTM36S
LE71680782009092ASN00	L7-_ETM_HRF_BUMP_168-_00_078-_78_090402_074014_L3Aa_UTM36S
LE71680782009108ASN00	L7-_ETM_HRF_BUMP_168-_00_078-_78_090418_074019_L3Aa_UTM36S
LE71680782009316ASN00	L7-_ETM_HRF_BUMP_168-_00_078-_78_091112_074032_L3Aa_UTM36S
LE71680782010015ASN00	L7-_ETM_HRF_BUMP_168-_00_078-_78_100115_074129_L3Aa_UTM36S
LE71680782010031ASN00	L7-_ETM_HRF_BUMP_168-_00_078-_78_100131_074142_L3Aa_UTM36S
LE71680782010047ASN00	L7-_ETM_HRF_BUMP_168-_00_078-_78_100216_074153_L3Aa_UTM36S
LE71680782010127ASN00	L7-_ETM_HRF_BUMP_168-_00_078-_78_100507_074207_L3Aa_UTM36S
LE71680782010143ASN00	L7-_ETM_HRF_BUMP_168-_00_078-_78_100523_074204_L3Aa_UTM36S
LE71680782010159ASN00	L7-_ETM_HRF_BUMP_168-_00_078-_78_100608_074206_L3Aa_UTM36S
LE71680782010175ASN00	L7-_ETM_HRF_BUMP_168-_00_078-_78_100624_074208_L3Aa_UTM36S
LE71680782010191ASN00	L7-_ETM_HRF_BUMP_168-_00_078-_78_100710_074210_L3Aa_UTM36S
LE71680782010207ASN00	L7-_ETM_HRF_BUMP_168-_00_078-_78_100726_074211_L3Aa_UTM36S

Appendix I: Scene list of imagery used for study

USGS Scene ID	CSIR / SAC / SANSA EO Scene ID
LE71680782010303ASN00	L7-_ETM_HRF_BUMP_168-_00_078-_78_101030_074228_L3Aa_UTM36S
LE71680782010335ASN00	L7-_ETM_HRF_BUMP_168-_00_078-_78_101201_074252_L3Aa_UTM36S
LE71680802008106ASN00	L7-_ETM_HRF_BUMP_168-_00_080-_80_080415_074053_L3Aa_UTM36S
LE71680802008154ASN00	L7-_ETM_HRF_BUMP_168-_00_080-_80_080602_074037_L3Aa_UTM36S
LE71680802008218ASN01	L7-_ETM_HRF_BUMP_168-_00_080-_80_080805_073959_L3Aa_UTM36S
LE71680802008234ASN00	L7-_ETM_HRF_BUMP_168-_00_080-_80_080821_073952_L3Aa_UTM36S
LE71680802008250ASN00	L7-_ETM_HRF_BUMP_168-_00_080-_80_080906_073945_L3Aa_UTM36S
LE71680802008266ASN00	L7-_ETM_HRF_BUMP_168-_00_080-_80_080922_073936_L3Aa_UTM36S
LE71680802008298ASN00	L7-_ETM_HRF_BUMP_168-_00_080-_80_081024_073935_L3Aa_UTM36S
LE71680802009044ASN00	L7-_ETM_HRF_BUMP_168-_00_080-_80_090213_074039_L3Aa_UTM36S
LE71680802009092ASN00	L7-_ETM_HRF_BUMP_168-_00_080-_80_090402_074102_L3Aa_UTM36S
LE71680802009124ASN00	L7-_ETM_HRF_BUMP_168-_00_080-_80_090504_074110_L3Aa_UTM36S
LE71680802009140ASN00	L7-_ETM_HRF_BUMP_168-_00_080-_80_090520_074112_L3Aa_UTM36S
LE71680802009156ASN00	L7-_ETM_HRF_BUMP_168-_00_080-_80_090605_074112_L3Aa_UTM36S
LE71680802009188ASN00	L7-_ETM_HRF_BUMP_168-_00_080-_80_090707_074107_L3Aa_UTM36S
LE71680802009316ASN00	L7-_ETM_HRF_BUMP_168-_00_080-_80_091112_074120_L3Aa_UTM36S
LE71680802010031ASN00	L7-_ETM_HRF_BUMP_168-_00_080-_80_100131_074230_L3Aa_UTM36S
LE71680802010047ASN00	L7-_ETM_HRF_BUMP_168-_00_080-_80_100216_074241_L3Aa_UTM36S
LE71680802010079ASN00	L7-_ETM_HRF_BUMP_168-_00_080-_80_100320_074255_L3Aa_UTM36S
LE71680802010127ASN00	L7-_ETM_HRF_BUMP_168-_00_080-_80_100507_074255_L3Aa_UTM36S
LE71680802010143ASN00	L7-_ETM_HRF_BUMP_168-_00_080-_80_100523_074252_L3Aa_UTM36S
LE71680802010159ASN00	L7-_ETM_HRF_BUMP_168-_00_080-_80_100608_074254_L3Aa_UTM36S
LE71680802010175ASN00	L7-_ETM_HRF_BUMP_168-_00_080-_80_100624_074256_L3Aa_UTM36S
LE71680802010191ASN00	L7-_ETM_HRF_BUMP_168-_00_080-_80_100710_074258_L3Aa_UTM36S
LE71680802010207ASN00	L7-_ETM_HRF_BUMP_168-_00_080-_80_100726_074259_L3Aa_UTM36S
LE71680802010239ASN00	L7-_ETM_HRF_BUMP_168-_00_080-_80_100827_074301_L3Aa_UTM36S
LE71680802010255ASN00	L7-_ETM_HRF_BUMP_168-_00_080-_80_100912_074303_L3Aa_UTM36S
LE71690772008049ASN00	L7-_ETM_HRF_BUMP_169-_00_077-_77_080218_074600_L3Aa_UTM36S
LE71690772008081ASN00	L7-_ETM_HRF_BUMP_169-_00_077-_77_080321_074553_L3Aa_UTM36S
LE71690772008113ASN00	L7-_ETM_HRF_BUMP_169-_00_077-_77_080422_074551_L3Aa_UTM36S
LE71690772008129ASN00	L7-_ETM_HRF_BUMP_169-_00_077-_77_080508_074546_L3Aa_UTM36S
LE71690772008209ASN00	L7-_ETM_HRF_BUMP_169-_00_077-_77_080727_074501_L3Aa_UTM36S
LE71690772008225ASN00	L7-_ETM_HRF_BUMP_169-_00_077-_77_080812_074455_L3Aa_UTM36S
LE71690772008241ASN00	L7-_ETM_HRF_BUMP_169-_00_077-_77_080828_074448_L3Aa_UTM36S
LE71690772008305ASN00	L7-_ETM_HRF_BUMP_169-_00_077-_77_081031_074441_L3Aa_UTM36S
LE71690772008353ASN00	L7-_ETM_HRF_BUMP_169-_00_077-_77_081218_074515_L3Aa_UTM36S
LE71690772009003ASN00	L7-_ETM_HRF_BUMP_169-_00_077-_77_090103_074522_L3Aa_UTM36S
LE71690772009083ASN00	L7-_ETM_HRF_BUMP_169-_00_077-_77_090324_074558_L3Aa_UTM36S
LE71690772009099ASN00	L7-_ETM_HRF_BUMP_169-_00_077-_77_090409_074603_L3Aa_UTM36S
LE71690772009115ASN00	L7-_ETM_HRF_BUMP_169-_00_077-_77_090425_074607_L3Aa_UTM36S
LE71690772009131ASN00	L7-_ETM_HRF_BUMP_169-_00_077-_77_090511_074610_L3Aa_UTM36S
LE71690772009147ASN00	L7-_ETM_HRF_BUMP_169-_00_077-_77_090527_074611_L3Aa_UTM36S
LE71690772009163ASN00	L7-_ETM_HRF_BUMP_169-_00_077-_77_090612_074610_L3Aa_UTM36S
LE71690772010022ASN00	L7-_ETM_HRF_BUMP_169-_00_077-_77_100122_074721_L3Aa_UTM36S
LE71690772010038ASN00	L7-_ETM_HRF_BUMP_169-_00_077-_77_100207_074734_L3Aa_UTM36S

Appendix I: Scene list of imagery used for study

USGS Scene ID	CSIR / SAC / SANSA EO Scene ID
LE71690772010070ASN00	L7-_ETM_HRF_BUMP_169-_00_077-_77_100311_074751_L3Aa_UTM36S
LE71690772010230ASN00	L7-_ETM_HRF_BUMP_169-_00_077-_77_100818_074758_L3Aa_UTM36S
LE71690772010246ASN00	L7-_ETM_HRF_BUMP_169-_00_077-_77_100903_074801_L3Aa_UTM36S
LE71690772010310ASN00	L7-_ETM_HRF_BUMP_169-_00_077-_77_101106_074820_L3Aa_UTM36S
LE71750832008011ASN00	L7-_ETM_HRF_BUMP_175-_00_083-_83_080111_082534_L3Aa_UTM34S
LE71750832008027ASN00	L7-_ETM_HRF_BUMP_175-_00_083-_83_080127_082533_L3Aa_UTM34S
LE71750832008043ASN00	L7-_ETM_HRF_BUMP_175-_00_083-_83_080212_082530_L3Aa_UTM34S
LE71750832008059ASN00	L7-_ETM_HRF_BUMP_175-_00_083-_83_080228_082526_L3Aa_UTM34S
LE71750832008075ASN00	L7-_ETM_HRF_BUMP_175-_00_083-_83_080315_082521_L3Aa_UTM34S
LE71750832008123ASN00	L7-_ETM_HRF_BUMP_175-_00_083-_83_080502_082517_L3Aa_UTM34S
LE71750832008219ASN00	L7-_ETM_HRF_BUMP_175-_00_083-_83_080806_082426_L3Aa_UTM34S
LE71750832008235ASN00	L7-_ETM_HRF_BUMP_175-_00_083-_83_080822_082419_L3Aa_UTM34S
LE71750832008299ASN00	L7-_ETM_HRF_BUMP_175-_00_083-_83_081025_082404_L3Aa_UTM34S
LE71750832008315ASN00	L7-_ETM_HRF_BUMP_175-_00_083-_83_081110_082418_L3Aa_UTM34S
LE71750832008331ASN00	L7-_ETM_HRF_BUMP_175-_00_083-_83_081126_082431_L3Aa_UTM34S
LE71750832008347ASN00	L7-_ETM_HRF_BUMP_175-_00_083-_83_081212_082441_L3Aa_UTM34S
LE71750832009077ASN00	L7-_ETM_HRF_BUMP_175-_00_083-_83_090318_082524_L3Aa_UTM34S
LE71750832009125ASN00	L7-_ETM_HRF_BUMP_175-_00_083-_83_090505_082538_L3Aa_UTM34S
LE71750832009205ASN00	L7-_ETM_HRF_BUMP_175-_00_083-_83_090724_082530_L3Aa_UTM34S
LE71750832009221ASN00	L7-_ETM_HRF_BUMP_175-_00_083-_83_090809_082524_L3Aa_UTM34S
LE71750832009237ASN00	L7-_ETM_HRF_BUMP_175-_00_083-_83_090825_082523_L3Aa_UTM34S
LE71750832009253ASN00	L7-_ETM_HRF_BUMP_175-_00_083-_83_090910_082523_L3Aa_UTM34S
LE71750832009317ASN00	L7-_ETM_HRF_BUMP_175-_00_083-_83_091113_082548_L3Aa_UTM34S
LE71750832010016ASN00	L7-_ETM_HRF_BUMP_175-_00_083-_83_100116_082645_L3Aa_UTM34S
LE71750832010032ASN00	L7-_ETM_HRF_BUMP_175-_00_083-_83_100201_082658_L3Aa_UTM34S
LE71750832010048ASN00	L7-_ETM_HRF_BUMP_175-_00_083-_83_100217_082709_L3Aa_UTM34S
LE71750832010064ASN00	L7-_ETM_HRF_BUMP_175-_00_083-_83_100305_082717_L3Aa_UTM34S
LE71750832010080ASN00	L7-_ETM_HRF_BUMP_175-_00_083-_83_100321_082723_L3Aa_UTM34S
LE71750832010096ASN00	L7-_ETM_HRF_BUMP_175-_00_083-_83_100406_082726_L3Aa_UTM34S
LE71750832010112ASN00	L7-_ETM_HRF_BUMP_175-_00_083-_83_100422_082725_L3Aa_UTM34S
LE71750832010144ASN00	L7-_ETM_HRF_BUMP_175-_00_083-_83_100524_082720_L3Aa_UTM34S
LE71750832010160ASN00	L7-_ETM_HRF_BUMP_175-_00_083-_83_100609_082721_L3Aa_UTM34S
LE71750832010176ASN00	L7-_ETM_HRF_BUMP_175-_00_083-_83_100625_082723_L3Aa_UTM34S
LE71750832010208ASN00	L7-_ETM_HRF_BUMP_175-_00_083-_83_100727_082726_L3Aa_UTM34S
LE71750832010224ASN00	L7-_ETM_HRF_BUMP_175-_00_083-_83_100812_082725_L3Aa_UTM34S
LE71750832010256ASN00	L7-_ETM_HRF_BUMP_175-_00_083-_83_100913_082730_L3Aa_UTM34S
LE71750832010288ASN00	L7-_ETM_HRF_BUMP_175-_00_083-_83_101015_082736_L3Aa_UTM34S
LE71750832010304ASN00	L7-_ETM_HRF_BUMP_175-_00_083-_83_101031_082744_L3Aa_UTM34S
LE71750832010336ASN00	L7-_ETM_HRF_BUMP_175-_00_083-_83_101202_082808_L3Aa_UTM34S
LE71750832010352ASN00	L7-_ETM_HRF_BUMP_175-_00_083-_83_101218_082815_L3Aa_UTM34S
LE71750842008011ASN00	L7-_ETM_HRF_BUMP_175-_00_084-_84_080111_082558_L3Aa_UTM34S
LE71750842008027ASN00	L7-_ETM_HRF_BUMP_175-_00_084-_84_080127_082557_L3Aa_UTM34S
LE71750842008059ASN00	L7-_ETM_HRF_BUMP_175-_00_084-_84_080228_082549_L3Aa_UTM34S
LE71750842008123ASN00	L7-_ETM_HRF_BUMP_175-_00_084-_84_080502_082541_L3Aa_UTM34S
LE71750842008203ASN00	L7-_ETM_HRF_BUMP_175-_00_084-_84_080721_082456_L3Aa_UTM34S

Appendix I: Scene list of imagery used for study

USGS Scene ID	CSIR / SAC / SANSA EO Scene ID
LE71750842008219ASN00	L7-_ETM_HRF_BUMP_175-_00_084-_84_080806_082450_L3Aa_UTM34S
LE71750842008235ASN00	L7-_ETM_HRF_BUMP_175-_00_084-_84_080822_082443_L3Aa_UTM34S
LE71750842008299ASN00	L7-_ETM_HRF_BUMP_175-_00_084-_84_081025_082428_L3Aa_UTM34S
LE71750842008315ASN00	L7-_ETM_HRF_BUMP_175-_00_084-_84_081110_082442_L3Aa_UTM34S
LE71750842008331ASN00	L7-_ETM_HRF_BUMP_175-_00_084-_84_081126_082455_L3Aa_UTM34S
LE71750842008347ASN00	L7-_ETM_HRF_BUMP_175-_00_084-_84_081212_082505_L3Aa_UTM34S
LE71750842008363ASN00	L7-_ETM_HRF_BUMP_175-_00_084-_84_081228_082513_L3Aa_UTM34S
LE71750842009013ASN00	L7-_ETM_HRF_BUMP_175-_00_084-_84_090113_082518_L3Aa_UTM34S
LE71750842009125ASN00	L7-_ETM_HRF_BUMP_175-_00_084-_84_090505_082602_L3Aa_UTM34S
LE71750842009205ASN00	L7-_ETM_HRF_BUMP_175-_00_084-_84_090724_082554_L3Aa_UTM34S
LE71750842009221ASN00	L7-_ETM_HRF_BUMP_175-_00_084-_84_090809_082548_L3Aa_UTM34S
LE71750842009237ASN00	L7-_ETM_HRF_BUMP_175-_00_084-_84_090825_082547_L3Aa_UTM34S
LE71750842009253ASN00	L7-_ETM_HRF_BUMP_175-_00_084-_84_090910_082547_L3Aa_UTM34S
LE71750842010016ASN00	L7-_ETM_HRF_BUMP_175-_00_084-_84_100116_082709_L3Aa_UTM34S
LE71750842010048ASN00	L7-_ETM_HRF_BUMP_175-_00_084-_84_100217_082733_L3Aa_UTM34S
LE71750842010064ASN00	L7-_ETM_HRF_BUMP_175-_00_084-_84_100305_082741_L3Aa_UTM34S
LE71750842010112ASN00	L7-_ETM_HRF_BUMP_175-_00_084-_84_100422_082749_L3Aa_UTM34S
LE71750842010160ASN00	L7-_ETM_HRF_BUMP_175-_00_084-_84_100609_082745_L3Aa_UTM34S
LE71750842010176ASN00	L7-_ETM_HRF_BUMP_175-_00_084-_84_100625_082747_L3Aa_UTM34S
LE71750842010224ASN00	L7-_ETM_HRF_BUMP_175-_00_084-_84_100812_082749_L3Aa_UTM34S
LE71750842010256ASN00	L7-_ETM_HRF_BUMP_175-_00_084-_84_100913_082754_L3Aa_UTM34S
LE71750842010304ASN00	L7-_ETM_HRF_BUMP_175-_00_084-_84_101031_082808_L3Aa_UTM34S
LE71750842010320ASN00	L7-_ETM_HRF_BUMP_175-_00_084-_84_101116_082821_L3Aa_UTM34S
LE71750842010336ASN00	L7-_ETM_HRF_BUMP_175-_00_084-_84_101202_082832_L3Aa_UTM34S
LE71750842010352ASN00	L7-_ETM_HRF_BUMP_175-_00_084-_84_101218_082839_L3Aa_UTM34S
LT51680772008258MLK00	L5-_TM-_HRF_BUMP_168-_00_077-_77_080914_073439_L3Aa_UTM36S
LT51680772010023JSA00	L5-_TM-_HRF_BUMP_168-_00_077-_77_100123_074023_L3Aa_UTM36S
LT51680772010119JSA00	L5-_TM-_HRF_BUMP_168-_00_077-_77_100429_074022_L3Aa_UTM36S
LT51680782009084JSA00	L5-_TM-_HRF_BUMP_168-_00_078-_78_090325_073644_L3Aa_UTM36S
LT51680782010119JSA00	L5-_TM-_HRF_BUMP_168-_00_078-_78_100429_074046_L3Aa_UTM36S
LT51680802009084JSA00	L5-_TM-_HRF_BUMP_168-_00_080-_80_090325_073731_L3Aa_UTM36S
LT51680802009116JSA00	L5-_TM-_HRF_BUMP_168-_00_080-_80_090426_073809_L3Aa_UTM36S
LT51680802009148JSA00	L5-_TM-_HRF_BUMP_168-_00_080-_80_090528_073844_L3Aa_UTM36S
LT51680802010119JSA00	L5-_TM-_HRF_BUMP_168-_00_080-_80_100429_074134_L3Aa_UTM36S
LT51690772009107JSA00	L5-_TM-_HRF_BUMP_169-_00_077-_77_090417_074258_L3Aa_UTM36S
LT51690772009139JSA00	L5-_TM-_HRF_BUMP_169-_00_077-_77_090519_074334_L3Aa_UTM36S
LT51690772009315JSA00	L5-_TM-_HRF_BUMP_169-_00_077-_77_091111_074604_L3Aa_UTM36S
LT51690772009331JSA00	L5-_TM-_HRF_BUMP_169-_00_077-_77_091127_074611_L3Aa_UTM36S
LT51690772009347JSA00	L5-_TM-_HRF_BUMP_169-_00_077-_77_091213_074620_L3Aa_UTM36S
LT51690772010126JSA00	L5-_TM-_HRF_BUMP_169-_00_077-_77_100506_074633_L3Aa_UTM36S

USGS ID Key:

LXSPPPRRRYYYYDDDGSIVV

LT51690772010126JSA00

Appendix I: Scene list of imagery used for study

Parameter	Description	Value (Examples only)
L	Satellite mission	L = Landsat
X	Sensor	E = Enhanced thematic mapper plus T = Thematic mapper
S	Satellite	5 = Landsat 5
PPP	WRS Path	169
RRR	WRS Row	077
YYYY	Year	2010
DDD	Julian day of the year	126
GSI	Ground station identifyer	JSA = Johannesburg South Afrika MLK = Malindi Kenya
VV	Version	01

SANSA ID Key:

SSS_sss_ttt_mmmm_pppp_ps_rrrr_rs_yymmdd_hhmmss_LLLL_PPPPPP

L7-_ETM_HRF_BUMP_0168_00_0077_00_010530_082459_L3Ab_UTM36S

Parameter	Description	Value (Examples only)
SSS	Satellite mission	L7- = Landsat-7
sss	Sensor	ETM = Enhanced thematic mapper plus TM = Thematic mapper
ttt	Image type	HRF = Multispectral HPN = L7 Panchromatic
mmmm	Imaging mode	BUMP = Bumper mode (Landsat)
pppp	Path index value	168- = WRS Path 168 (Landsat)
ps	Path shift	-3 = 15 % shift west
rrrr	Row index value	077- = WRS Path 077 (Landsat)
rs	Row shift Multiple frame image	+5 = 25% shift South 81 = multiple frame from row 077 - 081
yymmdd	Acquisition date	100801 = 01-Aug-2010
hhmmss	Acquisition centre time	062712 = 06AM 27minutes 12 seconds GMT
LLLL	Processing level	L3Aa = ortho DN (USGS L1T) L3Ab = ortho TOA Reflectance
PPPPPP	Projection	UTM35S ORBIT- = in sensor geometry/not projected

APPENDIX II: CODE DEFINING SPECTRAL CLASSES

```
! Strong Vegetation Spectral Rule
IF (SpectralClass = "V_SR") and (NDVI >= 0.630) and (MIR1 < 0.120) and (MIR2 < 0.050) and (NDBSI < -0.320) Then
    SpectralClass = "SV_SC"
ENDIF
! Strong Vegetation with High NIR Spectral Rule
IF (SpectralClass = "SV_SC") and (NIR >= 0.230) Then
    SpectralClass = "SVHNIR_LSC"
! Strong Vegetation with Low NIR Spectral Rule
ELSEIF (SpectralClass = "SV_SC") and (NIR < 0.230) Then
    SpectralClass = "SVLNIR_LSC"
ENDIF

! Average Vegetation Spectral Rule
IF (SpectralClass = "V_SR") and (NDVI < 0.630) and (NDVI >= 0.560) and (MIR1 < 0.120) and (MIR2 < 0.050) and (NDBSI < -0.320) Then
    SpectralClass = "AV_SC"
ENDIF
! Average Vegetation with High NIR Spectral Rule
IF (SpectralClass = "AV_SC") and (NIR >= 0.230) Then
    SpectralClass = "AVHNIR_LSC"
! Average Vegetation with Low NIR Spectral Rule
ELSEIF (SpectralClass = "AV_SC") and (NIR < 0.230) Then
    SpectralClass = "AVLNIR_LSC"
ENDIF

! Weak Vegetation Spectral Rule
IF (SpectralClass = "V_SR") and (NDVI < 0.560) and (MIR1 < 0.120) and (MIR2 < 0.050) and (NDBSI < -0.320) Then
    SpectralClass = "WV_SC"
ENDIF
! Weak Vegetation with High NIR Spectral Rule
IF (SpectralClass = "WV_SC") and (NIR >= 0.230) Then
    SpectralClass = "WVHNIR_LSC"
! Weak Vegetation with High NIR Spectral Rule
ELSEIF (SpectralClass = "WV_SC") and (NIR < 0.230) Then
    SpectralClass = "WVLNIR_LSC"
ENDIF

! Weak Vegetation with high NDBSI Spectral Rule
IF (SpectralClass = "V_SR") and (NDVI < 0.560) and (MIR1 < 0.120) and (MIR2 < 0.050) and (NDBSI >= -0.320) Then
    SpectralClass = "DR_LSC"
ENDIF
```

APPENDIX III: IRREGULAR LATTICE AS IMAGE FORMAT

Optical sensors on board a satellite consists of an array of detectors measuring radiation intensities around a predefined area on the surface of the earth, within a spectral band at a given spectral response function (Figure III.4-1). Due to the point spread function, which determines the outward spatial distribution of radiation contribution from the centre of the observed area, the binning of measurements to picture elements is a misrepresentation and generalisation of a given sensor measurement. The spatial resampling of these measurements from the sensor geometry to a unified ground geometry in a particular map projection leads to a further degradation and generalisation of the data. Such transformations into common coordinate systems are required to perform matrix algebra or spatial analyses of different datasets. Multi-temporal image analysis, or image compositing as described in Chapter 2, is subjected to these shortcomings. The problem is exacerbated when dealing with imagery acquired at different spatial resolutions. Raster-based data cubes (Figure III.4-2), a concept where pixels of different resolutions are nested within one another, is a common approach for handling multi-resolution datasets. Data cubes, however, are challenged by the multitude of different ground sampling distances available. Geoscience Australia has been pioneering the development of this multi-temporal, multi-spatial data cube.

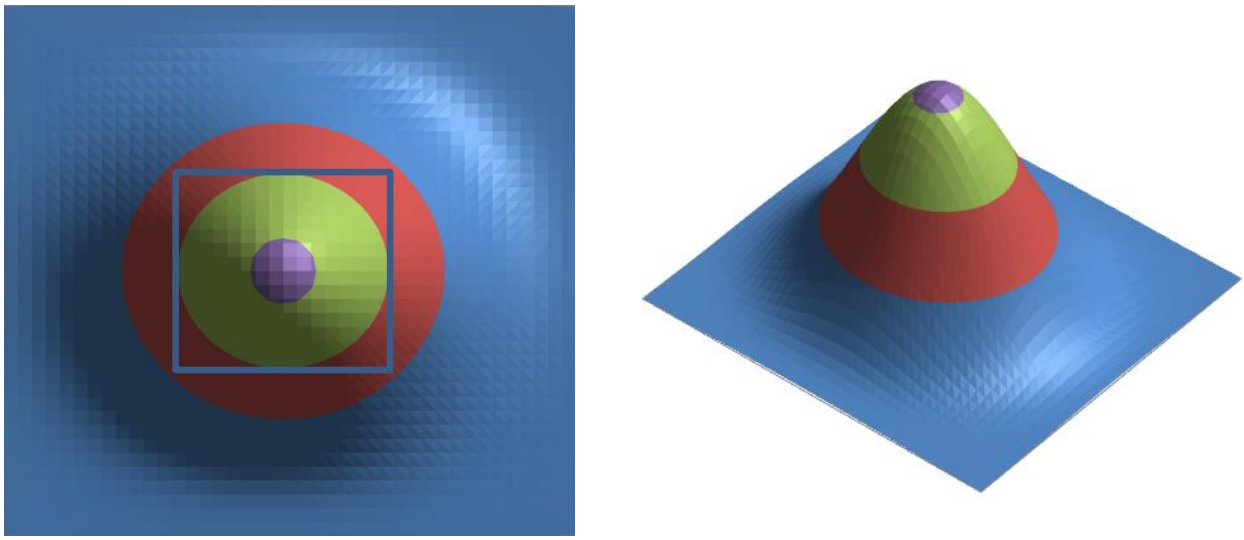

Figure III.4-1 Point spread function in 2D on the left, delineating the defined ground sampling distance of a pixel as a blue box. Values represent the contribution of radiation to sensor detector measurement in relation to the centre of the observation/pixel. On the right the same graph is rendered in 3D.

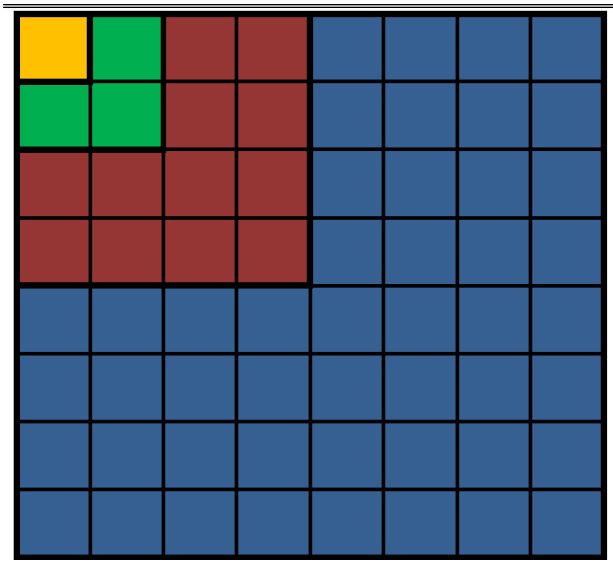

Figure III.4-2 Nesting of multi-resolution data into a multi-temporal data cube from imagery of different resolutions e.g. blue 8 m, brown 4 m, green 2 m, and yellow 1 m

Research is needed to circumvent or reduce the negative effects of resampling, especially within the context of MTMRMS imagery. One approach could be to represent such data as an irregular lattice, whereby single sensor observations are represented as points, geographically positioned at the centre of a single detector's field of view. Each observation can be described by the radiation intensity per band, with metadata provided for the sensor's point spread function, resolution, spectral response function, and radiometric accuracy. For multi-temporal image analysis, a weighting of observations can be applied for a certain area based on the proximity and properties of these point measurement representations.

Another topic of research could be the investigation of the most optimal data structure for a remote sensing-based data cube as irregular lattice. The option of adding two additional 32bit raster layers representing new X and Y geographic coordinates of each pixel in a remote sensing image should be further investigated. Alternatively, geometry can be calculated on the fly for only the area and data of interest using parameters provided in the metadata of the given imagery. The use of irregular lattice data formats commonly used for LIDAR or structure from motion (SFM) derived point clouds from UAV data should also be investigated for the fusion and analysis of multi-resolution and multidimensional data. The latest developments in geospatial databases may provide the tools for such an implementation. This implementation will pave the way for further avenues of research as discussed in Appendixes IV, V & IV.

APPENDIX IV: SPECTRAL, TEXTURAL PRE-CLASSIFICATION

Spectral and textural pre-classification of satellite imagery has become viable and is an attractive pre-processing step in which images are segmented based on spectral and textural parameters, and classes extracted that require special consideration in further pre-processing steps. (Baraldi et al. 2006) introduced the concept of spectral pre-classification of Landsat imagery, whereas Esch et al. (2010) demonstrated the use of textural filters and associated classifications for SAR imagery. Since then, many image pre-processing steps incorporated the use of classes derived from such techniques. Earlier versions of these spectral and textural classification techniques used reflectance values from spectral bands directly (such as implemented with SPECL in Atcor) (Richter & Schläpfer 2014), whereas other implementations rely on spectral indices and features derived from spectral bands. The latter tend to enhance the information content of the data and lead to a higher degree of classification accuracy, especially for targeted thematic classes. Further research needs to be done to identify the most applicable indices, textural features, and thematic features for rule-based classifications. These features should be calculated from a multitude of sensors and normalised so that an inter-sensor comparison of features becomes possible. Features should be grouped into those that are insensitive to atmospheric effects and topographic effects, and those that are intolerant to both atmospheric and topographic variations, but which hold the highest information content.

From the above it becomes clear that different rule-based classifications should be developed for different stages in the image pre-processing chain. The following workflow in Figure IV.1 illustrates this:

Appendix IV: Spectral, Textural Pre-Classification

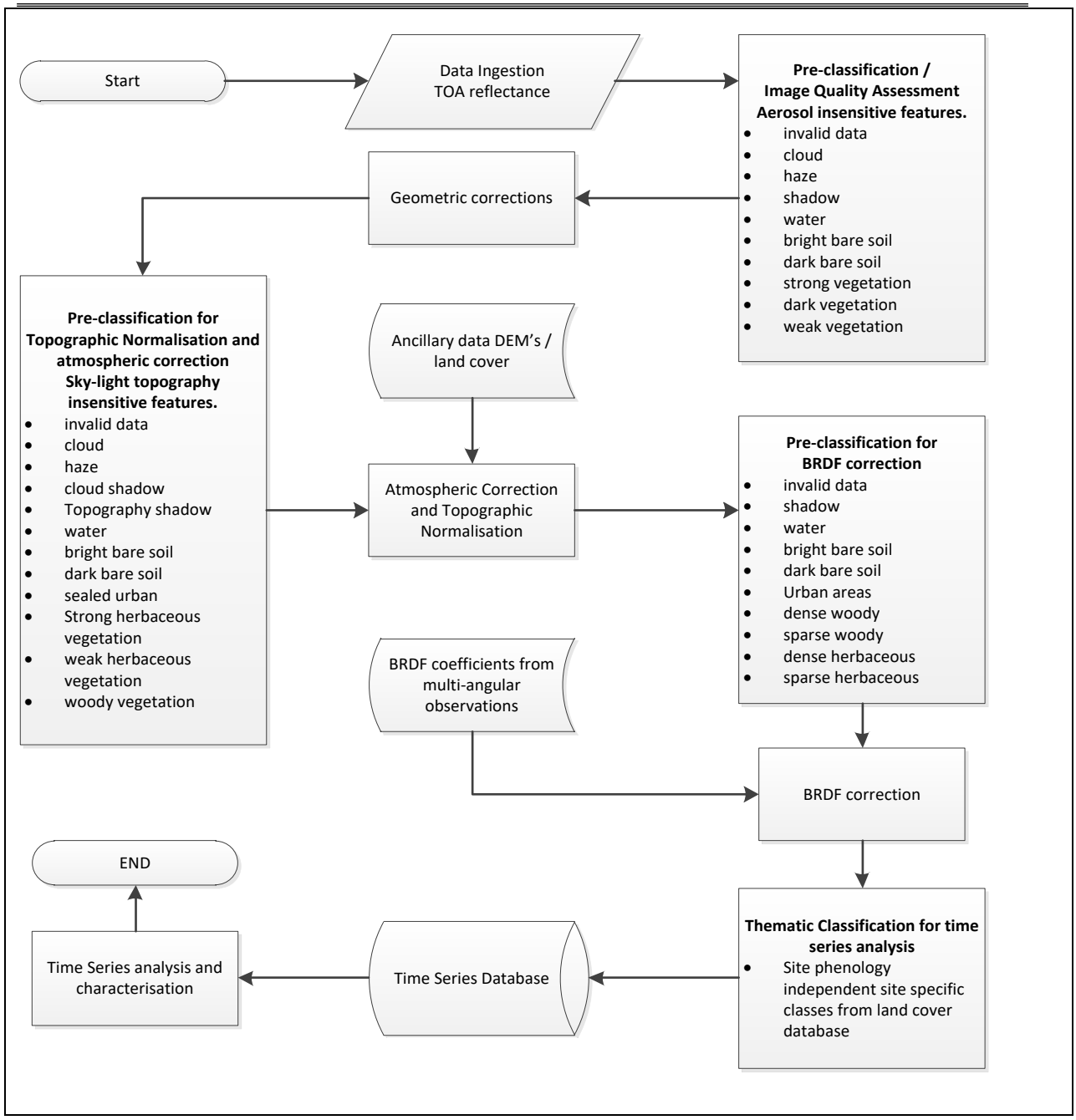

Figure IV.1 Illustration of different spectral textural rule-based classifications required for different pre-processing steps

Spectral and textural rule-based classifications should be implemented as fuzzy classifiers providing probability values for the best three class candidates and information on class stability and classification reliability. This information can then be used to segment images and generalise classifications, improving further thematic accuracy.

APPENDIX V: IMAGE PRE-PROCESSING

More research is required to improve a range of image pre-processing techniques essential for the automatic and accurate radiometric and geometric corrections of satellite imagery. Accurate geometric corrections of satellite imagery are essential for change detection and multi-temporal image analysis. A wide range of automated image registration approaches have been developed (Le Moigne, Netanyahu & Eastman 2011). These approaches can be divided into techniques using moving window cross-correlation techniques of matrixes either in the image or signal domain, and sometimes both. Semiglobal matching on the other hand is a pixel-to-pixel matching process useful for the matching of multi-angular imagery at a finer level of detail than what can be achieved by matrix-based cross-correlation (Hirschmüller 2008). Further research needs to be undertaken to develop image matching techniques that are guided by existing disparity reference data such as digital elevation models from the SRTM or Tandem-X mission. A pyramid approach needs to be investigated that uses spectral pre-classification to guide its matching approach and effort. No matching should be conducted over water, clouds, shadows or very homogenous areas. For the purpose of ground control point collection, a spectral and textural pre-classification can identify surfaces that are on the ground. GCPs should be collected from these surfaces only. This is particularly relevant for high spatial resolution imagery. Matching algorithms that work between SAR and optical imagery should receive considerable attention considering that the most accurate and current global reference dataset has been acquired by the TanDEM-X mission.

With the development of better image cross-correlation techniques and disparity measurements, including the use of SFM and image segmentation, the accurate extraction of 3D features can be achieved, which is presently very labour intensive. Research needs to focus on the integration of spectral and textural pre-classification, image matching, object-based image analysis, and 3D feature reconstruction.

Optical sensors on-board satellites acquiring imagery can be categorised in radiometrically well-calibrated (expensive systems such as Landsat and MODIS) and poorly calibrated (inexpensive systems such as those from Planet Labs). As imagery from the second category of sensors is more frequently available and presents the majority of acquisitions at higher spatial resolution, considerable research needs to be undertaken to apply a cross-sensor calibration based on a spectral pre-classification and regression analysis between well-calibrated and poorly calibrated observations. Considering that well-calibrated observations from, for example MODIS, can automatically be atmospherically and BRDF corrected due to the high spectral information

content, a radiometric cross-calibration of poorly calibrated imagery against these well-calibrated atmospherically corrected imagery may, in itself, already provide a quick and dirty atmospheric correction and radiometric normalisation of the initially poorly-characterised spectral data.

The most popular atmospheric correction tools implemented in commercial image processing software are Atcor (Richter 2011b) and 6S (Vermote et al. 1997). These tools rely on the use of standard atmosphere models represented by look-up tables with the 6S tool providing a higher level of flexibility than Atcor. Nonetheless, atmospheric corrections with these tools remain somewhat of a “black art” as actual atmospheric conditions during the acquisition of imagery are seldom taken into consideration. The integration of meteorological information captured by geostationary meteorological satellites and sensors such as MODIS have successfully been demonstrated for the correction of Landsat ETM+ imagery using 6S (Ju et al. 2012), but this becomes less practical with imagery from satellites with a larger delta of equatorial crossing times than those provided by the polar orbiting meteorological satellites. Substantial progress has been made with Numerical Weather Prediction models that uses meteorological satellite imagery to interpolate or extrapolate (predict) atmospheric conditions for any given period of time (Thies & Bendix 2011). Research is required to integrate output from these systems with atmospheric correction tools to provide a better approximation of atmospheric parameters for accurate atmospheric corrections.

Top of atmosphere (TOA) reflectance measurements are affected by the solar incidence angle, which is a combination of the solar elevation and azimuth angle and the orientation of the slopes of topography on the earth’s surface. Slopes facing the sun are subsequently exposed to more light than slopes facing away from the sun and therefore reflectance records differ significantly between these extremes. Vicente-Serrano, Pérez-Cabello & Lasanta (2008) investigated a range of image pre-processing techniques required for an improved classification. They argued a strong case for topographic normalisation, favouring techniques that take the different BRDF characteristics of surfaces into account.

A wide range of methods has been developed for the radiometric normalisation of optical satellite imagery. Many of these methods are based on empirical approaches that investigate statistical patterns in data that can be attributed to radiometric distortions and then correct the patterns realistically. Physical models should be preferred over empirical models as they characterise the spectral deviation based purely on physics. The big drawback of physical models is the lack of actual environmental measurements required to fully model radiation transfer. To alleviate this problem in a practical manner, physical models are often combined with empirical

models to provide an operational solution. An example of this is the correction techniques implemented in Atcor 2 & 3 (Richter 2011a). This can be clearly illustrated by the topographic correction techniques implemented in Atcor 3, which provide empirical threshold-based models that are surface-type independent. They therefore do not account for bidirectional distribution function (BRDF) characteristics of different surfaces in an image, but rather apply a generalised correction. A preferred physical topographic radiometric correction would be the Minaert correction, but it requires a pre-classification of the image into surface types, which are mostly not available, as has been demonstrated by Baraldi, Gironda & Simonetti (2010). The identification of shade and the correction thereof also use an empirical approach whereby a histogram pattern on the low end of the histogram distribution is identified that matches that of the general image. With the presence of water or a biased shade distribution, this technique can go horribly wrong. The same applies for LEDAPS and the underlying 6S code. LEDAPS is the radiometric image pre-processing software used for Landsat in the United States by the majority of researchers. LEDAPS makes use of the empirical assumption that dark dense vegetation can be found in an image and optical depth extracted by accessing the difference between reconstructed blue or green bands from short wave infrared (SWIR) bands (Masek et al. 2006). As dark dense vegetation does not exist in all scenes, this empirical optical depth retrieval method is not suitable for arid regions.

Various surface types reflect light into different directions at different intensities. These are wavelength dependent and described as a BRDF. The BRDF correction of high spatial resolution imagery, often acquired only from one angle, needs further research. The foundation for this correction has already been laid but further improvement is needed in order to apply this technique to a large range of high resolution optical imagery (Shuai et al. 2011). A BRDF specific spectral rule-based classification, together with a spatial segmentation of the high spatial resolution image, is going to aid the transferability of BRDF coefficients derived from multi-angular but low spatial resolution satellite images.

The radiometric correction of optical satellite imagery through topographic normalisation is generally a complicated undertaking as it requires a good pre-classification of imagery to account for BRDF effects and the elimination of sky light components through atmospheric corrections. The pre-classification has to be undertaken from calculated features and indices that are not sensitive to topographic variations. These techniques have yet to be developed. Furthermore, the quality of the DEM that will be used for the corrections needs to be very high to avoid artefacts. The Minnaert correction, often considered the best technique, requires the

Minnaert coefficient K to be calculated via regression analysis after a logarithmic transformation. This logarithmic regression analysis is very sensitive to the quality of samples used for this analysis (Richter, Kellenberger & Kaufmann 2009). A new topographic normalisation technique needs to be developed that tolerates poor quality DEMs and that will offset the sky light and BRDF effects more clearly.

APPENDIX VI: IMAGE ANALYSIS/CLASSIFICATION

Appendix IV illustrated that it is apparent that image classification needs to take place several times for different image pre-processing steps. This is also true during the final stages of image analysis and extraction of geospatial information (Baraldi & Boschetti 2012a). GEOBIA lends itself to the development of iterative automated classification workflows. Although it has gained popularity since 2000 (Benz et al. 2004), a real breakthrough to fully-automated classification chains in the earth observation sector has not been made (Blaschke 2010). This can be contributed to the fact that it is used with non-normalised data (Baraldi & Boschetti 2012b). Future research is necessary in the development of classification workflows from normalised data using spectral/textural pre-classification and multi-spatial, multi-temporal, and multi-source data as input, using both SAR and optical imagery together with multidimensional point clouds. Machine learning techniques and advanced data mining are highly automated and can greatly aid classical image interpretation and classification techniques, thereby developing rule bases using GEOBIA.

Vegetation is characterised by pronounced spectral reflectance variations that characterise responses to the availability of resources such as light, water, temperature, and minerals. In addition, fluctuations can be attributed to the various growth stages from germination to growth, flowering, maturation, and senescent. In perennial vegetation, which dominates forests, this is modulated with annual fluctuations due to the climatic seasons. This spectral variability is synonymous with phonological variability and the phenomenon is therefore termed phenology. In order to extract sufficient thematic information of vegetation from optical remotely sensed images, phenology (which can only be characterised through multi-temporal datasets across all seasons) needs to be taken into account. Mathematical functions have been derived for each pixel from a multi-temporal image stack from the same sensor with the same resolution (Zhu, Woodcock & Olofsson 2012), with further advances being made with more complex functions (Zhu et al. 2015). This work has led to the development of new fusion algorithms using spectral information from hyper-temporal MODIS observations and spatial information from the less frequent but higher spatial resolution Landsat imagery (Zhu et al. 2016:165). Much research, however, is still required to apply this approach to a mixture of numerous temporal, spectral, and spatial resolution datasets. Considering the computational burden and overheads of computing a mathematical function for the spectral phonologic behaviour of each pixel, perhaps research should rather concentrate on calculating these for image objects.

Considering that remote sensing analysts seldom have the skill to conduct all the image pre-processing steps and handle large data cubes (as previously mentioned in sections of Appendices (II, IV, & V)), the form of data presentation to remote sensing needs further research by analysts. An interesting approach would be to provide analysts with the mathematical functions per pixel describing phenology only. This would allow analysts to simulate an image at a given resolution for any given moment in time. This concept can be taken further for ecologists or other applied disciplines, whereas phenological patterns of biophysical variables are presented with these functions rather than spectral fluctuations. This would stimulate a wider and more appropriate use of remotely sensed imagery by the disciplines that could benefit most from this. When taking this concept into an operational environment, GIS users such as foresters could be presented with abstracted information from these biophysical parameters that are also described by mathematical functions. This information could be things like biomass, standing timber, mean annual increment, etc. Together with thematic information such as species composition, this information can be coupled with existing growth and yield models and spatial optimisation models using linear programming techniques, which again feeds into on-board computers of harvesting, extraction, transportation, and timber processing plants. Research in this field will finally close the information loop between remote sensing image acquisition and the seamless operational use of this information.